Synthetic Methods for Nanomaterials of Controlled Composition and Morphology

by

Bryan Matthew Tienes

B.S., University of Missouri – St. Louis, 2003

A thesis submitted to the

Faculty of the Graduate School of the

University of Colorado in partial fulfillment

of the requirement for the degree of

Doctor of Philosophy

Department of Chemistry and Biochemistry

2013

This thesis entitled:

Synthetic Methods for Nanomaterials of Controlled Composition and Morphology

written by Bryan Matthew Tienes

has been approved for the Department of Chemistry and Biochemistry

_____

Chair: Daniel L. Feldheim

_____

Gordana Dukovic

Date _____

The final copy of this thesis has been examined by the signatories, and we find that both the content and the form meet acceptable presentation standards of scholarly work in the above mentioned discipline.

Tienes, Bryan M. (Ph.D., Department of Chemistry and Biochemistry)

Synthetic Methods for Nanomaterials of Controlled Composition and Morphology

Thesis directed by Professor Daniel L. Feldheim

Novel heterogeneous catalysts are required to meet the energy needs of future generations and reduce emissions of carbon dioxide. Many of the recent advances in catalysis have been in the study of nanoparticles. The catalytic activity of nanoparticles relies heavily on their composition, crystal morphology, and surface structure. The best approach for the discovery of new catalysts is to first identify the most catalytically active elemental compositions and then synthesize nanoparticles of those compositions in the most active morphology. This dissertation covers three projects, each with the goal of addressing deficiencies the methods currently available for that catalyst discovery approach.

The work presented in Chapter 2 addressed deficiencies in the current synthetic methods used to discover materials with the most active composition. Presented is a method for synthesizing combinatorial catalysts arrays from precursor nanoparticles. Many researchers have turned to combinatorial methods to identify heterogeneous catalysts due to the difficultly in predicting active catalytic compositions *a priori*. First the synthetic method was demonstrated for generating arrays of gold and silver alloy nanoparticles, and then platinum and ruthenium nanoparticles were used to demonstrate the ability of the synthetic method to generate arrays for a combinatorial study.

The final two chapters focused on understanding the role of capping ligands in nanoparticle synthesis and then utilizing their functionality to direct the synthesis of nanoparticles to produce a desired surface structure. Chapter 3 discusses the role of the

popular capping ligands, alkyl phosphonic acids, in the synthesis of anisotropic zinc oxide nanoparticles. Chapter 4 describes work with the goal of using *in vitro* selection procedures to select RNA capable of directing the growth of platinum nanoparticles so that the desired surface structure is exposed on the surface of the nanoparticle product.

For the strongest woman I know, my mother, I love you.

Acknowledgements

I am extremely appreciative of all of the friends and family that have loved and supported me while in Boulder. My parents have always been my biggest fans and supporters and I could not be where I am today without them. My Dad taught me everything I know about tools and improvising while building things, which came in handy in the lab on several occasions. I could not thank my Mom enough for all of the love and support, and that is all I can say about that. My Brother and Sister are friends and confidants, thank you. The rest of my family, grandparents, aunts, uncles, cousins, Dieter, are all an important part of my life and I want to thank them as well.

I would like to thank my advisor, Dan Feldheim. He stuck with me through successes and failures, and I really appreciate it. I would like to thank Gordana for giving me the chance to do additional renewable energy research and everyone in her lab for accepting me as one of their own.

I would also like to thank all of the friends I have made over the years. Friends from St. Louis, Georger, Julie, Christy, Matt, Craig, Ed, and all the others, thank you. The friends I've made in Boulder, Carly, Keith, Molly, Kyle, Jen, Jamee, Candice, Chris A., thank you.

My wife, Jessica, I love you and thank you for coming into my life. You have made the last two and a half years of grad school the best years of my life. I cannot imagine my life without you.

Once again, thank you Mom and Dad, I could not have done it without you.

Contents

List of Tables

List of Figures

Chapter 1. Introduction

1.1 Motivation

Reducing the anthropogenic emissions of carbon dioxide, and important greenhouse gas, requires the development of new, carbon-free, and renewable energy sources. The largest source of renewable energy is the sun, which strikes the earth with as much energy in one hour as is currently used in a full year by all of humanity.[1] Unfortunately, current technological limitations prevent the utilization of that vast wealth of energy. New technologies capable of converting solar radiation into useable forms of energy have to be developed. A Department of Energy (DOE) report identified catalysis as "the key to energy conversion" and concluded that it was not only important to discover new catalysts, but it was also important to develop new systematic methods capable of identifying novel materials with enhanced catalytic activity.[2] One catalyst class of interest converts solar energy directly into useable forms of energy in the chemical bonds of fuels (i.e. photocatalysts).[1] Additionally, the utilization of those fuels requires an efficient way to convert the stored chemical energy into electricity. Fuel cells do this well, but require catalysts on their electrodes due to the slow oxidation kinetics of most fuels.[3] Therefore, the discovery of new catalysts is essential to the development of renewable energy sources that are less polluting than fossil fuels and are capable of satisfying the growing energy demand.[4] Deficiencies in the catalysts currently used for renewable energy applications require the identification of more efficient, cost effective, and environmentally friendly catalyst materials. In order to address these problems, there have been many notable advancements in the field of heterogeneous catalysis involving nano-structured materials.[5] Nano-structured materials are finely divided versions of bulk materials with dimensions on the order of

hundreds down to tens (or even fewer) of nanometers. They have found their niche as superior catalysts to traditional bulk materials, and another DOE report concluded that many of the catalysts required to support the energy of the future will be nano-materials.[6] The goal of the work presented as part of this dissertation was to improve upon the current methods used to identify and synthesize novel catalytic nano-materials.

Interest in one class of nano-materials, colloidal nanoparticles, began with the observation of their fascinating optical properties. For noble metal nanoparticles, the conduction band electrons on the surface of the nanoparticle can collectively oscillate in resonance with the electric field of light producing a strong plasmon resonance absorbance. This absorbance is what gives nanoparticle solutions of gold and silver their vivid red and yellow colors and was famously first reported by Faraday in 1857.[7-9] Colloidal semiconductor nanoparticles have different, but equally fascinating, interaction with light. Semiconductor nanoparticles exhibit quantum confinement, which allows tuning of the nanoparticle's band gap by changing its size. Therefore, the photoluminescence wavelength is dependent on the nanoparticle's size.[10] Since these optical properties were discovered, the field of nanoparticle research has quickly matured and new nanoparticles have been developed with applications in catalysis relevant to energy conversion. Enhanced catalytic activity has been reported in nano-structured materials over their bulk counterparts, which can be largely, but not exclusively, attributed to the increased geometric surface area available for heterogeneous reactions.[5] In addition to the simple increase in surface area, nanoparticles exist in kinetically trapped non-equilibrium states and thus contain high energy surface atoms that readily participate in reactions.[5] As a consequence, the catalytic activity of some metals has been shown to increase

when shrunk to the nano-scale, and nanoparticles of a metal commonly considered to be inert, such as gold, can become catalytically active.[11] The sum of these advantages of nano-scale materials as energy converting catalysts have lead the field, including the work presented here, to the study of synthetic methods to develop novel nano-catalysts.

The synthesis of colloidal nanoparticles typically follows a similar reaction scheme to the one presented in Figure 1.1. The scheme begins with the reaction of precursors to form monomers in the presence of capping ligands. The precursors can consist of metal salts, metal complexes, reducing agents, oxygen sources, or chalcogenide sources. Monomers are usually defined as the simplest unit of the crystal structure (such as metal atoms, metal oxides, or metal chalcogenides) and are generated through reactions of the precursor molecules (for example, the reduction of a metal salt by a reducing agent to form a M^0 metal atom). When a critical monomer concentration is reached, they begin to aggregate to form nuclei. Those nuclei are, in turn, grown by the addition of more monomers until the nanoparticle has reached a steady state size.[8, 12] Under the proper conditions, the nanoparticles can form into shapes,

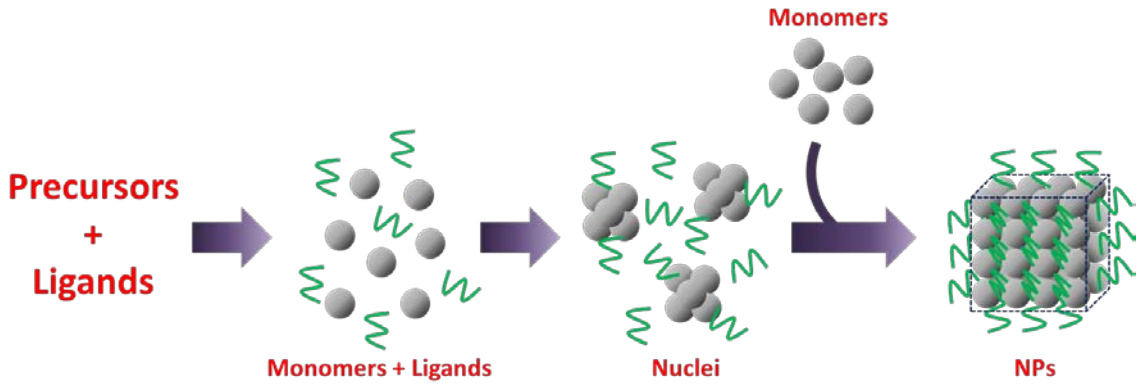

Figure 1.1. A General reaction scheme for the synthesis of colloidal nanoparticles. Precursors and ligands are combined in a solvent. Following a reaction of the precursors, metal or semiconductor monomers are formed. When a critical monomer concentration is reached they begin to aggregate, forming nuclei. The nuclei are then grown with the addition of additional monomers until a steady state nanoparticle of a specific morphology is formed.

such as the cube depicted in Figure 1.1. The shapes of nanoparticles are determined by the identity of the crystal facets displayed on their surfaces.[13] Modification of that typical procedure by swapping out the precursors or capping ligands along with controlling the rate of monomer production has led to a vast array of colloidal nanoparticles with different compositions, shapes, sizes, and morphologies.[7, 14-17] While the literature on the study of the these reaction conditions is extensive, there are still gaps in our understanding of how to select a nanoparticle composition best optimized for a given application, as well as ways to control surface structure in a deterministic fashion.

The benefits of understanding nanoparticle synthesis with respect to both the composition and shape/surface structure have been demonstrated in some remarkable examples of energy relevant catalysts. In these examples, Pt alloys, previously identified as being catalytically active, were grown as nanoparticles of specific shapes. Consequently, the already active Pt alloy materials had improved catalytic activity due to their shape. In the first example, cubic Pt-Cu alloy nanoparticles were studied as methanol and formic acid oxidation catalysts.[18, 19] In this particular synthesis, the composition of the final nanoparticles was determined by the ratio of the Pt(II) and Cu(II) acetylacetonate complexes used as precursors. The metal complexes were reduced to metal atom monomers by 1,2-tetradecanediol. The authors also determined that a small amount of dodecanethiol was required in order to control the reduction rate (i.e. monomer production rate) and form well mixed alloys. Shape control was provided by the capping ligands, tetraoctylammonium bromide (TOAB) and oleylamine. The Pt-Cu cubic nanoparticles were found to have improved catalytic activity for the oxidation of methanol and formic acid as compared to spherical Pt-Cu nanoparticles or pure Pt

nanoparticles. The improved activity is attributed to both the cubic shape, which exposes the more catalytically active (100) facet, and the presence of Cu, which adds a resistance to species capable of poisoning the catalyst.[18, 19] The example of Pt-Cu cubic nanoparticles clearly demonstrates the need to first understand what elemental compositions comprise the most active catalysts, followed by the need to develop ways to generate nanoparticles with a desired surface structure, because both composition and surface structure are important for catalytic activity. There are other similar examples in the literature of shape controlled nanoparticle synthesis of Pt alloys with Mn,[20] Ni,[21, 22] and Pd.[23] In all of these examples, a composition deemed to be catalytically active was found to have improved activity when synthesized as nanoparticles of a specific shape. Unfortunately, many of the current most active catalysts contain rare and expensive elements such as Pt, and there is little understanding on how to direct a nanoparticle synthesis so that a specific shape is produced. Therefore, the advancement of catalysis research relies on the ability to identify novel elemental compositions with improved catalytic activity and methods for controlling the shape of the nanoparticles comprised of those compositions in a deterministic fashion.

1.2 Scope

Based on the current state of the art, the projects presented in the following chapters focused on providing methods that lend themselves to a systematic approach for the identification and synthesis of nanoparticle catalysts with improved activity. The approach begins with identification of novel, catalytically active compositions through combinatorial methods. After the identification of the most active compositions, nanoparticles of those elemental compositions are synthesized with the most catalytically active surface structure.

The topics covered in the remaining chapters focus on key aspects of research that are still lacking in order for this approach to be fully realized. Based on the utility of combinatorial studies in the search for novel catalyst compositions, Chapter 2 discusses a synthetic method for generating combinatorial arrays of nanoparticles using colloidal nanoparticles as synthetic precursors. This novel synthetic method for combinatorial arrays will aid in future studies aimed at identifying nanoparticle compositions that are the most catalytically active. The final two chapters focus on the control of nanoparticle shape (i.e. surface structure). For example, the mechanism through which surface capping ligands control the shape of nanoparticles during a synthesis is not completely understood. Chapter 3 discusses the role of a popular capping ligand, octadecylphosphonic acid (ODPA), in the synthesis of anisotropic ZnO nanoparticles and provides insights that can be used in the development of new anisotropic nanoparticle syntheses. ZnO was studied based on the objective of developing a general understanding the growth of metal oxide nanocrystals rather than its relevancy as a catalytic material. Chapter 4 discusses a method to synthesize platinum nanoparticles with a predetermined facet exposed on the surface, using RNA as the surface structure directing capping ligand. Even though there have been many reports outlining methods for producing nanoparticles of various shapes and surface structures, the resulting shapes are often made fortuitously and there is still a need to be able to control shape and surface structure deterministically. Collectively, the lessons learned in these chapters have improved upon current methods for the identification and synthesis of colloidal nanoparticles with the most catalytically active compositions and surface structures, thus advancing the state of the art for energy relevant catalysts.

1.3 Background

1.3.1 Combinatorial Identification of Heterogeneous Catalysts with Optimized Compositions. Heterogeneous catalysts, or catalysts contained in a different phase than the reactants, exist in a huge parameter space when considering the number of possible combinations of elements in the periodic table. This nearly infinite diversity of materials has led many researchers to combinatorial methods as a means to identify new catalysts. As early as 1970, combinatorial methods of synthesizing materials were described as advantageous in materials discovery over traditional methods, which were only able to prepare one composition at a time.[24] Notable applications of combinatorial methods for heterogeneous catalyst discoveries were made in the late 1990s.[25] In these studies, libraries of materials were synthesized on surfaces in the form of arrays of transition metal or metal oxide thin films.[3, 25, 26] Many of the reports surveyed arrays of materials synthesized in the patterns based on the

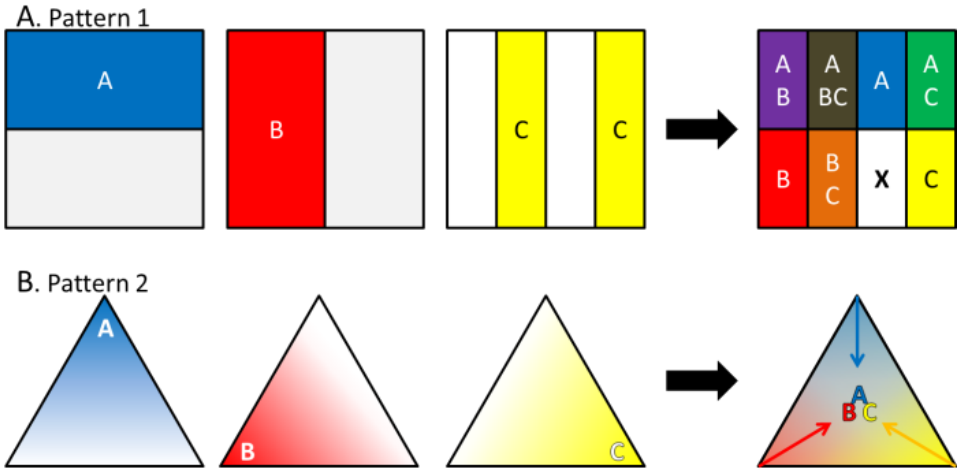

Figure 1.2. (A) Pattern 1: A general precursor pattern for the synthesis of a combinatorial array of elements A, B, and C. Additional elements can be added by overlaying additional elements and continuing the pattern. (B) Pattern 2: A general precursor pattern for the synthesis of a ternary combinatorial array in which the precursors for three elements are deposited in a gradient fashion from the three vertices of a triangle.

three element patterns shown in Figure 1.2. Pattern 1 depicts a method for constructing an array of elements A, B, and C in which the concentration of each element is not considered, only presence or absence. While Figure 1.2A depicts the combination of only three elements, it is apparent how it could be extended to additional elements by continually dividing each row/column in two, quickly making the arrays rather complex. Combinatorial arrays using patterns similar to Pattern 2 are also very common because they not only test the combination of the elements, but the concentration of each element as well. Arrays prepared according the scheme in Figure 1.2B are made by overlaying concentration gradients of each element to make a range of compounds containing different ratios of the three elements.

The first time a superior catalyst material was identified utilizing a combinatorial method was described in a report by Mallouk et al., in which combinatorial methodology identified a novel direct methanol fuel cell (DMFC) catalyst.[3] In that report, catalyst arrays were synthesized by using an ink jet printer to print metal salts in patterns similar to the one in Figure 1.2B, except the array was divided into discrete wells rather than a continuous gradient across a surface. The metal salts were then reduced with $NaBH_4$ to generate a library of zero-valent metal catalysts. Initial tests identified a ternary catalyst (Pt[62]/Rh[25]/Os[13]) that was slightly inferior to the state of the art at the time (Pt[50]/Ru[50]). However, the Pt/Rh/Os catalyst was positioned in a composition space of relatively inactive catalysts and thus theorized to be inactive.[3] That result was encouraging because it demonstrated the need for combinatorial studies by identifying active catalysts in compositions not able to be predicted from theory. The authors went on to apply the method to a quaternary array and identified a particularly active catalyst (Pt[44]/Ru[41]/Os[10]/Ir[5]) that was capable of doubling the short circuit

current density of the commercially available catalyst. The authors point out that this increased activity is despite the likely sub-optimal synthesis method that produced a catalyst with a surface area roughly half as large as the commercially available catalyst.[3]

Since that report by Mallouk, researchers have continued to use combinatorial methods in the search for heterogeneous catalysts. Bruce Parkinson's group also utilized ink jet printing in a combinatorial search for water splitting semiconductors.[26, 27] The catalyst arrays prepared in these studies were porous transition metal oxides formed from the thermal decomposition of metal nitrates printed on conductive supports in patterns similar to those in Figure 1.2B. The arrays were then attached as the working electrode to a potentiostat and screened for photocatalytic activity by scanning a visible light laser over the surface of the array and measuring the photocurrent. This produced a relatively high resolution photoelectrochemical activity map of the surface. The elemental composition of the active areas was then determined and the compounds could then be studied further. This method was successful in identifying an active cobalt oxide based mixed metal oxide ($Co_{2.52}Al_{0.18}Fe_{0.30}O_4$) with a nearly ideal band gap of 1.5 eV.[28] While this was not the "holy grail" of water splitting semiconductors, it was an encouraging find, and it inspired the formation of the SHArK program (Solar Hydrogen Activity Research Kit), which distributed the plans for kits to be used by undergraduate and high school students to screen libraries of metal oxides for active semiconductors.[29] Since the first reports of this method, other publications have provided even more sophisticated methods for screening metal oxide arrays produced by thermal decomposition of metals salts patterned by ink jet printing. Lewis et al. described a complex electrode capable of measuring photocurrent for hundreds of different compositions.[30] Bard et

al. have used a state of the art photo-electrochemical instrument utilizing a 200 µm optical fiber surrounded by a 35 µm thick gold ring electrode to measure photocurrent of ~300 µm diameter oxide spots with good resolution and sensitivity.[31-35] The sophistication of the screening methods of Parkinson, Lewis, and Bard described here is a testament to the maturity of the field with respect to the ability to analyze a combinatorial catalyst array.

The goal of the work presented in Chapter 2 was to improve upon the current combinatorial heterogeneous catalyst studies by developing a new method for synthesizing the combinatorial arrays. It was clear that the methods for identifying active catalysts have been improved upon over the past 15 years since the Mallouk paper,[3] but there have not been many reports improving on the synthetic methodology. Chapter 2 represents a relatively simple and advantageous way to synthesize combinatorial arrays that expands on the range of morphologies that the current synthetic methodologies are capable of synthesizing.

1.3.2 Shape Control of nanoparticles. Control of the final shape and surface structure of both metal and semiconductor nanoparticle colloids has been achieved by altering different aspects of the general synthesis scheme presented in Figure 1.1. Shape and surface structure are inherently linked and are dictated by the same processes during a nanoparticle synthesis. Therefore, the terms "shape" and "surface structure" are used somewhat interchangeably throughout this chapter and subsequent chapters. Unfortunately, there is no general method for controlling nanoparticle shape/surface structure, and the methods vary based on the chemistry of each given system.[13] However, several parameters have been shown to affect the final shape of nanoparticles in different synthesis schemes, including the phase of the seed particle, the monomer concentration during the growth period, and the surface energy of the

material.[17, 36] Basically, those parameters control the rate of addition of monomers to specific crystal facets during the growth process. The facets that have a high rate of monomer addition are covered, eventually reducing their abundance, and the facets with slow monomer addition remain exposed on the surfaces of the nanoparticles. The abundance of each crystal facet on the surface of the final nanoparticle defines its final shape.[13] The first parameter, the crystal phase of seed particle, has been shown to affect whether some nanoparticles grow isotropically or anisotropically. For example, when nuclei of MnS and CdS nanoparticles are formed in the cubic phase, such as zinc blend or rock salt, the crystals tend to grow isotropically, and when those nuclei are produced in the hexagonal wurtzite phase, the crystals tend to grow anisotropically.[17, 37]

The surface energy of the growing crystal also influences the final shape and surface structure of a nanoparticle. The equilibrium shape for crystalline nanoparticles involves a convolution of the minimization of surface area, with the anisotropic nature of the surface energy of various crystal facets.[38] Consequently, nanoparticles tend to be capped with facets with low Miller indices because the high energy, high index facets are quickly eliminated during crystal growth.[39] This leads to polyhedral nanoparticles with faces containing a mixture of low energy facets, and the abundance of each facet is dictated by their relatively small surface energy differences.[38] For example, it has been reported that the surface energy of the (00-1) facet of wurtzite semiconductor crystals is greater than the surface energy of (100) and (110) crystal facets.[17, 40] Therefore, it has been observed that wurtzite materials grow in rod shapes along the (00-1) axis because monomers tend to add to the higher energy facets during nanoparticle growth to reduce the total surface energy of the crystal.[17, 37] Control over the

relative energy differences between crystal faces has been achieved by the selective adhesion of surface capping ligands resulting in the selective stabilization of different crystal facets.[41] One example of this process is the synthesis of silver wires from the reaction of $AgNO_3$ with ethylene glycol in the presence of poly(vinyl pyrrolidone) (PVP). The PVP selectively binds to the (100) facet of the Ag seed nanoparticles leaving additional monomers to add to the (111) face, causing anisotropic growth in the ‹111› direction.[42]

The effect of monomer concentration on growth is illustrated in the example of wurtzite CdSe nanorods described in detail by Peng and Alivisatos and referred to as "kinetic control."[12, 14, 17, 43] The monomer concentration determines the diffusion rate of monomers to the surfaces of the crystal, or the monomer flux. At high monomer fluxes, monomers add to the high energy surfaces of the growing crystal. In the case of CdSe, this equates to addition along the (00-1) direction of the crystal causing one dimensional, anisotropic growth.[14] As the monomer flux decreases due to consumption of the monomers, the process converts to more isotropic growth mechanisms where the crystal grows in three dimensions. When the monomer concentration nears zero, the crystal growth enters a thermodynamic regime where the nanoparticles start to ripen, either by reducing the anisotropy or by Ostwald ripening.[17] The competition between kinetic and thermodynamic control during a nanoparticle synthesis has also been demonstrated for PbS nanoparticles, and was achieved by simply varying the temperature during the nanoparticle growth regime of the synthesis.[44] At high temperatures, the growth was under thermodynamic control, resulting in growth of the more thermodynamically stable, isotropic, truncated cube shaped particles. At lower temperatures

the growth was under kinetic control, resulting in growth along the higher energy ‹100› direction resulting in anisotropic nanorods.[17, 44]

While the examples described in this section demonstrate the level to which nanoparticle shape control is understood, there are still clear gaps in that understanding. The goal of the work presented in Chapter 3 was to understand how the capping ligand ODPA affects the anisotropic synthesis of ZnO nanoparticles and ultimately determine the mechanism of the anisotropic growth. The goal of the work in Chapter 4 was to utilize what is known about the selective adhesion mechanism of shape control and develop a ligand capable of binding one facet with a higher affinity than others, thereby directing the growth of the nanoparticle. The overall goal of the work in both of the final chapters was to add to the current state of the art on understanding anisotropic nanoparticle growth and how to deterministically control it.

1.3.3 Biomolecule Mediated Nanoparticle Synthesis. Nature has developed biological systems capable of synthesizing some remarkable nano-materials. For example, the bacterium *Magnetospirillum magneticum* synthesizes magnetic iron oxide nanoparticles, which it uses like a compass for navigation.[45] Using nature as inspiration, several different polymeric biomolecules (i.e. peptides, proteins, and nucleases) have been identified, isolated, and used *in vitro* to mediate or catalyze the synthesis of nano-materials.[46] For example, a 12 amino acid peptide (dubbed Ge8) was found in the Feldheim lab to mediate the formation of Ag nanoparticles and nanowires at neutral pH with the aid of room light.[47] A protein, the human H-chain ferritin cage, has been shown to mediate the formation of superparamagnetic iron oxide nanoparticles *in vitro*, and it forms a complex with the nanoparticle usable in medical imaging.[48] In another example of the utilization of biomolecules, surface bound arrays of

random sequence 12-mer deoxyribonucleic acid (DNA) molecules were used to identify sequences capable of mediating the formation of small fluorescent Ag nanoparticles.[49] These examples of biomolecules mediating the synthesis of nano-materials represent an exciting field of research developing novel and functional materials for many applications. What is even more interesting is that biomolecules often allow the synthesis of nano-materials at much milder conditions than what is normally required, such as room temperature and neutral pH.[50, 51] The bio-polymer ribonucleic acid (RNA) is of most interest to the work presented here. RNA is an interesting biomolecule for the synthesis of materials because of its ability to reproducibly fold into secondary structures. These secondary structures have been used to recognize and bind with specificity to the surface structure of proteins.[51] It has been hypothesized that the secondary structure could help RNA recognize inorganic material surfaces as well.[51] In fact, RNA has been used to control the size of semiconductor quantum dots during growth.[52-54] Therefore, RNA was chosen as the bio-polymer of interest for the work described in Chapter 4.

One of the powerful aspects of using biomolecules in materials synthesis is the ability to isolate active molecules with specific amino acid or nucleotide sequences from large biomolecule libraries through the process of *in vitro* selection.[51] Figure 1.3 illustrates the general scheme for *in vitro* selection.[55] The process starts with a large combinatorial library of biomolecules with

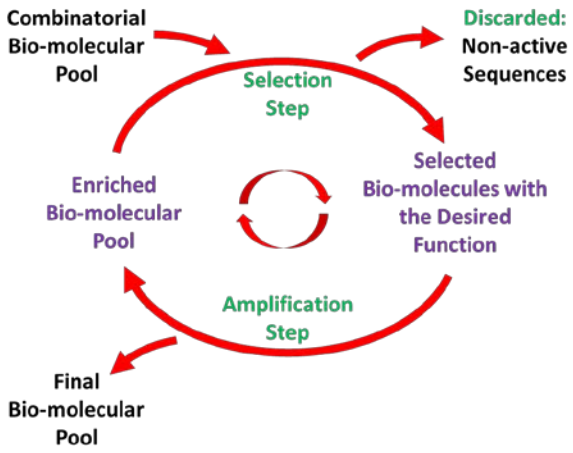

Figure 1.3. The general scheme for the in vitro selection of biomolecules starting with a highly combinatorial pool of random biopolymers.

random amino acid or nucleotide sequences that often contain 10^9 - 10^{14} different biomolecule sequences. The next step, the "selection step," is crucial and requires the ability to isolate the molecules from the library that perform a desired function while discarding all other "non-active" sequences.[51] The active molecules are isolated, and then amplified, generating a new library of molecules in which the ability to perform the desired function has been enriched. The selection step is repeated, further enriching the pool until a final pool of molecules with a high activity towards the desired function has been isolated. Early experiments following the scheme in Figure 1.3 were designed to isolate RNA sequences able to be replicated by the Qβ replicase protein, which is highly substrate specific.[55] The introduction of the polymerase chain reaction (PCR) was a significant development in the field of *in vitro* selection and allowed for the selection of RNA and DNA sequences with properties other than their ability to be amplified by a replicase protein.[55] Additionally, the enzymes used in PCR often have a 10^{-4} to 10^{-6} per nucleotide error rate, adding an evolutionary aspect to the process by mutating the pool during amplification and thus adding diversity.[55] Since that advancement, RNA has been selected through a process termed SELEX (Systematic Evolution of Ligands by EXponential enrichment) to bind with high affinity to proteins and small molecules with applications in the medical field.[56, 57]

The application of *in vitro* selection of RNA in materials synthesis is illustrated in some intriguing examples. RNA sequences, with modified uracil bases to improve their metal coordination ability, were selected in the Feldheim lab to mediate the formation of relatively large (~1 μm) Pd particles from organometallic complexes.[58] The RNA sequences were selected from a pool of 10^{14} unique RNA sequences, 87 bases in length, using the process in Figure 1.3.

The selection step was performed by mixing the RNA pool with the organometallic precursors and then isolating the sequences bound to Pd particles by size exclusion filtration. The bound RNA was then amplified and carried through to the next round. After several rounds, a pool of RNA capable of forming ~1 μm hexagonal plates was isolated.[58] Further study found that the particle shape formed by the RNA, was sequence dependent. Some of the sequences isolated as part of the selection mediated the formation of hexagonal plates while others mediated cubes.[59] Interestingly, the RNA was not only able to catalyze the formation of Pd particles from the organometallic precursors, but it was also able to mediate the final structure of the particles. Another uracil modified RNA selection performed in the Feldheim lab isolated sequences capable of mediating the formation of magnetic iron oxide nanoparticles.[60] In that experiment, the selection step required that the RNA was associated with magnetic material. This meant that the active sequences not only had to form an iron oxide particle, but in a morphology that was magnetically active, instead of one of the non-magnetic iron oxide morphologies.[60] The results of these two RNA selections prove that it is not only possible to select RNA sequences capable of mediating the formation of materials such as palladium or iron oxide, but it is also possible to control the morphology as well, such as in the production hexagonal disks or the polymorph, magnetite.

In light of the useful properties of RNA in materials synthesis, the goal of the work in Chapter 4 was to utilize those properties as selective adhesion ligands in Pt nanoparticle synthesis. The goal of the work was to select RNA sequences that bound with a higher affinity to one crystal facet of platinum over the others. Then, when that selected RNA was added to a

Pt nanoparticle synthesis, it would selectively adhere to that facet causing an enrichment of that facet in the final product.

1.4 Summary and Goals

The primary goal of the research presented in the following chapters was to provide some of the methods and understanding needed to systematically develop new nano-catalysts with applications in renewable energy. The activity of a nano-catalyst for a specific application requires the identification and synthesis of the most active composition and morphology. Ideally, the identification process would include the systematic screening of elemental combinations for the most active composition, and Chapter 2 outlines a new synthetic method for combinatorial arrays of nano-materials. Those compositions would then need to be synthesized as nano-catalysts in the most active morphology. Unfortunately, the current understanding of morphological control of nano-materials is incomplete. Therefore, Chapter 3 and Chapter 4 aim to improve the understanding of morphological control in an effort to make it more deterministic. Overall, the data presented in the following chapters mark an improvement in the understanding of the synthetic methods required to systematically develop new nano-catalysts.

1.5 References

1. Lewis, N. S.; Nocera, D. G., Powering the planet: Chemical challenges in solar energy utilization. *Proc. Natl. Acad. Sci. U. S. A.* 2006, 103, 15729-15735.

2. Alivisatos, P.; Cummings, P.; De Yoreo, J.; Fichthorn, K.; Gates, B.; Hwang, R.; Lowndes, D.; Majumdar, A.; Makowski, L.; Michalske, T.; Misewich, J.; Murray, C.; Sibener, S.; Teague, C.; Williams, E. *Nanoscience Research for Energy Needs. Report of the National Nanotechnology Initiative Grand Challenge Workshop, March 16-18, 2004*; 2004; p Medium: ED.

3. Reddington, E.; Sapienza, A.; Gurau, B.; Viswanathan, R.; Sarangapani, S.; Smotkin, E. S.; Mallouk, T. E., Combinatorial electrochemistry: A highly parallel, optical screening method for discovery of better electrocatalysts. *Science* 1998, 280, 1735-1737.

4. Bell, A. T.; Gates, B. C.; Ray, D.; Thompson, M. R. *Basic Research Needs: Catalysis for Energy*; PNNL-17214; Other: KC0302010; TRN: US200816673; 2008; p Medium: ED; Size: PDFN.

5. Feldheim, D. L., The new face of catalysis. *Science* 2007, 316, 699-700.

6. Hemminger, J. *New Science for a Secure and Sustainable Energy Future*; U.S. Department of Energy: 2008; p Medium: ED.

7. Burda, C.; Chen, X. B.; Narayanan, R.; El-Sayed, M. A., Chemistry and properties of nanocrystals of different shapes. *Chem. Rev. (Washington, DC, U. S.)* 2005, 105, 1025-1102.

8. Bonnemann, H.; Richards, R. M., Nanoscopic metal particles - Synthetic methods and potential applications. *Eur. J. Inorg. Chem.* 2001, 2455-2480.

9. Faraday, M., The Bakerian Lecture: Experimental Relations of Gold (and Other Metals) to Light. *Philosophical Transactions of the Royal Society of London* 1857, 147, 145-181.

10. Alivisatos, A. P., Perspectives on the physical chemistry of semiconductor nanocrystals. *J. Phys. Chem.* 1996, 100, 13226-13239.

11. Valden, M.; Lai, X.; Goodman, D. W., Onset of catalytic activity of gold clusters on titania with the appearance of nonmetallic properties. *Science* 1998, 281, 1647-1650.

12. Liu, H. T.; Owen, J. S.; Alivisatos, A. P., Mechanistic study of precursor evolution in colloidal group II-VI semiconductor nanocrystal synthesis. *J. Am. Chem. Soc.* 2007, 129, 305-312.

13. Polarz, S., Shape Matters: Anisotropy of the Morphology of Inorganic Colloidal Particles - Synthesis and Function. *Adv. Funct. Mater.* 2011, 21, 3214-3230.

14. Peng, Z. A.; Peng, X. G., Mechanisms of the shape evolution of CdSe nanocrystals. *J. Am. Chem. Soc.* 2001, 123, 1389-1395.

15. Ferrando, R.; Jellinek, J.; Johnston, R. L., Nanoalloys: From theory to applications of alloy clusters and nanoparticles. *Chem. Rev. (Washington, DC, U. S.)* 2008, 108, 845-910.

16. Li, Y.; Shen, W., Morphology-dependent nanocatalysis on metal oxides. *Science China Chemistry* 2012, 55, 2485-2496.

17. Jun, Y.-w.; Choi, J.-s.; Cheon, J., Shape Control of Semiconductor and Metal Oxide Nanocrystals through Nonhydrolytic Colloidal Routes. *Angewandte Chemie International Edition* 2006, 45, 3414-3439.

18. Xu, D.; Bliznakov, S.; Liu, Z. P.; Fang, J. Y.; Dimitrov, N., Composition-Dependent Electrocatalytic Activity of Pt-Cu Nanocube Catalysts for Formic Acid Oxidation. *Angewandte Chemie-International Edition* 2010, 49, 1282-1285.

19. Xu, D.; Liu, Z. P.; Yang, H. Z.; Liu, Q. S.; Zhang, J.; Fang, J. Y.; Zou, S. Z.; Sun, K., Solution-Based Evolution and Enhanced Methanol Oxidation Activity of Monodisperse Platinum-Copper Nanocubes. *Angewandte Chemie-International Edition* 2009, 48, 4217-4221.

20. Kang, Y. J.; Murray, C. B., Synthesis and Electrocatalytic Properties of Cubic Mn-Pt Nanocrystals (Nanocubes). *J. Am. Chem. Soc.* 2010, 132, 7568.

21. Zhang, J.; Yang, H. Z.; Fang, J. Y.; Zou, S. Z., Synthesis and Oxygen Reduction Activity of Shape-Controlled Pt3Ni Nanopolyhedra. *Nano Lett.* 2010, 10, 638-644.

22. Wu, J. B.; Zhang, J. L.; Peng, Z. M.; Yang, S. C.; Wagner, F. T.; Yang, H., Truncated Octahedral Pt3Ni Oxygen Reduction Reaction Electrocatalysts. *J. Am. Chem. Soc.* 2010, 132, 4984.

23. Yin, A. X.; Min, X. Q.; Zhang, Y. W.; Yan, C. H., Shape-Selective Synthesis and Facet-Dependent Enhanced Electrocatalytic Activity and Durability of Monodisperse Sub-10 nm Pt-Pd Tetrahedrons and Cubes. *J. Am. Chem. Soc.* 2011, 133, 3816-3819.

24. Hanak, J. J., The "multiple-sample concept" in materials research: Synthesis, compositional analysis and testing of entire multicomponent systems. *J. Mater. Sci.* 1970, 5, 964-971.

25. Jandeleit, B.; Schaefer, D. J.; Powers, T. S.; Turner, H. W.; Weinberg, W. H., Combinatorial materials science and catalysis. *Angewandte Chemie-International Edition* 1999, 38, 2495-2532.

26. Woodhouse, M.; Parkinson, B. A., Combinatorial approaches for the identification and optimization of oxide semiconductors for efficient solar photoelectrolysis. *Chem. Soc. Rev.* 2009, 38, 197-210.

27. Woodhouse, M.; Herman, G. S.; Parkinson, B. A., Combinatorial approach to identification of catalysts for the photoelectrolysis of water. *Chem. Mater.* 2005, 17, 4318-4324.

28. Woodhouse, M.; Parkinson, B. A., Combinatorial discovery and optimization of a complex oxide with water photoelectrolysis activity. *Chem. Mater.* 2008, 20, 2495-2502.

29. Osterloh, F. E.; Parkinson, B. A., Recent developments in solar water-splitting photocatalysis. *MRS Bulletin* 2011, 36, 17-22.

30. Katz, J. E.; Gingrich, T. R.; Santori, E. A.; Lewis, N. S., Combinatorial synthesis and high-throughput photopotential and photocurrent screening of mixed-metal oxides for photoelectrochemical water splitting. *Energy & Environmental Science* 2009, 2, 103-112.

31. Liu, G. J.; Liu, C. Y.; Bard, A. J., Rapid Synthesis and Screening of Zn(x)zCd(1-x)S(y)Se(1-y) Photocatalysts by Scanning Electrochemical Microscopy. *J. Phys. Chem. C* 2010, 114, 20997-21002.

32. Liu, G. J.; Bard, A. J., Rapid Preparation and Photoelectrochemical Screening of CuInSe2 and CuInMSe2 Arrays by Scanning Electrochemical Microscopy. *J. Phys. Chem. C* 2010, 114, 17509-17513.

33. Liu, W.; Ye, H. C.; Bard, A. J., Screening of Novel Metal Oxide Photocatalysts by Scanning Electrochemical Microscopy and Research of Their Photoelectrochemical Properties. *J. Phys. Chem. C* 2010, 114, 1201-1207.

34. Jang, J. S.; Lee, J.; Ye, H.; Fan, F. R. F.; Bard, A. J., Rapid Screening of Effective Dopants for Fe2O3 Photocatalysts with Scanning Electrochemical Microscopy and Investigation of Their Photoelectrochemical Properties. *J. Phys. Chem. C* 2009, 113, 6719-6724.

35. Lee, J. W.; Ye, H. C.; Pan, S. L.; Bard, A. J., Screening of photocatalysts by scanning electrochemical microscopy. *Anal. Chem.* 2008, 80, 7445-7450.

36. Zhou, K. B.; Li, Y. D., Catalysis Based on Nanocrystals with Well-Defined Facets. *Angewandte Chemie-International Edition* 2012, 51, 602-613.

37. Manna, L.; Scher, E. C.; Alivisatos, A. P., Shape control of colloidal semiconductor nanocrystals. *J. Cluster Sci.* 2002, 13, 521-532.

38. Sau, T. K.; Rogach, A. L., Nonspherical Noble Metal Nanoparticles: Colloid-Chemical Synthesis and Morphology Control. *Adv. Mater. (Weinheim, Ger.)* 2010, 22, 1781-1804.

39. Tian, N.; Zhou, Z. Y.; Sun, S. G.; Ding, Y.; Wang, Z. L., Synthesis of tetrahexahedral platinum nanocrystals with high-index facets and high electro-oxidation activity. *Science* 2007, 316, 732-735.

40. Zhang, H.; Huang, F.; Gilbert, B.; Banfield, J. F., Molecular Dynamics Simulations, Thermodynamic Analysis, and Experimental Study of Phase Stability of Zinc Sulfide Nanoparticles. *The Journal of Physical Chemistry B* 2003, 107, 13051-13060.

41. Yin, Y.; Alivisatos, A. P., Colloidal nanocrystal synthesis and the organic-inorganic interface. *Nature* 2005, 437, 664-670.

42. Wiley, B.; Sun, Y. G.; Xia, Y. N., Synthesis of silver wanostructures with controlled shapes and properties. *Acc. Chem. Res.* 2007, 40, 1067-1076.

43. Peng, X. G.; Manna, L.; Yang, W. D.; Wickham, J.; Scher, E.; Kadavanich, A.; Alivisatos, A. P., Shape control of CdSe nanocrystals. *Nature* 2000, 404, 59-61.

44. Lee, S.-M.; Jun, Y.-w.; Cho, S.-N.; Cheon, J., Single-Crystalline Star-Shaped Nanocrystals and Their Evolution: Programming the Geometry of Nano -Building Blocks. *J. Am. Chem. Soc.* 2002, 124, 11244-11245.

45. Arakaki, A.; Webb, J.; Matsunaga, T., A Novel Protein Tightly Bound to Bacterial Magnetic Particles in Magnetospirillum magneticum Strain AMB-1. *J. Biol. Chem.* 2003, 278, 8745-8750.

46. Akhtar, M. S.; Panwar, J.; Yun, Y.-S., Biogenic Synthesis of Metallic Nanoparticles by Plant Extracts. *ACS Sustainable Chemistry & Engineering* 2013.

47. Carter, C. J.; Ackerson, C. J.; Feldheim, D. L., Unusual Reactivity of a Silver Mineralizing Peptide. *ACS Nano* 2010, 4, 3883-3888.

48. Uchida, M.; Flenniken, M. L.; Allen, M.; Willits, D. A.; Crowley, B. E.; Brumfield, S.; Willis, A. F.; Jackiw, L.; Jutila, M.; Young, M. J.; Douglas, T., Targeting of Cancer Cells with Ferrimagnetic Ferritin Cage Nanoparticles. *J. Am. Chem. Soc.* 2006, 128, 16626-16633.

49. Richards, C. I.; Choi, S.; Hsiang, J. C.; Antoku, Y.; Vosch, T.; Bongiorno, A.; Tzeng, Y. L.; Dickson, R. M., Oligonucleotide-stabilized Ag nanocluster fluorophores. *J. Am. Chem. Soc.* 2008, 130, 5038.

50. Rouge, J. L.; Eaton, B. E.; Feldheim, D. L., Biomolecules in the synthesis and assembly of materials for energy applications. *Energy & Environmental Science* 2011, 4, 398-402.

51. Feldheim, D. L.; Eaton, B. E., Selection of biomolecules capable of mediating the formation of nanocrystals. *ACS Nano* 2007, 1, 154-159.

52. Ma, N.; Dooley, C. J.; Kelley, S. O., RNA-Templated Semiconductor Nanocrystals. *J. Am. Chem. Soc.* 2006, 128, 12598-12599.

53. Kumar, A.; Jakhmola, A., RNA-Templated Fluorescent Zn/PbS (PbS + Zn2+) Supernanostructures. *The Journal of Physical Chemistry C* 2009, 113, 9553-9559.

54. Kumar, A.; Jakhmola, A., RNA-Mediated Fluorescent Q-PbS Nanoparticles. *Langmuir* 2007, 23, 2915-2918.

55. Joyce, G. F., Forty Years of In Vitro Evolution. *Angewandte Chemie International Edition* 2007, 46, 6420-6436.

56. Tuerk, C.; Gold, L., Systematic Evolution Of Ligands By Exponential Enrichment - Rna Ligands To Bacteriophage-T4 Dna-Polymerase. *Science* 1990, 249, 505-510.

57. Dewey, T. M.; Mundt, A. A.; Crouch, G. J.; Zyzniewski, M. C.; Eaton, B. E., New Uridine Derivatives For Systematic Evolution Of Rna Ligands By Exponential Enrichment. *J. Am. Chem. Soc.* 1995, 117, 8474-8475.

58. Gugliotti, L. A.; Feldheim, D. L.; Eaton, B. E., RNA-mediated metal-metal bond formation in the synthesis of hexagonal palladium nanoparticles. *Science* 2004, 304, 850-852.

59. Gugliotti, L. A.; Feldheim, D. L.; Eaton, B. E., RNA-mediated control of metal nanoparticle shape. *J. Am. Chem. Soc.* 2005, 127, 17814-17818.

60. Carter, C. J.; Dolska, M.; Owczarek, A.; Ackerson, C. J.; Eaton, B. E.; Feldheim, D. L., In vitro selection of RNA sequences capable of mediating the formation of iron oxide nanoparticles. *J. Mater. Chem.* 2009, 19, 8320-8326.

Chapter 2. Synthesis of Combinatorial Nanoparticle Arrays

2.1 Introduction

The development of novel, more efficient materials for renewable energy applications relies heavily on the identification of nanoparticles (NPs) with optimized compositions.[1-3] Materials of one class, heterogeneous catalysts, have typically been discovered via trial and error methods in which a single composition hypothesized as an effective catalyst is subsequently synthesized and then tested for efficacy. Unfortunately, there is insufficient predicting power to design catalysts completely *a priori*, making serial synthesis and screening approaches impractical. Therefore, researchers have turned to parallel (combinatorial) screening methods to discover new materials. The goal of many of these combinatorial studies is to test vast numbers of elemental combinations typically starting with elements theorized to work well synergistically. While the composition parameter space is practically limitless, the synthesis method by which the elements are combined is often not ideal for producing some potentially highly effective nano-materials. The material libraries are typically synthesized by screen-printing or spotting solutions of metal salts on surfaces, and then exposing them to strong chemical reducing agents and/or high temperatures.[4-8] Even though this approach produces libraries of materials based in composition space, it provides limited control of the size, shape, and crystallinity of the materials. Specifically, these methods produce thin films of bulk materials instead of nano-structured materials. Consequently, the current synthetic methods for generating combinatorial arrays may be overlooking important nano-structured materials, and new ways of synthesizing nano-structured combinatorial arrays are required in the search for new catalysts.

The hypothesis of the research presented in this chapter was that using nanoparticles as precursors to generate combinatorial arrays of novel materials would give unprecedented control over their synthesis. Using nanoparticle as precursors could offer the ability to access materials that are not possible through traditional methods. Raymond Schaak's group has studied the use of NPs to synthesize an important class of solid-state materials, intermetallics. Intermetallics are stoichiometric metal alloys with a regular crystal structure and are typically synthesized by standard metallurgical techniques in which metal powders are exposed to high temperatures (typically >1000°C) for long annealing times (on the order of days or weeks).[9] Schaak et al. found intermetallics formed at much lower temperatures and shorter reaction times when the two elements were combined using nanoparticle as starting materials.[9-15] When NPs are used, atomic mixing can occur more rapidly and under milder conditions, because atomic diffusion distances are much shorter than when the starting materials particles are on the order of microns or larger. The ability to use milder conditions could allow the synthesis of materials that are not in the most thermodynamically stable morphology.

The initial objective of this project was to identify a method by which metal NPs of different elemental compositions could be arranged in a pattern on the surface of a substrate in such a way that they could be used as precursors for a combinatorial array. Combinatorial arrays, such as the ones reported by Parkinson et al. and described in Chapter 1, require the ability to establish concentration gradients of the elements of interest in opposing directions.[6] The concentration gradients described here were created by forming metal NP density gradients on the surface of a substrate. The NP arrays were assembled by electrostatically attaching anionic NPs to cationic surfaces. The gradients were characterized utilizing the strong

plasmon resonance absorbance that is observed in NPs of the noble metals gold and silver. After the nanoparticle density gradients were established, a series of experiments were conducted in order to understand the conditions under which the NPs could be forced to react and form an array of alloy NPs. The newly formed alloy NP array contained NPs with compositions based on the ratio of nanoparticle precursors in the surface density gradients. Essentially, a new synthetic method was established to utilize nanoparticle precursors to synthesize combinatorial arrays providing the benefits described by Schaak et al. to the synthesis.[12]

The second objective was to demonstrate the applicability of this synthetic method to generate a combinatorial array applicable to a catalyst screening procedure. Mallouk et al. presented a visual methanol oxidation catalyst screening technique that takes advantage of the localized pH drop caused by the oxidation half reaction and is visualized by a fluorescent pH indicator.[4, 5] This method was adapted in order to study the electrocatalytic activity of nanoparticle alloy arrays in the methanol oxidation reaction. Methanol oxidation is an important reaction for direct methanol fuel cells (DMFC) and a catalyst is required to improve the slow reaction kinetics of methanol oxidation.[16] Ru and Pt were chosen because they have been widely studied as methanol oxidation catalyst materials and it has been well documented that alloys of the two metals are a much better catalysts than either metal on its own.[17, 18] Indium tin oxide (ITO) coated glass slides with Pt and Ru NP arrays were fashioned into working electrodes, and these NP arrays were then used to demonstrate the ability of this method to generate combinatorial NP arrays able to be screened electrochemically.

2.2 Results and Discussion

2.2.1 Assembly of Au/Ag Gradient Arrays. Nanoparticle density gradients were prepared on transparent substrates using citrate stabilized Au and Ag NPs. The NPs were approximately 10 nm in diameter and were synthesized according to previously published aqueous methods.[19, 20] The citrate capping ligands gave the NP surfaces a net negative charge.[21] Glass substrates were prepared by thoroughly cleaning with piranha solution and then soaking in a solution of a cationic polymer, such as poly-L-lysine or poly-(diallyldimethylammonium chloride), to give the substrates a net positive charge. Based on these properties, when a cationic substrate placed in a solution of anionic NPs, the NPs slowly began to adhere to the surface. NP density gradients were prepared by taking advantage of the kinetics of adsorption of the anionic NPs to the cationic surface of the substrate.[21] Figure 2.1 shows a schematic of the experimental set-up by which this was accomplished. The substrates were exposed to a solution containing the NPs of interest at a controlled rate using a syringe pump. The portion of the slide oriented toward the bottom of the beaker remained in contact with the nanoparticle solution the longest and thus contained the highest density of particles. A constant flow created a linear density gradient across the slide, and changing the flow rate altered the slope of the gradient. Non-linear gradients

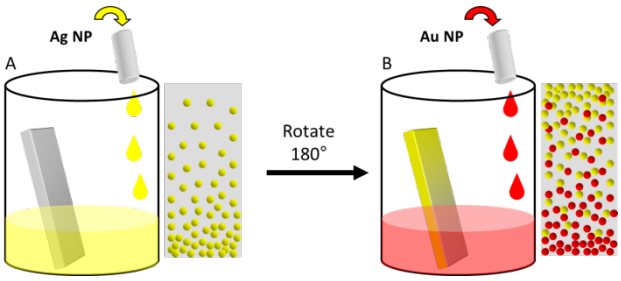

Figure 2.1. A schematic of the procedure used to assemble gradient NP arrays on transparent substrates. (A) A rectangular substrate with a cationic surface was placed vertically in a vessel and slowly exposed to a solution of negatively charged AgNPs. The result is a NP concentration gradient across the surface. (B) The substrate is placed vertically in another vessel with the opposite end down and an AuNP concentration gradient is assembled in the opposite direction.

were possible by altering the flow rate during a run. Turning the glass slide 180° with respect to the first gradient and repeating the procedure with NPs of a different metal, generated bidirectional NP gradients.

Gold and silver were used as proof of concept materials because of the unique visible absorption spectrum that is observed in NPs of those materials. Au and Ag NPs have intense plasmon resonance absorbances at well separated wavelengths (~400 nm for Ag and ~520 nm for Au).[22, 23] The NP gradients were deposited along the long axis of rectangular shaped glass substrates. Since the substrates were transparent to visible light, simply placing the sample in the beam of a UV-Visible spectrometer allowed the collection of a series of spectra along the length of the sample. The result is a series of spectra like the ones of an Au NP gradient in Figure 2.2A. The plasmon absorbance is clearly visible even though the NPs are in a single layer on the surface, as will be discussed later. This is due to the extraordinarily high extinction coefficients observed in gold and silver NPs which are on the order of 10^8 $M^{-1} \cdot cm^{-1}$.[21] Also apparent in Figure 2.2A is the control this method gives over concentration of NPs on the surface of the substrate. The plot in Figure 2.2B depicts a relatively linear slope of the peak height plotted versus position, as measurements are made traversing the substrate. Bidirectional nanoparticle gradients of both Au and Ag NPs could be characterized by UV-Visible spectroscopy due to the separation of the two metals' plasmon resonance absorbance peaks. Spectra were collected along the axis of a bidirectional nanoparticle gradient at the points illustrated in Figure 2.2C and the results are shown in Figure 2.2D. It is clear that as the slide is traversed, the plasmon absorption associated with Ag NPs reduces in intensity while the plasmon absorption associated with Au NPs increases in intensity. This data establishes the

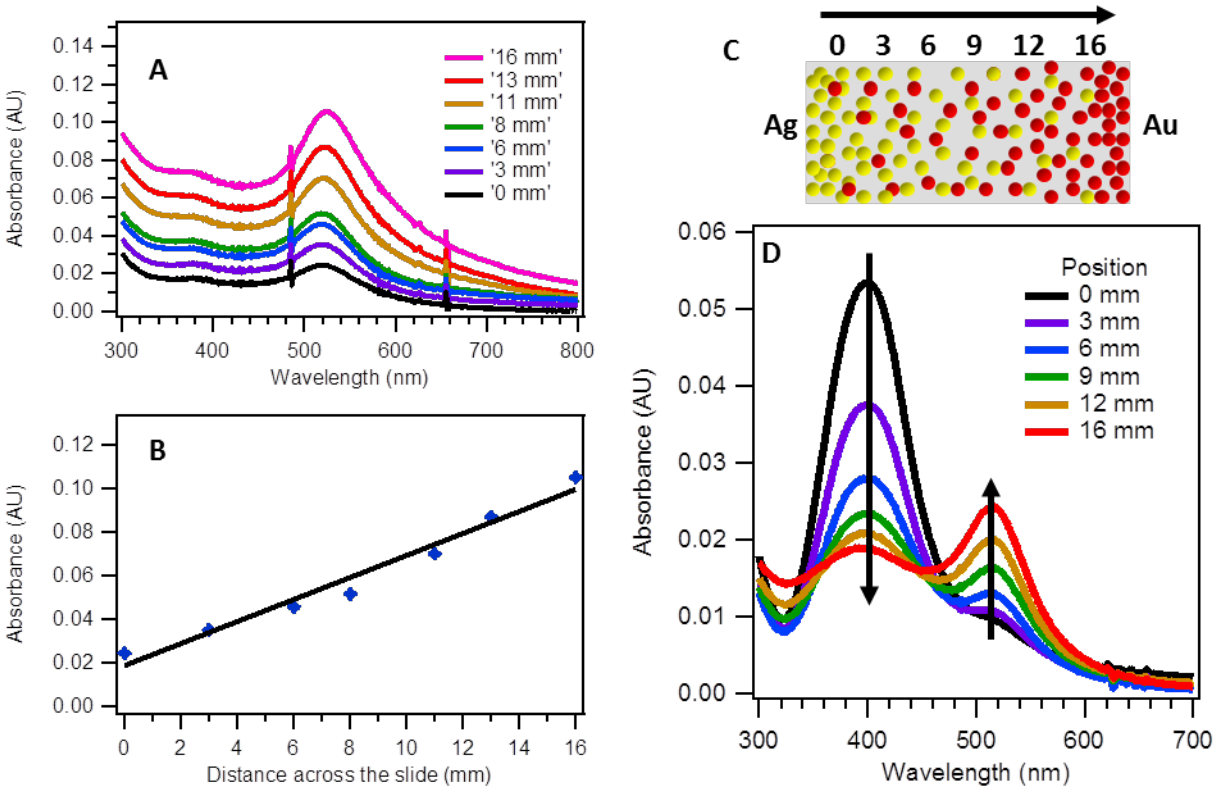

Figure 2.2. (A) UV-Visible spectra collected at points along the axis of an AuNP gradient assembled on a glass substrate. The AuNP plasmon absorbance (~520 nm) is visibly increasing as spectra are collected traversing the substrate. (B) A plot of the AuNP plasmon absorbance peak height versus distance across the substrate showing the linearly relationship between peak height and position. (C) A schematic of a bidirectional NP gradient showing the measurement points along the length of the slide. (D) UV-Visible spectra of a bidirectional Ag/Au NP gradient demonstrating the reduction in peak height of the AgNP plasmon (~400 nm) and the increase of the AuNP plasmon (~520 nm) as the substrate is traversed.

ability of this method to form multidirectional concentration gradients of the nanoparticle starting materials required for the synthesis of combinatorial arrays .

2.2.2 Alloying reaction. To generate arrays of alloys, a reaction step was required in order to promote the coalescing of adjacent NPs. Initial experiments were conducted with highly dense arrays of Au NPs on glass slides. When the nanoparticle surface density was high enough (i.e. a high concentration of NPs on the surface) the particles began to adsorb in clusters with NPs in very close proximity to each other. The effect is the red-shifted shoulder

observable in the spectrum of the initial array, shown as the blue trace in Figure 2.3A. This phenomenon has been reported many times in the past as a result of Au NP aggregation.[24, 25] An SEM image of a high nanoparticle density Au NP array deposited on indium doped tin oxide (ITO) coated conductive and transparent glass slides is shown in Figure 2.3B. In this image it is apparent that there are clusters of NPs in very close proximity to each other. Upon heating these samples in a muffle furnace at 350 °C there is a notable change in the plasmon resonance spectrum, as well as in the appearance of the particles on the surface. In Figure 2.3A, the spectrum of the annealed sample (red trace) became a sharp single peak with none of the observed proximity effects seen in the original spectrum. In the SEM image of the annealed sample (Figure 2.3C) it is readily apparent that new larger particles are present instead of clusters of smaller particles observed in Figure 2.3B. These results confirm that adjacent NPs on these surfaces (glass and ITO coated glass) do in fact

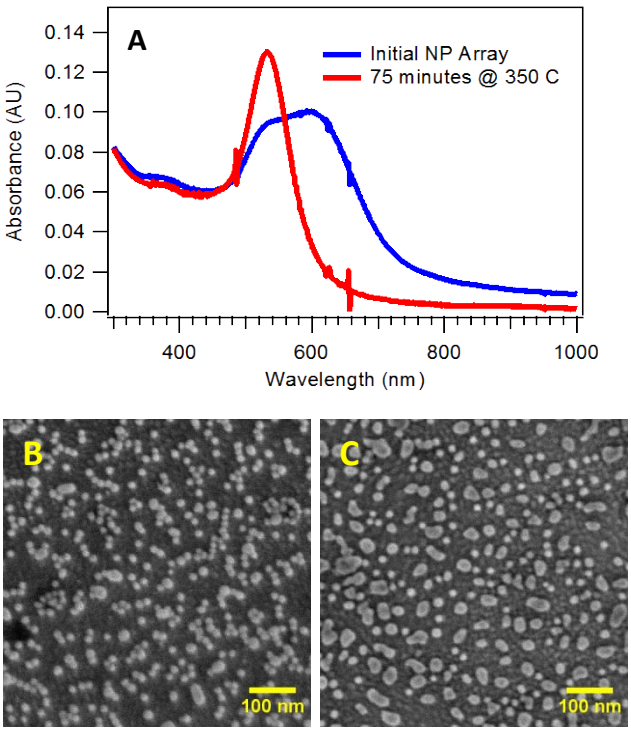

Figure 2.3. (A) UV-Visible spectra of an AuNP array on a glass substrate. The initial spectrum (blue trace) contains a plasmon peak with a red shifted shoulder often seen when AuNPs are in close proximity to each other or aggregated. After the AuNP array was heated for 75 minutes at 350 °C, the shoulder has disappeared (red trace). (B) An SEM image of an AuNP array on a ITO coated surface with a spectrum similar to the one shown as the blue trace in A. The NPs are clearly in aggregated clusters on the surface. (C) An SEM image after the AuNP array has been heated showing that there are no longer NP clusters on the surface and now some larger NPs are present demonstrating the coalescence of adjacent NPs up heating.

coalesce to form new, larger NPs. This is in contrast to other hypothesized scenarios in which the NPs would melt to form thin films or start to volatilize off the surface.

The next step of these experiments was to determine if heating the NP arrays comprised of Au and Ag NPs would cause the alloying of adjacent NPs. This was challenging because of the reactivity of Ag NPs with atmospheric oxygen.[26] When an array of Ag NPs was heated in an ambient atmosphere at 300 °C for one hour, the Ag plasmon absorbance disappeared. However, when the same experiment was performed on an Ag NP array sealed in a stainless steel tube under an argon atmosphere, the Ag NP plasmon remained. This finding ruled out the possibility that the disappearing Ag NP plasmon was caused by volatilization of the Ag and suggested the Ag was reacting with ambient oxygen forming a non-plasmonic material. Surprisingly, when Au/Ag alloy NPs that had been prepared in solution are adsorbed on a glass slide and then heated in atmospheric oxygen the plasmon resonance slowly shifts to that of Au, completely losing the Ag character. Figure 2.4 demonstrates this phenomenon for a sample of Ag/Au NPs with a starting plasmon peak at 437 nm. After 30, 60, 120, and 180 minutes at 350 °C in ambient atmosphere the plasmon peak has shifted to 443, 474, 503, and 515 nm respectively. This observation was explained by gradual oxidation of the silver atoms, causing them to no longer contribute to the plasmon resonance peak

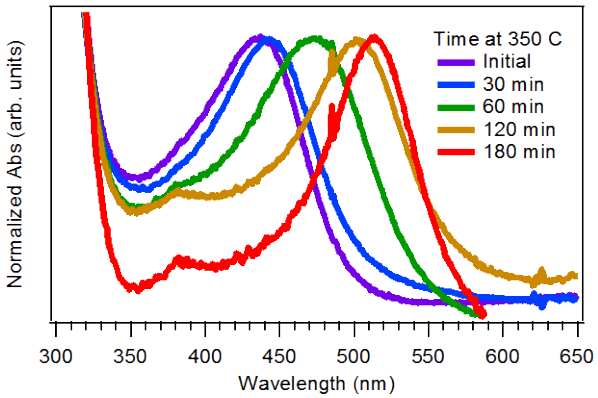

Figure 2.4. Spectra of Au/Ag alloy NPs assembled on the surface of a glass substrate. Spectra were collected as the samples heated at 350 °C in ambient atmosphere or 0, 30, 60, 120, and 180 minutes. The plasmon red shifts as the sample is heated demonstrating the oxidation of Ag due to ambient oxygen in the atmosphere

position. These results made it clear that an inert atmosphere would be required in order to synthesize combinatorial arrays containing Ag.

Alloying of the surface bound NPs was first achieved by heating the substrates in a muffle furnace with the samples sealed under and argon atmosphere inside a stainless steel tube. The resulting NP alloys were characterized based on the remarkable property of Au/Ag alloy NPs, where the λ_{max} of the plasmon resonance is a linear combination of the plasmon peak positions for the two materials based on the mole fraction of Au and Ag.[27] In other words, the peak position of Au/Ag alloy NPs plasmon resonance varies with composition such that, as the mole fraction of Au is decreased the plasmon resonance peak decreases from 520 nm (X_{Au}=1, X_{Ag}=0) to 400 nm (X_{Au}=0, X_{Ag}=1). This happens in a linear fashion, meaning a 0.5:0.5 alloy would have a plasmon resonance peak at 460 nm. In the sample characterized by the spectra in Figure 2.5A&B, a reaction time of 4.5 hours at 400°C in an argon atmosphere led to the disappearance of the individual plasmon resonances of Au and Ag NPs and the appearance of a single peak at each position on the slide indicating alloys had formed. Figure 2.5A shows the spectra collected of the original NP gradient, while Figure 2.5B presents the spectra collected of the sample after the argon atmosphere reaction. The spectra in Figure 2.5B have been normalized so that the shifting plasmon is more readily apparent. The λ_{max} of each spectrum was then used to determine the mole ratio of gold and silver in the alloys at each position. A plot of composition versus sample position (Figure 2.5C) demonstrates that it was possible to gain good control over composition using this method. The range of this particular composition gradient was from a X_{Au} of nearly 1 to X_{Au} of approximately 0.2 and the slope of the plot is linear with respect to distance across the substrate. These data have proven that the

process described here could be used in constructing NP arrays with compositional gradients of Au/Ag alloys that could be utilized in a combinatorial study. It was then of interest to determine the steps involved in the nanoparticle alloying process so that the reaction could be further optimized with respect to time and temperature.

During the course of the experiments described above, there were several indicators that nanoparticle mobility on the surface was the rate-limiting step for these reactions. It was found that a high surface particle density was required in order for the alloying to be complete. This is evidenced by the shoulders observed in the initial spectra of the gradient in Figure 2.5A. It was not possible to get complete alloying (i.e. two distinct plasmon peaks were still apparent after the reaction) unless these shoulders were observed in the initial spectra. Further examination of the self-diffusion constants of

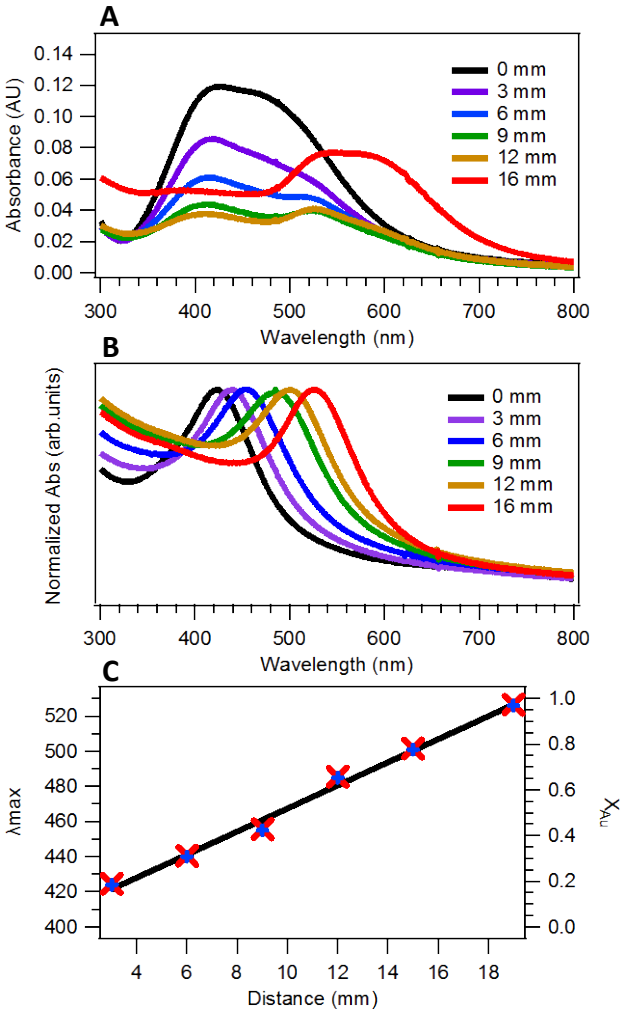

Figure 2.5. (A) UV-Visible Spectra of a bidirectional Au/Ag NP array on a glass substrate taken at regular points across the substrate. (B) Normalized UV-Visible spectra taken at the same positions on the substrate after it had been heated at 400 °C for 4.5 hours sealed under argon in a stainless steel tube. As the ratio of Ag:Au shifts from 1 to 0 the plasmon absorbance peak shifts from 400 nm to 520 nm as would be expected for a gradient of alloy NPs. (C) A plot of the plasmon peak position versus the position the spectrum was collected on the substrate (left axis). The data has been converted to mole fraction of Au on the right axis. There is a linear relationship between composition and position.

gold atoms in the bulk led to the conclusion that 4 hours was much longer than what would be required for atoms of gold and silver to mix at 400°C. Experimentally it has been determined that gold atoms diffuse through bulk gold according to Equation 2.1.[28]

Equation 2.1[28]

$$D = (0.031 \pm 0.004) e^{\left(\frac{-39360 \pm 280}{RT}\right)} \frac{cm^2}{sec}$$

Using that equation, it was calculated that gold atoms would have been able to diffuse, on average, 120 nm through the bulk after 4 hours at 400°C. This is a very conservative estimate, because it has been reported that metal atoms diffuse through NPs with rate constants many orders of magnitude higher than what is observed in the bulk.[29] Therefore, atomic mixing of adjacent NPs was not likely to be the slow step for alloying. This leaves the rate-limiting step as the rate at which the whole NPs diffused across the surface of the substrate to come into contact with each other. After coming into contact the NPs would then coalesce and mix relatively quickly. The conclusion was that identification of a method to increase the mobility of NPs on the surface of the slide would decrease reaction times and temperatures.

One method employed to improve NP mobility on the surfaces was to use a solvent as the reaction medium. Reactions were therefore performed by submerging the NP gradient sample in the solvent, purging with argon, and heating to the solvent's boiling point. Glycerol was the first successful solvent tested, reducing the reaction time to 1 hour and the temperature to glycerol's boiling point of 290°C (Figure 2.6A&B). Figure 2.6C contains SEM images of an ITO coated glass slide with gold and silver NPs adsorbed to the surface both before and after heating in glycerol. It is apparent that the particles remain adhered to the surface of the slide and are larger in size.

While glycerol was found to work well, other solvents were also tested in order to ascertain what properties of the solvent were important. To accomplish this, a series of solvents with varying boiling points and polarities were tested. Diphenyl ether was also capable of supporting the alloying reaction with a reaction time of 4 hours at its boiling point of 259 °C (Figure 2.7). These two solvents contrast in the fact that glycerol is very hydrophilic while diphenyl ether is hydrophobic, suggesting that the role they play in the reaction has more to do with their physical properties, such as boiling point and viscosity, rather than their chemical functionality. To test this hypothesis other solvents, such as 2-phenoxy ethanol (bp 247 °C), propylene carbonate (bp 240 °C), tetra-ethylene glycol (bp 314 °C), dimethyl sulfoxide (bp 189 °C), and ethylene glycol (bp 197 °C) were tested. None of these solvents were found to be able to successfully alloy

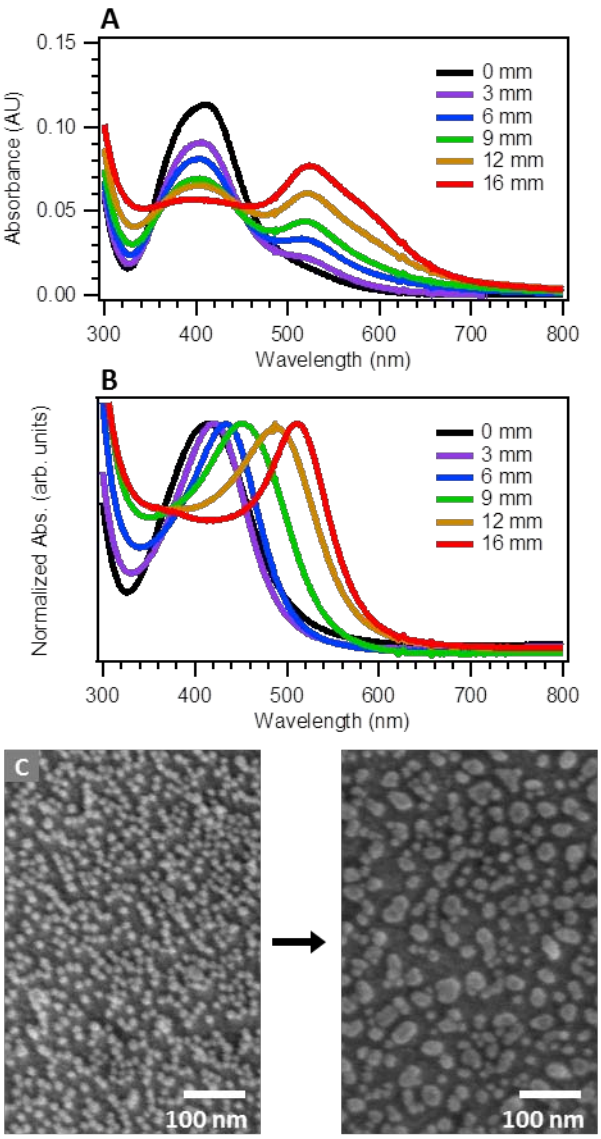

Figure 2.6. (A) UV-Visible Spectra of a bidirectional Au/Ag NP array on a glass substrate taken at regular points across the substrate. (B) Normalized UV-Visible spectra taken at the same positions on the substrate after heating in argon purged boiling glycerol (290 °C) for 1 hour. A single peak is observed at each position indicating complete alloying has occurred at this shorter reaction time and lower reaction temperature. Below are SEM images of ITO coated substrates containing Au and Ag NPs before (C) and after (D) heating in argon purged boiling glycerol (290 °C) for 1 hour.

the NP gradients under the testing constraint of 8 hours of boiling. For each test, the flask containing the sample and the solvent was purged with argon and then heated to the solvent's boiling point. While the exact reasons for the failure of most of the solvents was not ascertained, observation of the boiling points suggests that there is a specific temperature range under which the alloying process works the best. For all of the solvents with boiling points under that of diphenyl ether (<259 °C), two plasmon resonances remained in the post reaction spectra. The exception to this was propylene carbonate, which appeared to oxidize the silver, similar to what was observed with heating in ambient atmosphere. This was either due the inability to purge oxygen from the solution by bubbling argon gas through it, or because propylene carbonate itself reacts with the silver. For the one solvent tested with a boiling point above that of glycerol, tetraethylene glycol (bp 314 °C), the NPs appeared to become dislodged from the substrates even after boiling for times as short as 30 minutes. Therefore, the required properties of solvents capable of successfully supporting the surface alloying reaction are that the boiling points lie in the range of ~259 °C – ~290 °C and inert with respect to the metal NPs.

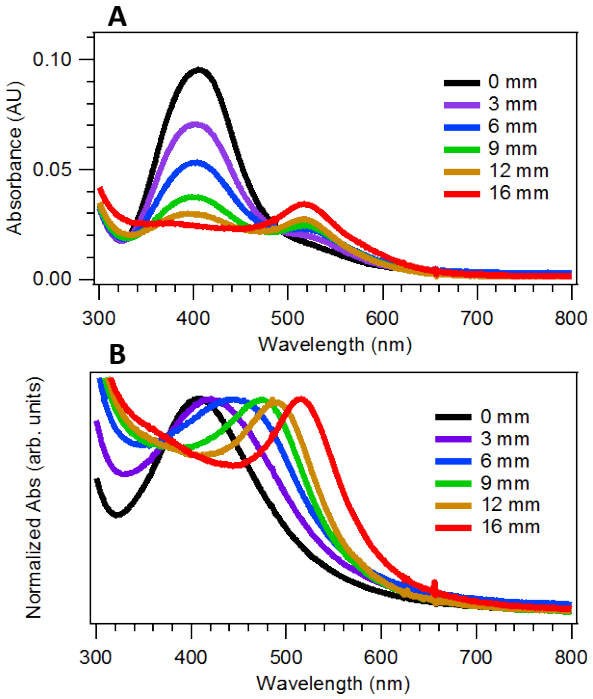

Figure 2.7. (A) UV-Visible Spectra of a bidirectional Au/Ag NP array on a glass substrate taken at regular points across the substrate. (B) Normalized UV-Visible spectra taken at the same positions on the substrate after it had been heated in argon purged diphenyl ether for 4 hours at its boiling point (259 °C). A single peak is observed at each position indicating complete alloying has occurred.

In addition to the requirement of the boiling point of the reaction solvent to be within a specific range, it was also determined that the solvent needed to be vigorously boiling in order for complete alloying to take place. A set of experiments outlined in Table 2.1 reveal the necessity of a boiling reaction solution. In these reactions, gradient arrays were heated in solvents at temperatures below their boiling point but equal to the reaction temperature of a successful reaction. For example, diphenyl ether could successfully support the alloying of an Ag/Au gradient when heated to its boiling point of 259 °C for 4 hours. However, when an Ag/Au gradient was heated in glycerol (bp 290 °C) at 259 °C for 4 hours, complete alloying was not observed. The same was true when the reaction was attempted in tetraethylene glycol (bp 314 °C) at the boiling point of glycerol (290 °C) for one hour. A possible explanation is that the surface bound NPs become nucleation sites for the formation of vapor bubbles in the solvent, thus mechanically moving the particles across the surface and into contact with each other. In fact, adding boiling stones to the reaction vessel along with the sample increased reaction times required for complete alloying. In other words, additional gas bubble nucleation sites in solution appear to reduce the benefit of the boiling solvent by providing additional sites other than the NPs for the vapor bubbles to nucleate. This evidence supports that the NPs are acting as vapor bubble nucleation sites during solvent boiling and that action is important for NP

Table 2.1. Solvents used as the reaction medium for alloying of Au/Ag bidirectional NP gradients

Solvent	Boiling Point	Reaction Temp.	Vigorous Boiling?	Alloying Complete?
Glycerol	290 °C	290 °C	Yes	Yes
Diphenyl Ether	259 °C	259 °C	Yes	Yes
Tetra(ethylene) glycol	314 °C	290 °C	No	No
Glycerol	290 °C	259 °C	No	No

surface mobility.

Described in this section were methods for converting assembled arrays of precursor nanoparticles into arrays of nanoparticle alloys. It was found that in the case of silver, and likely in the case of many other metals, an inert atmosphere was required in order to avoid a reaction with atmospheric oxygen. This result does, however, suggest a route to mixed metal oxides, nitrides, and sulfides. Those compounds could possibly be synthesized using subsequent heating steps of alloy nanoparticle arrays in atmospheres containing oxygen, a nitrogen containing gas such as ammonia,[30] or a sulfur containing gas such as H_2S,[31] respectively. These compounds are currently of substantial interest for their renewable energy applications in catalysis and photovoltaics.[30-32] To generate NP alloy arrays from precursor NP arrays with high NP densities, it was possible to simply anneal the array in a muffle furnace under an argon atmosphere. In order to reduce alloying reaction times and temperatures, the arrays could be heated in solvents under specific conditions. With the reaction taking place under these milder conditions, this route could enable the formation of combinatorial arrays of materials composed of difficult to synthesize morphologies, such as the ones described by Schaak et al.[10, 12, 14, 31]

2.2.3 Identification of Electrocatalysts. A catalyst assay was developed in order to assess the ability of the synthesis method described above to generate combinatorial arrays that could be screened for catalytic activity. The assay was developed to evaluate the catalytic activity of materials in the methanol oxidation reaction (Equation 2.2), which is an important reaction for the direct methanol fuel cell (DMFC).[16]

Equation 2.2

$$CH_3OH + {}^3/_2\ O_2 \rightarrow CO_2 + 2\ H_2O$$

While the oxidation of methanol to carbon dioxide and water is thermodynamically favored ($\Delta G° = -702\ kJmol^{-1}$), a catalyst is required in order to speed up the reaction kinetics for utilization in a DMFC.[16] Platinum and specifically platinum NPs (Pt NPs) have been found to be good catalysts for DMFCs. Consequently, Pt NP catalysis of the methanol oxidation reaction has been reported extensively in the literature.[33-38] Due to the high cost of Pt and the continuing effort to develop more efficient catalysts, many reports have discovered that Pt alloys are more ideal catalysts.[16, 17, 39] One such alloy that has been reported to be particularly efficient was the alloy of Pt with Ru. [17, 18] These results provide a good test case for the synthesis method described in the previous section. Both Pt and Ru NPs were synthesized with anionic capping agents (citrate and acetate, respectively) like the Au and Ag NPs discussed above. Therefore, patterns of Pt and Ru NPs were easily prepared on the surface of ITO coated glass, and then those substrates were fashioned into electrodes for electrochemical experiments.

Electrochemical experiments were conducted using the configuration outlined in Figure 2.8A. The nanoparticle array on ITO coated glass was connected as the working electrode in a standard three electrode configuration. The working electrode was constructed by attaching an insulated copper wire to the surface of the ITO glass using conductive silver epoxy and then insulated from the electrolyte solution using standard epoxy. The construction of the working electrode can be seen in Figure 2.8B, along with the placement of the Pt wire auxiliary electrode and the Ag/AgCl reference electrode. In this experiment the current observed at the surface of the working electrode could be measured while sweeping the potential towards oxidizing potentials (positive) versus the Ag/AgCl reference electrode. The test solution contained 6 M methanol and 0.5 M $NaClO_4$ as the supporting electrolyte. A way to visualize

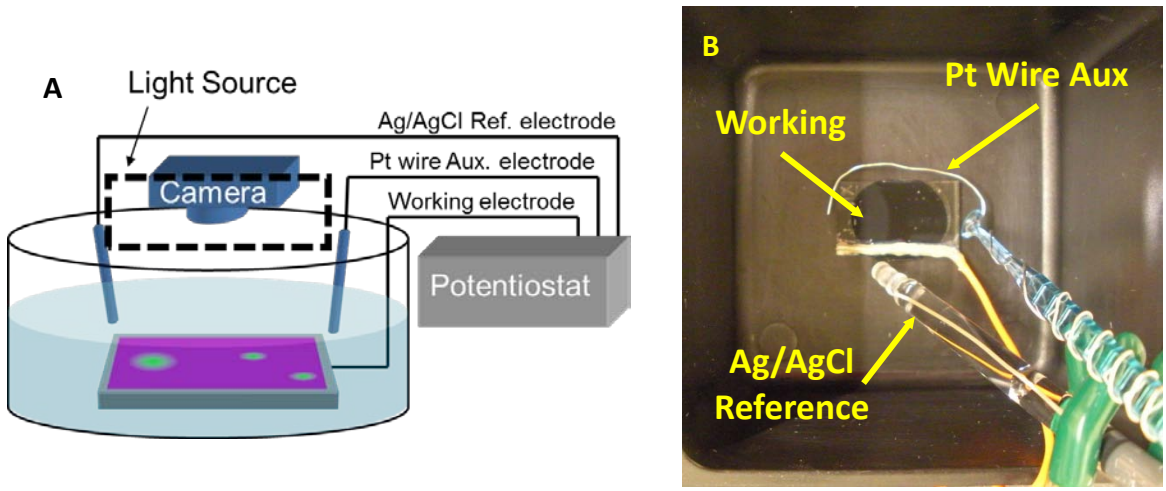

Figure 2.8. (A) A schematic of the three electrode electrochemistry experiment used to evaluate surface bound NP arrays on ITO coated glass. A digital camera and a UV lamp were positions directly above the sample in order to visualize and observe the pH indicator. (B) An image of the electrode positioning for the experiments. The working electrode (NP array on ITO coated glass) was adhered to the bottom of a dark opaque dish with vacuum grease and the reference/auxiliary electrodes were positioned closely to the working electrode.

methanol oxidation occurring at the surface of an electrode was adapted from the visualization method developed by Mallouk.[4, 5] Quinine was added to the electrolyte solution (100 µM quinine) and was used as a pH indicator. When the methanol oxidation half reaction, shown in Equation 2.3, takes place at the surface of an electrode, it is associated with a localized pH drop because the six electron oxidation also produces six protons.

Equation 2.3

$$CH_3OH + H_2O \rightarrow 6H^+ + CO_2 + 6\,e^-$$

The localized pH drop could be easily visualized by the fluorescent pH indicator quinine. At neutral pH quinine is not fluorescent under UV irradiation (365 nm), but at pH values below its pKa, the molecule is protonated and becomes fluorescent emitting green/blue light at approximately 450 nm (Figure 2.9).[4, 40, 41] Therefore, as the potential is swept in the positive direction fluorescence was seen above areas of the array where the oxidation half reaction was

taking place. The fluorescence was then visible first above the most active catalysts on the electrode during the scan. Less efficient catalysts would begin to fluoresce at higher overpotentials as the scan continued. Since the fluorescence is in the visible spectrum, a standard digital camera was used to acquire images of the array capturing the fluorescence.

Control experiments were performed to assure the design of the experiment was sound. The catalytic activity of the ITO coated glass towards the methanol oxidation reaction was tested and found not to be active (i.e. no fluorescence was observed) when the potential was scanned between 0 and 1000 mV (vs. Ag/AgCl). NPs of Pt and Ru were adsorbed separately onto half of two separate ITO electrodes in the pattern seen in Figure 2.10A. Both electrodes exhibited florescence above the portion of the slide containing NPs as the potential was scanned

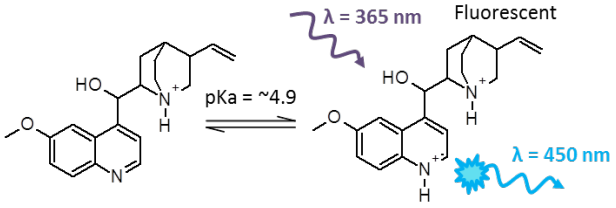

Figure 2.9. The chemical structure of quinine used to visualize the pH drop associated with the methanol oxidation half reaction shown as Equation 3. When the pH of the solution is above its pKa (~4.9) the molecule is deprotonated and is not fluorescent under UV radiation (left). When the pH is below its pKa the molecule is protonated and become fluorescent emitting visible blue/green light.

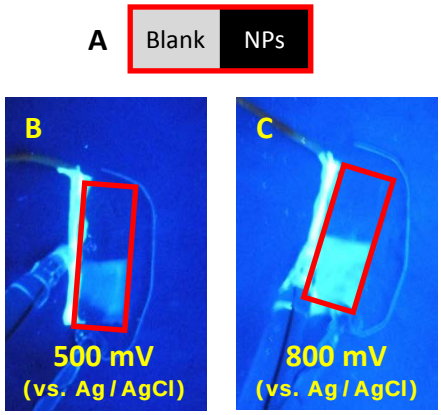

Figure 2.10. (A) A schematic of the configuration of the NP arrays used as the control samples for the electrochemistry experiments. One side of the sample was blank ITO while the other side contained the NPs of interest (Ru or Pt). (B) The fluorescence observed above PtNPs at 500 mV vs. Ag/AgCl as the potential was scanned at 10 mV/s in the positive direction. (C) The fluorescence observed above Ru NPs at 800 mV vs. Ag/AgCl as the potential was scanned at 10 mV/s in the positive direction.

in the positive direction while the solution above the bare ITO did not fluoresce. Fluorescence was observed above the Pt NPs at lower potentials than the Ru NPs (Figure 2.10B&C), as would be expected from information in the literature.[16]

To test the synthesis of alloys, Pt and Ru NPs were deposited in a three section pattern so as to allow a comparison between each metal individually and the mixture of the two, according to the diagram in Figure 2.11A. Two NP arrays were prepared. The first array was

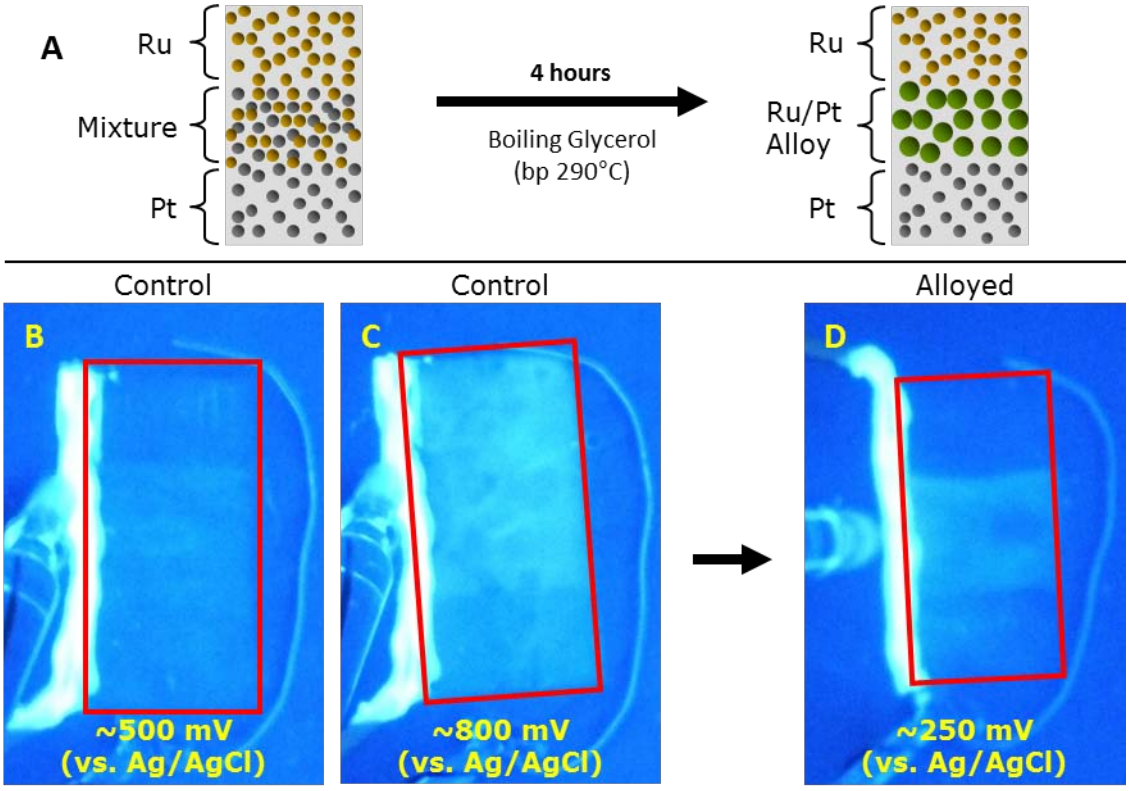

Figure 2.11. (A) A schematic of the NP arrays used to test the effect of alloying Pt and Ru NPs on the surface of an ITO coated slide. The NPs were arrays in a three section patter such that either end of the array contained Pt and Ru NPs separately and the center section contained both particles. The array was then subjected to argon purged boiling glycerol for 4 hours generate Ru/Pt alloys NPs in the center section. (B) Quinine florescence observed the entire Pt section of the pre-alloyed array in the forward scan (10 mV/s) upon reaching 500 mV vs. Ag/AgCl. (C) Quinine florescence observed the entire pre-alloyed array in the positive scan (10 mV/s) upon reaching 800 mV vs Ag/AgCl. (D) Quinine florescence observed above the center Ru/Pt alloy section of the array during the positive scan upon reaching 250 mV vs. Ag/AgCl.

not subjected to any more treatment after the NPs were attached (control). The second NP array was reacted in glycerol at its boiling point (290 °C) for 4 hours. Figure 2.11 summarizes the results of these experiments. As the electrode potential was scanned positive for the control slide, the entire Pt section of the slide fluoresced at lower potentials (~500 mV vs. Ag/AgCl, Figure 2.11B) and the Ru section began to fluoresce at higher potentials (~800 mV vs. Ag/AgCl, Figure 2.11C). There was no differentiation between the center section containing the mixture of the two metals and the ends of the slide that contained just one metal. The second electrode that had been reacted in boiling glycerol for four hours had a different electrochemical profile. During the positive scan, the center section, presumably containing Pt/Ru alloys, began to fluoresce first (~250 mV vs. Ag/AgCl, Figure 2.11D), followed by the Pt section, and finally the Ru section. The observation that the post alloying section of the array containing both Pt and Ru was a better catalyst than that same section of the non-alloyed slide helps to confirm the alloying results from above for the Ag/Au NP arrays. Unlike the Ag/Au arrays, Pt and Ru NPs do not have a spectroscopic signature that could be used to confirm alloying, therefore the catalysis assay was used. As has been reported previously in the literature, the alloy of Pt and Ru was a better catalyst than either of the metals on their own.[16]

2.3 Conclusions and Future Directions

The data reported in this chapter describe a novel method for the synthesis of combinatorial NP arrays from precursor NPs. Surface-bound NP gradients of two different metals (Au and Ag) were converted into NP arrays with a composition gradient that varied linearly from one side of the substrate to the other. These alloys were formed from the individual metal precursors using relatively mild conditions. The reaction was found to be

complete after 4.5 hours at 400 °C in an inert atmosphere. Heating the gradient arrays in argon purged solvents enabled the reduction of reaction time and temperature, likely due to increased surface mobility of the NPs in those media. Glycerol and diphenyl ether were found to best support the reaction, under the caveat that the solvents were vigorously boiling. Proof that this method for synthesizing NP alloy arrays could be used in the production of material arrays for combinatorial studies was demonstrated for the methanol oxidation reaction using Pt and Ru. Literature results stating alloys of Pt and Ru were more efficient methanol oxidation cataylsts were confirmed.

Future experiments in this field could focus on two areas. First, further study is needed to determine the resolution of the synthetic method. It is still unclear how many nanoparticles coalesce during the alloy reaction. If a very narrow size distribution of precursor nanoparticles were used to form alloy nanoparticle arrays, then statistics on the composition of individual nanoparticles would reveal the resolution of the method. However, if there was a large spread in the number of nanoparticles that coalesced in the alloying process, this determination would be difficult. One way of ascertaining this information would be high resolution elemental mapping, which was not possible with available instrumentation. Understanding resolution aspect of the synthetic method would allow for improvement in its design with respect to the surface density of the starting nanoparticle gradients and reaction conditions.

The second direction for future work in this area would be to apply this synthetic method to the search for novel catalyst materials. This method could easily be applied to the testing scheme developed by Parkinson. By patterning arrays of nanoparticles of catalytically relevant metals, combinatorial arrays could be prepared and analyzed using the same

photocurrent scanning technique. Hypothetically, this method would have the advantage of producing a variety of morphologies that the current harsh methods of synthesizing combinatorial arrays cannot do, as described in Chapter 1. Considering the established correlation between a catalyst's morphology and its activity, this synthetic method could be an important advancement in the field.

2.4 Experimental

2.4.1 Chemicals and materials. Tetrachloroauric acid ($HAuCl_4$, 99.999%), citric acid trisodium salt ($Na_3C_6H_5O_7$, anhydrous), sodium borohydride ($NaBH_4$, 99.99%), poly(diallyl-dimethylammonium chloride) (PDDA, MW 100,000 – 200,000, 20% in water), poly-L-lysine hydrochloride (MW >30,000), monosodium phosphate ($NaHPO_4$), hydrogen peroxide (H_2O_2, 30%), ruthenium(III) chloride ($RuCl_3 \cdot xH_2O$, 99.98%), ITO coated glass (70-100 Ω/sq), (3-aminopropyl)trimethoxysilane (APTMS, 97%), Hydrogen gas (99.99+%), and sodium perchlorate ($NaClO_4$, 98%) were purchased from Sigma Aldrich. $AgNO_3$ (certified ACS grade) and sodium chloride (NaCl) were purchased from Fisher. K_2PtCl_4 (46.5-47.0% Pt) was purchased from Acros. Sodium acetate and concentrated sulfuric acid (H_2SO_4) were purchased from Mallinckrodt. Conductive epoxy (silver epoxy, PN: CW2400) was purchased from Circuit Works. Quinine (purum for fluorescence, 98%) was purchased from Fluka. All solvents were standard A.C.S. grade or purer. These chemicals were used without any further purification. All water came from a Millipore Milli-Q Academic A-10 water purification system and had a resistivity of 18.2 MΩ

2.4.2 Nanoparticle Synthesis. Au NPs:[19] Citrate coated Au NPs were prepared in a 250 mL round bottom flask (RBF) cleaned with aqua regia (3:1 $HCl:HNO_3$) and fitted with a reflux

condenser. 100 mL of 1 mM $HAuCl_4$ in Milli-Q water was heated to boiling and 10 mL of 38.8 mM sodium citrate (Na_3Cit) was injected quickly with a syringe through the condenser. The flask was allowed to boil for 15 minutes and then cooled to room temperature. The NP solution was then filtered through 0.45 µm Nylon filters. The NP concentration was determined by UV-Vis using $\varepsilon = 2.0 \times 10^8\ M^{-1}\cdot cm^{-1}$.[42] **Ag NPs:**[20] Citrate coated Ag NPs were prepared in a 250 mL round bottom flask (RBF) cleaned with aqua regia (3:1 HCl:HNO_3) and the outside was covered with aluminum foil to block light. 96 mL of Milli-Q water in a sealed flask was deoxygenated by bubbling argon through while stirring for 15 minutes. 790 µL of 38.8 mM Na_3Cit (final 0.3 mM) and 2.0 mL of 5 mM $AgNO_3$ (final 0.1 mM) were added via syringe. The solution was deoxygenated for 15 min and then 1.0 mL of 50 mM $NaBH_4$ (final 0.5 mM) was injected quickly via syringe. The reaction was allowed to stir under argon for 45 minutes. **Pt NPs:**[43] Pt NPs were synthesized using an aged K_2PtCl_4 solution (10 mM in Milli-Q water aged 4 days in a foil covered glass vial). 5 mL of K_2PtCl_4 solution was added to a 250 mL RBF with 95 mL of water (final 0.5 mM). The flask was sealed and Ar was bubbled through while stirring for 10 minutes. 520 µL of 38.8 mM Na_3Cit (final 0.2 mM) was added via syringe and Ar was bubbled through the solution or an additional 10 minutes. H2 gas was bubbled through the solution for 3 minutes, the flask was sealed, and the reaction was stirred for 2 hours. The NPs could be purified by dialysis versus 18.2 MΩ water (4 days, 10,000 MWCO) to improve colloidal stability. **Ru NPs:**[44] To a 50 mL aqua regia cleaned RBF was added 10 mL of 2.26 mM $RuCl_3$. 1 mL of 1 M sodium acetate was added while stirring followed by 1 mL of 112 mM $NaBH_4$ that had been freshly prepared added drop wise over 1 minute. The solution was then sonicated for 20 minutes and then immediately diluted by a factor of 3 to produce a stable solution.

2.4.3 Preparation of Substrates with Cationic Surfaces. Poly-cation thin films were assembled on sections of glass microscope slides after cleaning in piranha solution (3:1 H_2SO_4/30% H_2O_2) at 60 °C in an open dish. *DANGER: Piranha solution is a strong oxidizer and potentially explosive. It must be handled with extreme care and exposure to organic matter must be strictly avoided.* ITO coated slides were prepared by simply rinsing with water, methanol, and acetone. Poly-L-lysine coated slides were prepared by soaking the cleaned slides in a 0.35 mg/mL solution in phosphate buffered saline (PBS = 50 mM $NaHPO_4$, 150 mM NaCl, pH 7.4) overnight, rinsing with Milli-Q water, and then drying in ambient air. PDDA coated slides were prepared by submerging in a 20% solution for 3 hours, rinsing with copious amounts of Milli-Q water, and drying in ambient air. ITO coated glass slides were derivatized with APTMS by first cleaning with sonication in solvents (10 min sonication each with CH2Cl2, Acetone, isopropanol) and then rinsing with methanol. The clean slides were then placed in 3% APTMS/5% water in methanol and shaken for 30 minutes. The slides were then removed from the solution, rinsed in methanol and annealed at 120 °C for 10 minutes.

2.4.4 Surface Bound NP Arrays: The positively charged substrates were then submerged into agitated solutions of the metal NPs. Nanoparticle density gradients were produced by filling glass vials containing the slide at a constant rate using a syringe pump. A holder made from copper wire was used to hold the substrate vertically, away from the side of the vial to assure even exposure to the NP solution.

2.4.5 Reaction of Surface Bound NPs. Two heating methods were employed to cause the surface bound nanoparticle arrays to react. The first method involved heating the arrays in a muffle furnace at temperatures ranging from 300 °C to 600 °C. An inert atmosphere was

maintained by sealing the slide in a stainless steel tube capped with Swagelok® fittings under an argon atmosphere. Alternatively, slides were heated solvents by first placing the slide in a 100 mL RBF equipped with a temperature probe adapter. 20 mL of solvent were added and the flask was sealed with a reflux condenser. A stainless steel needle was used to bubble argon through the solvent for 30 minutes. The flask was then heated to the desired temperature using a J-Kem Scientific Model 210 temperature controller attached to heating mantle. Alternatively for boiling experiments, the flask was heated to boiling using a heating mantle and a variac voltage controller. Argon atmosphere was maintained throughout the experiment and was not broken until the sample had reached room temperature.

2.4.6 Characterization. UV-Visible spectra were collected on an Agilent 8453 spectrometer for gold and silver nanoparticle arrays by suspending the glass slide in the light path of the spectrometer using a holder made from a ruler, a piece of cardboard, and rubber bands. The rubber bands held the slide to the piece of cardboard with a hole slightly smaller than the slide in it and only the top and bottom 1.5 mm were obstructed. The piece of cardboard holding the slide was then attached to a ruler with a binder clip and the position of the spectrum could be measured in this manner. SEM images of nanoparticle arrays on ITO coated glass slides were collected on a JOEL JSM-7401F field emission scanning electron microscope with and energy dispersive X-ray spectrometer. The samples were attached to aluminum SEM stubs using conductive carbon tape. A thin piece of tape was used to make a connection between the surface of the conductive slide and the Al stub. Images were collected using an accelerating voltage of 1.0 kV at a working distance of 3 mm.

2.4.7 Electrochemical Experiments. Electrochemical experiments were conducted using a three electrode configuration. An insulated, tinned copper wire was attached to the ITO coated glass supported nanoparticle array using conductive silver epoxy. Standard gel epoxy was used to insulate the connection from the solution. The array was then connected as the working electrode. An Ag/AgCl electrode was used as the reference, and a Pt wire was used as the auxiliary. The electrolyte contained 6 M methanol, 0.5 M $NaClO_4$, and 100 μM quinine indicator. The electrode potential was scanned in the positive direction, and images were collected using a long wave UV lamp and a digital camera. The surface of the nanoparticles were electro-polished by holding the potential of the working electrode at negative potentials (-250 to -450 mV vs. Ag/AgCl) until the positive fluorescence was observed above the nanoparticles in the positive scan. Positive scans were conducted from 0 mV vs. Ag/AgCl at slow scanning speeds (1 to 10 mV/s) and pictures were taken at various points during the scan. The potential at which the picture was taken was recorded for each picture. Observations of the fluorescence of the quinine indicator were also recorded.

2.5 References

1. Ferrando, R.; Jellinek, J.; Johnston, R. L., Nanoalloys: From theory to applications of alloy clusters and nanoparticles. *Chem. Rev. (Washington, DC, U. S.)* 2008, 108, 845-910.

2. Osterloh, F. E.; Parkinson, B. A., Recent developments in solar water-splitting photocatalysis. *MRS Bulletin* 2011, 36, 17-22.

3. Lewis, N. S.; Nocera, D. G., Powering the planet: Chemical challenges in solar energy utilization. *Proc. Natl. Acad. Sci. U. S. A.* 2006, 103, 15729-15735.

4. Reddington, E.; Sapienza, A.; Gurau, B.; Viswanathan, R.; Sarangapani, S.; Smotkin, E. S.; Mallouk, T. E., Combinatorial electrochemistry: A highly parallel, optical screening method for discovery of better electrocatalysts. *Science* 1998, 280, 1735-1737.

5. Gurau, B.; Viswanathan, R.; Liu, R. X.; Lafrenz, T. J.; Ley, K. L.; Smotkin, E. S.; Reddington, E.; Sapienza, A.; Chan, B. C.; Mallouk, T. E.; Sarangapani, S., Structural and electrochemical characterization of binary, ternary, and quaternary platinum alloy catalysts for methanol electro-oxidation. *J. Phys. Chem. B* 1998, 102, 9997-10003.

6. Woodhouse, M.; Parkinson, B. A., Combinatorial approaches for the identification and optimization of oxide semiconductors for efficient solar photoelectrolysis. *Chem. Soc. Rev.* 2009, 38, 197-210.

7. Woodhouse, M.; Herman, G. S.; Parkinson, B. A., Combinatorial approach to identification of catalysts for the photoelectrolysis of water. *Chem. Mater.* 2005, 17, 4318-4324.

8. Arai, T.; Konishi, Y.; Iwasaki, Y.; Sugihara, H.; Sayama, K., High-throughput screening using porous photoelectrode for the development of visible-light-responsive semiconductors. *J. Comb. Chem.* 2007, 9, 574-581.

9. Schaak, R. E.; Sra, A. K., Rapid low-temperature solution route to multimetallic solid state materials using nanoparticle precursors. *Abstr. Pap. Am. Chem. Soc.* 2004, 228, 563-INOR.

10. Bauer, J. C.; Chen, X.; Liu, Q. S.; Phan, T. H.; Schaak, R. E., Converting nanocrystalline metals into alloys and intermetallic compounds for applications in catalysis. *J. Mater. Chem.* 2008, 18, 275-282.

11. Cable, R. E.; Schaak, R. E., Low-temperature solution synthesis of nanocrystalline binary intermetallic compounds using the polyol process. *Chem. Mater.* 2005, 17, 6835-6841.

12. Schaak, R. E.; Sra, A. K.; Leonard, B. M.; Cable, R. E.; Bauer, J. C.; Han, Y. F.; Means, J.; Teizer, W.; Vasquez, Y.; Funck, E. S., Metallurgy in a beaker: Nanoparticle toolkit for the rapid low-temperature solution synthesis of functional multimetallic solid-state materials. *J. Am. Chem. Soc.* 2005, 127, 3506-3515.

13. Schaak, R. E.; Sra, A. K., Controlling atomic order in intermetallic nanocrystals. *Abstr. Pap. Am. Chem. Soc.* 2004, 228, 763-INOR.

14. Schaak, R. E.; Sra, A. K., Synthesis of atomically ordered nanocrystals from bimetallic nanoparticle precursors. *Abstr. Pap. Am. Chem. Soc.* 2004, 227, 847-INOR.

15. Schaak, R. E.; Cable, R. E.; Leonard, B. M.; Norris, B. C., Colloidal crystal microarrays and two-dimensional superstructures: A versatile approach for patterned surface assembly. *Langmuir* 2004, 20, 7293-7297.

16. Leger, J. M., Mechanistic aspects of methanol oxidation on platinum-based electrocatalysts. *J. Appl. Electrochem.* 2001, 31, 767-771.

17. Pang, H. L.; Zhang, X. H.; Zhong, X. X.; Liu, B.; Wei, X. G.; Kuang, Y. F.; Chen, J. H., Preparation of Ru-doped SnO2-supported Pt catalysts and their electrocatalytic properties for methanol oxidation. *J. Colloid Interface Sci.* 2008, 319, 193-198.

18. Shimazaki, Y.; Kobayashi, Y.; Yamada, S.; Miwa, T.; Konno, M., Preparation and characterization of aqueous colloids of Pt-Ru nanoparticles. *J. Colloid Interface Sci.* 2005, 292, 122-126.

19. Storhoff, J. J.; Elghanian, R.; Mucic, R. C.; Mirkin, C. A.; Letsinger, R. L., One-Pot Colorimetric Differentiation of Polynucleotides with Single Base Imperfections Using Gold Nanoparticle Probes. *J. Am. Chem. Soc.* 1998, 120, 1959-1964.

20. Sun, Y. G.; Xia, Y. N., Gold and silver nanoparticles: A class of chromophores with colors tunable in the range from 400 to 750 nm. *Analyst* 2003, 128, 686-691.

21. Kramer, S.; Xie, H.; Gaff, J.; Williamson, J. R.; Tkachenko, A. G.; Nouri, N.; Feldheim, D. A.; Feldheim, D. L., Preparation of protein gradients through the controlled deposition of protein-nanoparticle conjugates onto functionalized surfaces. *J. Am. Chem. Soc.* 2004, 126, 5388-5395.

22. Mulvaney, P., Surface plasmon spectroscopy of nanosized metal particles. *Langmuir* 1996, 12, 788-800.

23. Link, S.; El-Sayed, M. A., Spectral properties and relaxation dynamics of surface plasmon electronic oscillations in gold and silver nanodots and nanorods. *J. Phys. Chem. B* 1999, 103, 8410-8426.

24. Sandrock, M. L.; Foss, C. A., Synthesis and linear optical properties of nanoscopic gold particle pair structures. *J. Phys. Chem. B* 1999, 103, 11398-11406.

25. Khlebtsov, B. N.; Khanadeyev, V. A.; Ye, J.; Mackowski, D. W.; Borghs, G.; Khlebtsov, N. G., Coupled plasmon resonances in monolayers of metal nanoparticles and nanoshells. *Physical Review B* 2008, 77.

26. Cai, W. P.; Zhong, H. C.; Zhang, L. D., Optical measurements of oxidation behavior of silver nanometer particle within pores of silica host. *J. Appl. Phys.* 1998, 83, 1705-1710.

27. Link, S.; Wang, Z. L.; El-Sayed, M. A., Alloy formation of gold-silver nanoparticles and the dependence of the plasmon absorption on their composition. *J. Phys. Chem. B* 1999, 103, 3529-3533.

28. Okkerse, B., SELF-DIFFUSION OF GOLD. *Physical Review* 1956, 103, 1246-1249.

29. Yasuda, H.; Mori, H., SPONTANEOUS ALLOYING OF ZINC ATOMS INTO GOLD CLUSTERS AND FORMATION OF COMPOUND CLUSTERS. *Phys. Rev. Lett.* 1992, 69, 3747-3750.

30. Lee, K.; Tienes, B. M.; Wilker, M. B.; Schnitzenbaumer, K. J.; Dukovic, G., (Ga1–xZnx)(N1–xOx) Nanocrystals: Visible Absorbers with Tunable Composition and Absorption Spectra. *Nano Lett.* 2012, 12, 3268-3272.

31. Vasquez, Y.; Henkes, A. E.; Bauer, J. C.; Schaak, R. E., Nanocrystal conversion chemistry: A unified and materials-general strategy for the template-based synthesis of nanocrystalline solids. *J. Solid State Chem.* 2008, 181, 1509-1523.

32. Wadia, C.; Alivisatos, A. P.; Kammen, D. M., Materials Availability Expands the Opportunity for Large-Scale Photovoltaics Deployment. *Environ. Sci. Technol.* 2009, 43, 2072-2077.

33. Liu, H. S.; Song, C. J.; Zhang, L.; Zhang, J. J.; Wang, H. J.; Wilkinson, D. P., A review of anode catalysis in the direct methanol fuel cell. *J. Power Sources* 2006, 155, 95-110.

34. Antolini, E.; Lopes, T.; Gonzalez, E. R., An overview of platinum-based catalysts as methanol-resistant oxygen reduction materials for direct methanol fuel cells. *J. Alloys Compd.* 2008, 461, 253-262.

35. Tang, Y.; Cheng, W. L., Metallic Nanoparticles as Advanced Electrocatalysts. *Science of Advanced Materials* 2012, 4, 784-797.

36. Wang, H. S.; Abruna, H. D., Electrocatalysis of Direct Alcohol Fuel Cells: Quantitative DEMS Studies. In *Fuel Cells and Hydrogen Storage*, Bocarsly, A.; Mingos, D. M. P., Eds. 2011; Vol. 141, pp 33-83.

37. Zhong, C. J.; Luo, J.; Fang, B.; Wanjala, B. N.; Njoki, P. N.; Loukrakpam, R.; Yin, J., Nanostructured catalysts in fuel cells. *Nanotechnology* 2010, 21.

38. Zhou, Y. K.; Neyerlin, K.; Olson, T. S.; Pylypenko, S.; Bult, J.; Dinh, H. N.; Gennett, T.; Shao, Z. P.; O'Hayre, R., Enhancement of Pt and Pt-alloy fuel cell catalyst activity and durability via nitrogen-modified carbon supports. *Energy & Environmental Science* 2010, 3, 1437-1446.

39. Peng, Z. M.; Yang, H., Designer platinum nanoparticles: Control of shape, composition in alloy, nanostructure and electrocatalytic property. *Nano Today* 2009, 4, 143-164.

40. May, E. L.; Hillier, A. C., Rapid and reversible generation of a microscale pH gradient using surface electric fields. *Anal. Chem.* 2005, 77, 6487-6493.

41. Jayaraman, S.; Hillier, A. C., Electrochemical synthesis and reactivity screening of a ternary composition gradient for combinatorial discovery of fuel cell catalysts. *Meas. Sci. Technol.* 2005, 16, 5-13.

42. Maye, M. M.; Han, L.; Kariuki, N. N.; Ly, N. K.; Chan, W. B.; Luo, J.; Zhong, C. J., Gold and alloy nanoparticles in solution and thin film assembly: spectrophotometric determination of molar absorptivity. *Anal. Chim. Acta* 2003, 496, 17-27.

43. Wilson, O. M.; Hu, X. Y.; Cahill, D. G.; Braun, P. V., Colloidal metal particles as probes of nanoscale thermal transport in fluids. *Physical Review B* 2002, 66.

44. Yang, J.; Deivaraj, T. C.; Too, H. P.; Lee, J. Y., Acetate stabilization of metal nanoparticles and its role in the preparation of metal nanoparticles in ethylene glycol. *Langmuir* 2004, 20, 4241-4245.

Chapter 3. Layered Phosphonates in Colloidal Synthesis of Anisotropic ZnO Nanocrystals*

3.1 Introduction

Alkyl phosphonic acids (PAs) have played a crucial role in the development of synthetic methods for colloidal semiconductor nanocrystals, most notably CdSe-based materials. Their use has enabled control over nanocrystal size and shape through fine tuning of experimental parameters.[1-6] When used in CdSe nanocrystal synthesis, aliphatic PAs react with Cd sources such as CdO and $Cd(CH_3)_2$ to form cadmium phosphonates.[4, 7] These precursor molecules react with Se sources, such as trialkylphosphine selenides, to nucleate and grow the nanocrystals.[8, 9] It has been proposed that the strong binding of phosphonate ligands to Cd^{2+} results in relatively sTable 3.Cd precursors, allowing for the accumulation of high monomer concentrations, which promotes anisotropic nanocrystal growth.[3, 4] In addition to controlling the reaction kinetics and the resulting nanocrystal shapes, PAs serve as strong surface-capping ligands that stabilize nanocrystals against aggregation and precipitation in organic solvents.[10, 11]

ZnO is another II-VI wurtzite semiconductor of fundamental and technological importance due to its large exciton binding energy (60 meV).[12, 13] There is considerable interest in control over the anisotropic growth of colloidal ZnO nanocrystals for applications as transducers or field-effect transistors, and use in gas sensors or lasers.[13] While several high-temperature colloidal synthetic procedures with control of particle size and shape have been reported,[14-20] relatively few utilize PAs.[12, 21-23] For example, tert-butylphosphonic acid (TBPA)

*This chapter is adapted from and expands upon the following article: Tienes, Bryan M.; Perkins, Russell; Shoemaker, Richard; Dukovic, Gordana. Layered Phosphonates in Colloidal Synthesis of Anisotropic ZnO Nanocrystals. *Chem. Mater.* 2013, *Accepted*.

enabled the synthesis of quantum confined ZnO nanocrystals in the thermal decomposition of zinc acetate ($Zn(OAc)_2$), while in the absence of PA bulk ZnO was obtained.[21] In another synthesis of ZnO nanocrystals by reaction of zinc stearate with 1-octadecanol, the addition of octadecylphosphonic acid (ODPA) post ZnO nanocrystal formation resulted in the sharpening of size distribution of quantum dots.[22] In that synthesis ODPA was also able to convert of nano-pyramids into quantum dots.[22] Finally, addition of tetradecylphosphonic acid (TDPA) in the synthetic mixture of $Zn(OAc)_2$ and 1,12-dodecanediol, resulted in a drastic change of the product morphology. In the absences of PA, hierarchically ordered spheres consisting of aggregated ZnO nanocones formed, and the presence of TDPA changed the morphology to highly soluble nanorods with a relatively uniform size distribution.[12, 23] These reports suggest that PAs may provide the degree of synthetic control currently available with CdSe nanocrystals.

This chapter discusses the role of aliphatic PAs in the synthesis of anisotropic ZnO nanocrystals. The initial step of the reaction involves the formation of an insoluble nano-structured intermediate from the reaction of $Zn(OAc)_2$ with aliphatic PAs (e.g., octadecylphosphonic acid, ODPA). Characterization of the intermediate by TEM, STEM-EELS, low-angle XRD, FTIR, and solid-state ^{31}P NMR revealed that $Zn(OAc)_2$ reacts with PAs to form layered Zn-phosphonates. Such materials are known in the literature, but have not been described in the context of nanocrystal synthesis. It was discovered that these periodic structures react with 1-undecanol to produce ZnO nanocrystals, however, both the $Zn(OAc)_2$ and Zn-phosphonate precursors are required to obtain anisotropic rod-shaped nanocrystals. The dimensions of the anisotropic ZnO nanocrystals are relatively insensitive to the length of

the aliphatic chain of the PA in the C6-C18 length range. The presence of two Zn precursor sources in the reaction mixture ($Zn(OAc)_2$ and Zn-phosphonate) presents a contrast to the single molecular phosphonate source described in the formation of CdSe nanocrystals. These sources provide several chemical pathways to ZnO and appear to work synergistically in the formation of anisotropic ZnO nanocrystal shapes.

3.2 Results and Discussion

A previously reported procedure was adapted to explore the role of PAs in a ZnO nanorod synthesis. In that procedure, the addition of a long-chain aliphatic PA to the reaction mixture drastically transformed the product from ZnO nanocone aggregates to highly soluble ZnO nanorods.[12] Briefly, the air-free synthetic procedure reported here consisted of the following steps: (1) drying of $Zn(OAc)_2$ (1.0 mmol) dissolved in a mixture of octyl ether and trioctylphosphine oxide (TOPO). This step was carried out by heating under vacuum at 100 °C for 30 minutes; (2) precursor formation step, in which the reaction mixture was heated to 200 °C under an argon atmosphere, incubated at that temperature for 60 minutes, and cooled to 60 °C; and (3) nanocrystal formation step, in which 1-undecanol (6 mmol) was added, and the reaction heated to 250 °C and allowed to proceed for 2 hours. A TEM image of the ZnO nanocrystals resulting from the synthesis described above is shown in Figure 3.1A. The particles are aggregated, relatively large

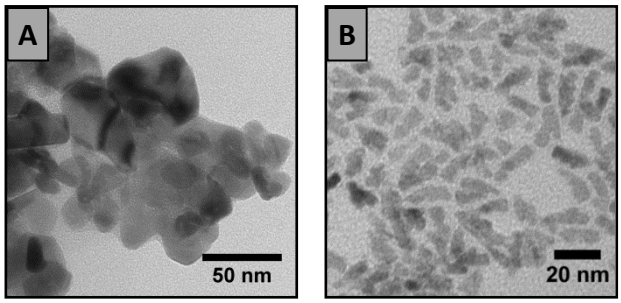

Figure 3.1. (A) TEM image of ZnO nanocrystals synthesized from a reaction of $Zn(OAc)_2$ with 1-undecanol in a solvent of octyl ether and TOPO. The crystals are aggregated, relatively large, and poly-disperse. (B) TEM image of ZnO nano-crystals synthesized by reaction of $Zn(OAc)_2$ and ODPA with 1-undecanol. The particles are highly anisotropic with rod-like shapes.

(smallest dimension > 10 nm), and polydisperse in size and shape. This synthetic procedure is referred to as the *PA-free* synthesis. In contrast, when ODPA was included in the as a starting material in a 0.45:1 ODPA:Zn molar ratio, the resulting ZnO nanocrystals were anisotropic irregularly-shaped nanorods, with diameters of 7 ± 2 nm, lengths of 18 ± 5 nm, and the average aspect ratio of 2.5:1 (Figure 3.1B). The procedure that includes ODPA is referred to as the *ZnO nanorod* synthesis. The effect of the PA in the synthesis was first explored by identification and characterization of the insoluble intermediate and then the role of the intermediate in the synthesis of anisotropic ZnO was explored.

3.2.1 Isolation of a layered intermediate. The reaction mixtures of the *PA-free* and *ZnO nanorod* syntheses exhibit different appearances at various stages of the reaction. In the *PA-free* synthesis, the mixture of $Zn(OAc)_2$, octyl ether, and TOPO turned optically clear at 90 °C during the drying step, indicating dissolution of the starting materials. The solution remained clear during the precursor formation step and only upon the addition of 1-undecanol did the reaction turn cloudy, as the insoluble ZnO nanocrystals (Figure 3.1A) were formed. In the *ZnO nanorod* synthesis, the ODPA-containing reaction mixture also turned clear upon reaching approximately 90 °C. However, the mixture quickly became cloudy before reaching 100 °C and at the same time the pressure increased in the Schlenk line, which indicated the release of a volatile product. The cloudiness persisted throughout the remainder of the reaction (both the precursor formation and nanocrystal formation steps), suggesting the existence of an insoluble intermediate. The ZnO nanocrystals could be isolated/purified and are shown in the TEM image, Figure 3.1B. To investigate the structure and the chemical identity of the insoluble

intermediate, the *ZnO nanorod* synthesis was halted before the addition of 1-undecanol. The solid was isolated by precipitation and purified (see Experimental section).

Figure 3.2A shows an SEM image of the insoluble intermediate formed during *ZnO nanorod* synthesis. The material consisted of quasi-cylindrical 3-dimensional structures with average diameters of approximately 100 nm and lengths on the order of 1 μm. A closer look via TEM (Figure 3.2B) revealed that each quasi-cylinder consisted of alternating layers of dark and light contrast materials. HR-TEM (Figure 3.2C) showed the dark-contrast layers to be significantly thinner than the light-contrast layers and there was no evidence of appreciable crystalline domains in the HR-TEM images. Information about the elemental composition of the alternating layers was provided by electron energy loss spectroscopy (EELS) mapping via scanning TEM (STEM) (Figure 3.2D). In the high angle annular dark field (HAADF) image (Figure 3.2D, top), the contrast is reversed such that the bright regions in HAADF correspond to the dark regions in Figures 2B and 2C. EELS maps reveal that he bright regions in the

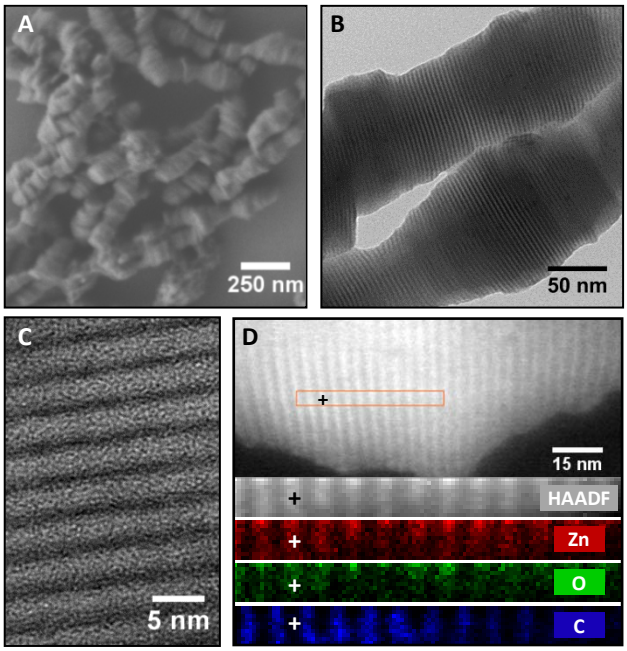

Figure 3.2. Images of the insoluble intermediate after the precursor formation step in the *ZnO nanorod* synthesis. (A) An SEM image illus-trating that the intermediate consists of 3-dimensional quasi-cylindrical structures with diameters around 100 nm and lengths on the order of 1 μm; (B) TEM image demonstrating the periodic structure within the quasi-cylinders. (C) HR-TEM image showing thin layers of dark contrast material and thicker layers of a light contrast material. (D) STEM-HAADF image of the periodic layered structure correlated with STEM-EELS images for Zn, O, and C, showing that the layers consist of carbon-rich regions alternating with zinc- and oxygen-rich regions.

HAADF image are rich in Zn and O, while the dark HAADF regions contain high amounts of C. The images shown in Figure 3.2 suggest that the solid formed in *ZnO nanorod* synthesis consists of periodic structures that are inorganic-organic hybrids with relatively thin Zn and O-containing layers and relatively thick organic layers.

In order to characterize the periodic structure of the layered intermediate in *ZnO nanorod* synthesis, low angle powder x-ray diffraction (XRD) was employed. The features that correspond to intermolecular periodicity can be determined by examining diffraction in the 2Θ range of 2-20°.[24] The solid intermediate shown in Figure 3.2 exhibits several regularly spaced peaks at angles below 15° 2Θ (Figure 3.3G, green trace). The series of evenly spaced peaks is

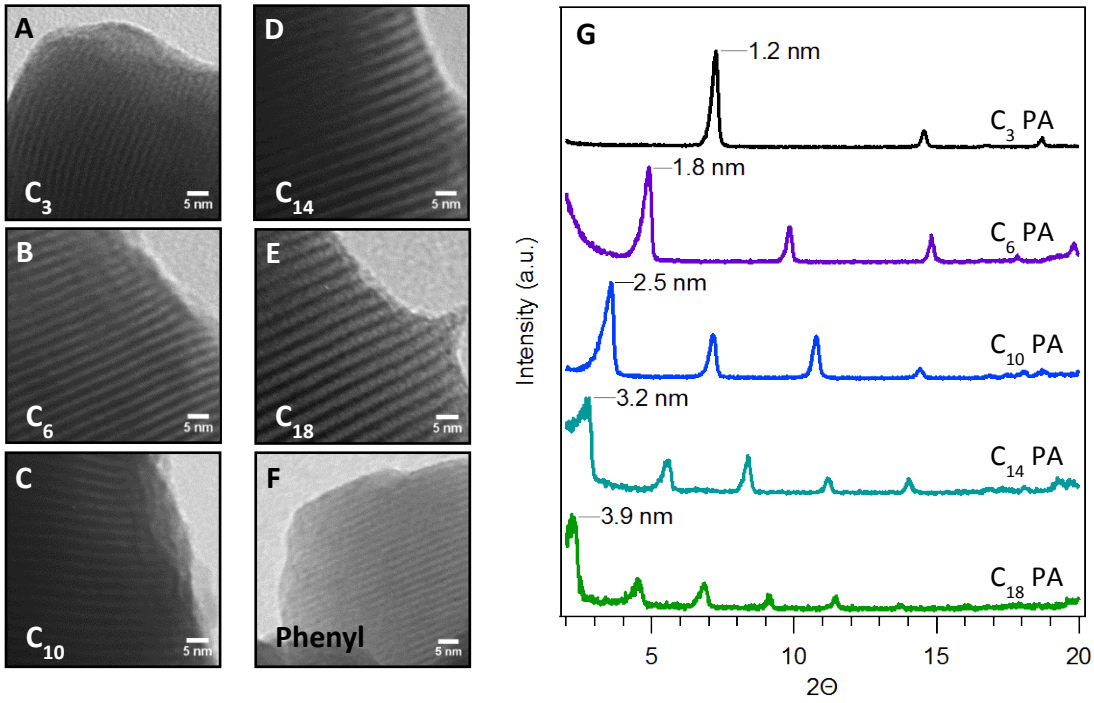

Figure 3.3. TEM images of the layered phosphonate that was isolated as the intermediate in ZnO nanocrystal synthesis using: (A)Propyl (C3) phosphonic acid, (B) Hexyl (C6) phosphonic acid, (C) Decyl (C10) phosphonic acid, (D) Tetradecyl (C14) phosphonic acid, (E) Octadecyl (C18) phosphonic acid, and (F) Phenyl phosphonic acid. (G) Low angle XRD patterns of Zn-(C3, C6, C10, C14, C18) phosphonates prepared by reaction of $Zn(OAc)_2$ with C3, C6, C10, C14, C18 PAs. The position of the (001) reflection was converted to d-spacing using the Bragg equation.

assigned to multiple orders of diffraction (e.g., (001), (002), (003), etc.) corresponding to the repeat unit length (i.e., d-spacing) in the direction along the length of the quasi-cylinders shown in Figure 3.2. The well-defined peak positions indicate that the d-spacing is uniform throughout the sample. The repeat unit length, calculated using Bragg's law, is 3.9 nm, which is consistent with the TEM observations (Figure 3.2).

To determine whether the length of the repeat unit depends on the alkyl chain length of the PA, ODPA (C18) was replaced with propyl (C3), hexyl (C6), decyl (C10), and tetradecyl(C14) PAs in the reaction with $Zn(OAc)_2$. All these reactions resulted in the formation of periodic structures (Figure 3.3A-F). Low-angle XRD patterns for the layered structures formed using C3, C6, C10, C14, and C18 PAs (Figure 3.3G) demonstrate an increase in d-spacing with increasing alkyl chain length. The d-spacing as a function of PA length, as measured from an O atom of the OH group to the terminal H on the alkyl chain, is shown in Figure 3.4. The relationship is linear, with a remarkably good fit (R^2 = 0.999) and a slope of 1.5 [d (nm) / PA length(nm)], which will be discussed in a later section. This linear dependence strongly suggests that the organic layers originate from the PAs. Extrapolating to zero PA length, we find the thickness of the Zn-containing layer to be 0.35 nm. This length is on the order of the lattice parameter *a* of wurtzite ZnO,[13] suggesting that the Zn-containing layers are a single Zn atom thick.

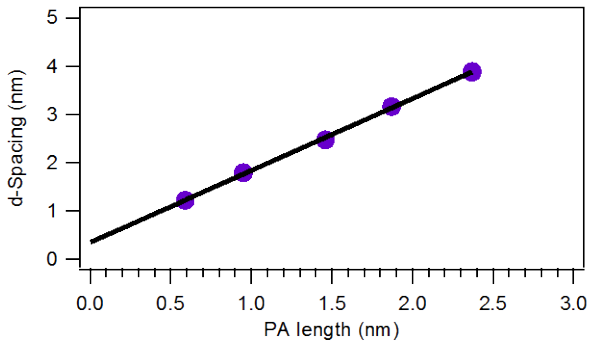

Figure 3.4. d-spacing observed by XRD as a function of the PA length. The linear fit is extrapolated to zero (infinitely small PA) to give a Zn layer thickness of 0.35 nm. The slope of the line is 1.5.

3.2.2 Chemical identification and structure of the layered intermediate. Based

on the periodic layered structure, STEM-EELS elemental analysis, and the thinness of the Zn-containing layer, the solid intermediates formed by reaction of $Zn(OAc)_2$ and PAs were hypothesized to be layered Zn phosphonates. Layered divalent metal phosphonates are a well-known class of materials.[25-32] Interest in these materials stems from their porous structure and their potential applications as ion exchangers, sorbents, proton conductors, catalysts, and catalyst supports.[27, 28, 33] Zn phosphonates are typically made through aqueous routes by reacting a zinc salt (usually $ZnCl_2$) with the PA and excess base.[26, 30, 31, 34-36] The base deprotonates the PA, which allows it to dissolve and form a complex with Zn^{2+}. The Zn phosphonate precipitates from solution and is isolated by filtration. Non-aqueous routes to Zn phosphonates, such as the one described here, are not common,[37] and such structures have not been previously reported in the context of nanocrystal synthesis. Previous reports characterizing layered metal phosphonates by FT-IR[30, 32, 35-38] and ^{31}P solid-state NMR[29, 31, 38] provide a means for comparing the structures generated in the *ZnO nanorod* synthesis with previously described materials.

An FTIR spectrum of the layered intermediate in the *ZnO nanorod* synthesis is shown in Figure 3.5A. The peaks at 2800-3000 cm^{-1} correspond to the C-H stretching modes of the alkyl chains and the peak at 1463 cm^{-1} corresponds to alkyl chain C-H scissor mode.[24, 39, 40] The region between 1250 cm^{-1} and 900 cm^{-1} is associated with the phosphonate functional group and the peaks correspond to P=O, P-O, and P-O-H stretches.[37, 39, 41, 42] Similar FTIR spectra were obtained when TOPO was not included in the solvent, which indicates that TOPO is not likely to be incorporated into the structure. For comparison, a FTIR spectrum of Zn-octadecyl phosphonate (Zn-ODP) synthesized using the previously reported aqueous methods[26-28] is

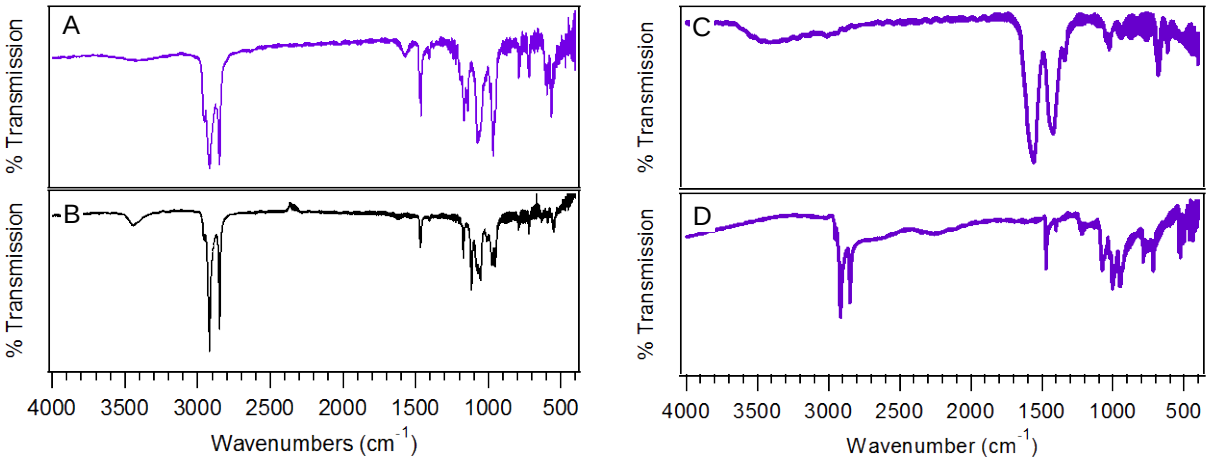

Figure 3.5. FTIR spectra of samples dried on a KBr crystal. (A) Insoluble intermediate in the non-aqueous *ZnO nanorod* synthesis. (B) Zn-ODP prepared by an aqueous method from $ZnCl_2$, ODPA, and NaOH. (C) $Zn(OAc)_2$ starting material in the ZnO reaction. The spectrum contains strong C=O stretches at 1554 cm^{-1} and 1417 cm^{-1}. (D) ODPA starting material in the ZnO reaction. The spectrum contains C-H stretches between 3000 and 2800 cm^{-1}; a broad O-H stretch between 2000 and 3000 cm^{-1}; a C-H scissor mode peak at 1471 cm^{-1}; and P-O peaks between 1250 and 900 cm^{-1}.

shown in Figure 3.5B. This spectrum is nearly identical to the one in Figure 3.5A with two exceptions. A peak in the OH region (3440 cm^{-1}) is present in Figure 3.5B and is characteristic of a hydrated product.[35, 37] The P-O peaks, centered at 1150 cm^{-1}, have a larger splitting in Figure 3.5B, which we attribute to the presence of water molecules incorporated into the crystal lattice of the hydrated product. Very similar differences were previously observed between the FTIR spectra of hydrated and dehydrated Zn-phenyl phosphonates.[35] The FTIR spectra of the pure starting materials ($Zn(OAc)_2$ and ODPA) are also shown in Figure 3.5C&D for comparison. To provide further evidence that the small differences in the spectra are due to presence of water in the aqueous product, Zn-phenyl phosphonate was synthesized both by the method reported here and by the previously reported aqueous method.[35] The comparison of their FTIR spectra (Figure 3.6) matches the previously reported comparison of hydrated and dehydrated

Zn-phenyl- phosphonates.[35] The FTIR data support the hypothesis that the product of reaction of $Zn(OAc)_2$ with ODPA in the synthesis of ZnO nanorods is layered Zn-ODP. This compound can form by the displacement of acetate with phosphonate, with acetic acid as a product:

Equation 1

$$n\ Zn(OAc)_2 + n\ ODPA \rightarrow [Zn(ODP)]_n + 2n\ HOAc$$

This reaction is consistent with the observation of a volatilized product during the drying step at 100 °C under vacuum.

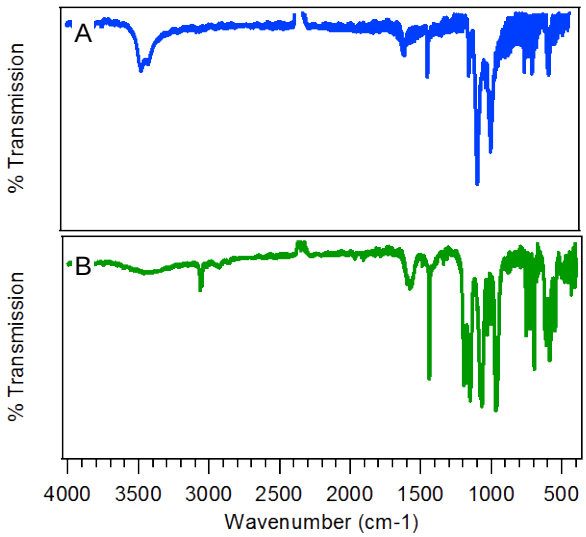

Figure 3.6. (A) FTIR of zinc phenylphosphonate made using an aqueous preparation (see Methods). (B) FTIR of the zinc phenylphosphonate made in the precursor formation step of *ZnO nanorod* synthesis using phenyl PA instead of ODPA. These spectra match previously reported spectra. (see Text)

Layered Zn phosphonates can have varying bonding motifs between the zinc atoms and the oxygen atoms of the phosphonate. The possibilities are described as (011), (111), (112), and (122).[29, 31, 38] In this notation, each of the three numbers represents an oxygen atom in the phosphonate and the value of the number corresponds to the number of metal ions bound to that oxygen. A value of 2 indicates that the oxygen atom is bridging two metal ions. The different bonding arrangements can be distinguished by ^{31}P solid state magic angle spinning (MAS) NMR by determining the associated chemical shift tensor parameters.[29, 31] These parameters have been determined for several bonding motifs in Zn phosphonates synthesized by aqueous methods. The NMR data was correlated with the chemical structure determined by single crystal x-ray crystallography.[29] Here, ^{31}P solid state NMR was utilized to determine the bonding arrangement in layered Zn-ODP formed during the *ZnO nanorod* synthesis. Figure 3.7

shows isotropic ^{31}P solid state NMR spectra of ODPA (red trace) and the insoluble intermediate in the ZnO nanorod synthesis (black trace), obtained using magic angle spinning (MAS) at 10 kHz. ODPA exhibits one peak at 30 ppm, and in the Zn-ODP spectrum, 4 separate, isotropic chemical shifts are observed. Peaks corresponding to TOPO (Figure 3.7, green trace) were not observed in the spectra of the product. The presence of 4 well resolved, isotropic chemical shifts observed in Zn-ODP spectrum indicates that the unit cell of the crystalline material contains 4 crystallographically distinct phosphorous centers. Chemical shift tensor parameters of the four Zn-ODP peaks in the 27-34 ppm region, determined by spinning the sample slowly (2.0 to 2.2 kHz) and simulating the powder spectra of each the four isotropic peaks (see Methods section), are shown in Table 3.1. The 2 kHz MAS spectra, their deconvolution, and the simulated powder spectra are shown in Figures 3.8 and 3.9. The values of the asymmetry parameter (η) and the chemical shift anisotropy (Δ) are a close match to those previously reported for the (112) bonding motif for each of the 4 phosphorous centers observed in Zn-ODP.[29, 38] In the (112) structure, one of the phosphonate O atoms bridges two Zn atoms, while the remaining two O atoms are singly bound to one Zn atom each (Figure 3.10). Each Zn is tetrahedrally coordinated

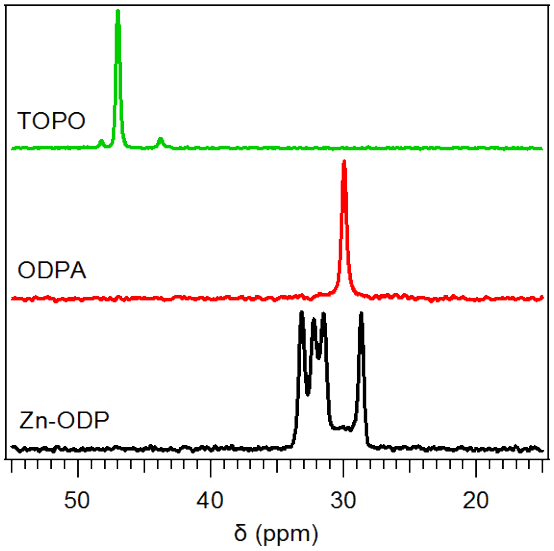

Figure 3.7. ^{31}P MAS (10 kHz) solid state NMR spectra of TOPO, ODPA, and layered Zn-ODP. The TOPO and ODPA spectra each contain a single peak, while the layered Zn-ODP spectrum contains four peaks with chemical shifts similar to those of ODPA.

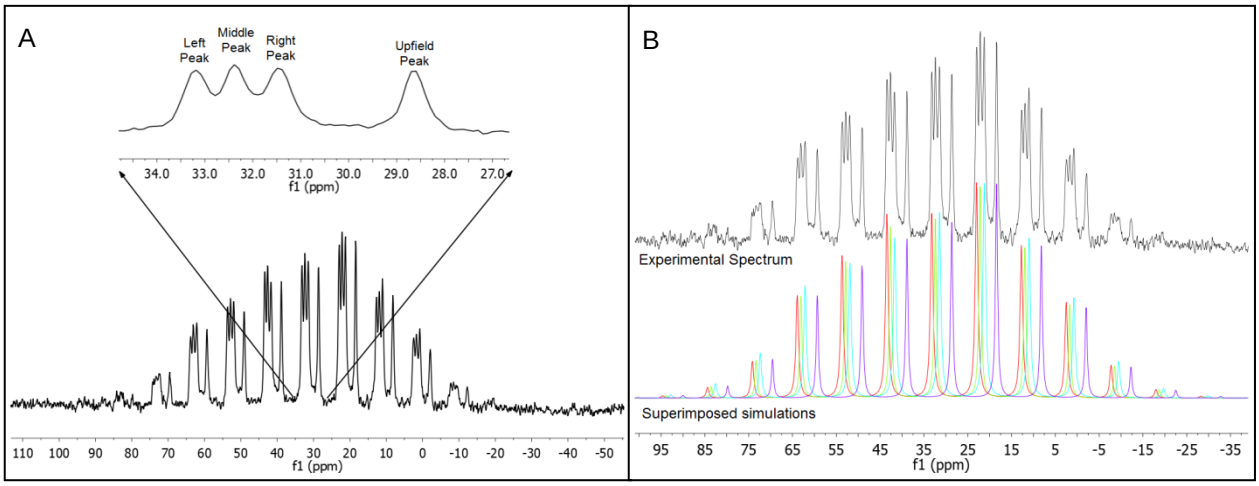

Figure 3.8. (A) ^{31}P MAS NMR collected at 2kHz to be used determine the tensor parameter for each of the four peaks shown. The isotropic peaks are expanded and labeled for clarity. (B top) The experimental MAS (2 kHz) ^{31}P NMR spectra of the Zn-ODP. (B bottom) Overlaid simulated spectra generated using the STARS simulation package in the VNMRJ 3.2A software (Agilent Technologies). The spectrum of each of the four peaks were simulated independently of each other allowing the software to calculate a asymmetry parameter (η) and the chemical shift anisotropy (Δ) for each peak.

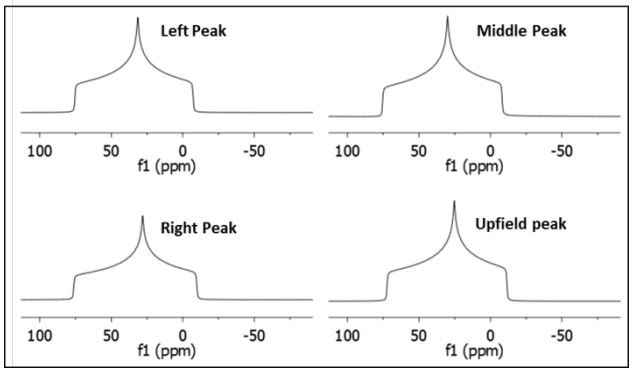

Figure 3.9. The simulated static solid ^{31}P NMR spectra for each of the four peaks generated using the Agilent Technologies STARS software utility.

Table 3.1. Chemical shift tensor parameters for ODPA and the Zn-ODP intermediate

Sample	δ_{iso} [a]	δ_{zz}	δ_{yy}	δ_{xx}	η [b]	Δ [c]
ODPA	30.0	-16.45	45.82	60.53	0.28	-46.42
Zn-ODP	28.7	72.35	25.24	-11.66	0.84	43.70
	31.5	76.16	28.06	-9.83	0.85	44.70
	32.3	75.45	29.98	-8.28	0.89	43.06
	33.1	75.49	31.44	-7.31	0.92	42.28

a. $\delta_{iso} = (\delta_{xx} + \delta_{yy} + \delta_{zz})/3$ (isotropic chemical shift; all values are relative to 85% H_3PO_4)
b. $\eta = (\delta_{yy} - \delta_{xx})/ \Delta$ (asymmetry parameter)
c. $\Delta = \delta_{zz} - \delta_{iso}$ (chemical shift anisotropy)

by O atoms such that sites are not available for coordination of additional species in the material. The (112) configuration has been previously reported for Zn-ODP.[31]

The packing geometry of the alkyl chains associated with the PAs was determined using the information in Figure 3.4. The slope of the line correlating the length of the periodic repeat

unit (i.e., the d-spacing) with the PA length is 1.5. A slope of 1 would indicate completely interdigitated aliphatic chains, while a value of 2 would suggest aliphatic chains that are stacked in fully extended configurations perpendicular to the Zn planes. The slope of 1.5 suggests that the aliphatic layers are oriented at an angle τ from the plane of the Zn atoms such that their projection along the axis perpendicular to the planes is 1.5 times the length of one chain (Figure 3.11). The parallel and herringbone configurations of aliphatic chains (Pattern 1 and Pattern 2 in Figure 3.11) cannot be distinguished in this model. The value of τ determined from the slope was calculated using Equation 2 is 49°.

Equation 2

$$\cos(90° - \tau) = \frac{\text{slope}}{2}$$

τ =49° has been predicted to be the ideal value for alkyl phosphonates of divalent metals based on the local bonding geometry at the phosphonate-metal interface.[26-28]

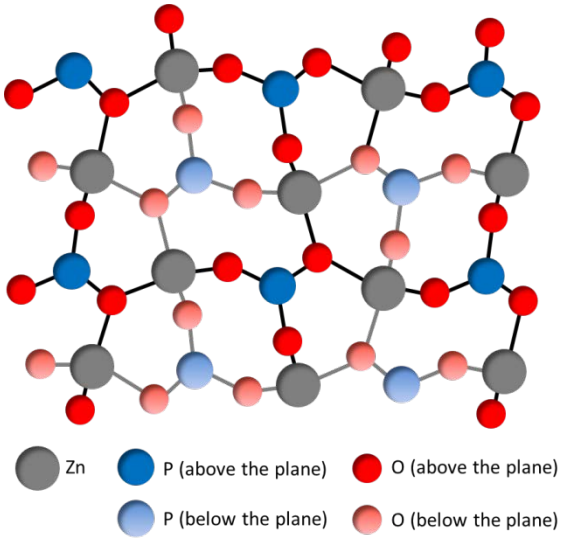

Figure 3.10. A schematic of the atomic arrangement in (112) Zn-ODP as determined by comparison of the ^{31}P tensor parameters with literature values. The alkyl chains point in and out of the plane of the page and have been removed for clarity.

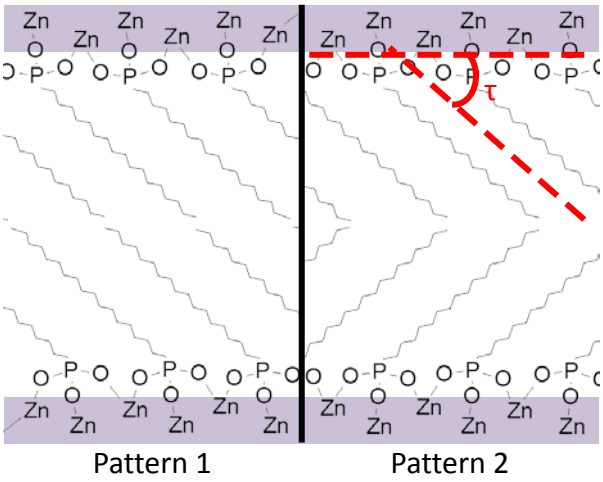

Figure 3.11. A schematic of the proposed packing of the alkyl chains in the layered Zn-ODP structure.

3.2.3 Reaction to form nanocrystals. Following the precursor formation step where the Zn-ODP described above was made, 1-undecanol was added in excess and the reaction was heated for 2 hours at 250 °C. The resulting ZnO nanorods (Figure 3.1B) could be separated from the residual Zn-ODP due to a difference in solubility in hexanes. After precipitating all solids from the *ZnO nanorod* synthesis mixture using alcohol, the precipitate was dispersed in hexanes. Using centrifugation, the highly soluble ZnO nanorods were retained in the supernatant and could be separated from the rest of the precipitate to be studied further. It should be noted that this procedure was not 100% efficient and some nanorods remained in the precipitate precluding the quantitative calculation of a synthetic yield. Characterization of the ZnO nanorods was done by UV-Vis and powder XRD (Figure 3.12). The ability to make stable, optically clear solutions of the ZnO nanorods allowed the UV-Visible spectrum in Figure 3.12A to be collected. It contains a sharp band edge absorption at 380 nm typical for a direct band gap semiconductor.[21] Drying solutions of the ZnO nanorod solutions onto XRD substrates allowed the collection of a powder XRD pattern. It matches well with the reference pattern for wurtzite ZnO (Figure 3.12B). The characterization data confirmed that the ZnO

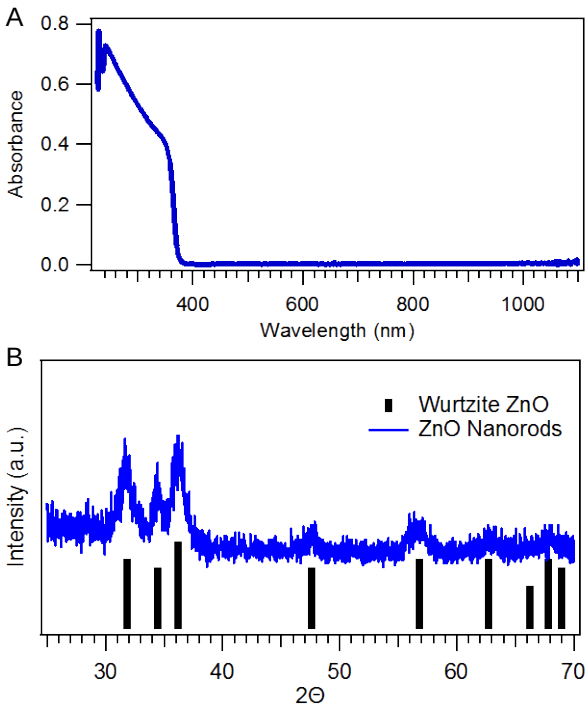

Figure 3.12. Characterization data for the puri-fied product from the *ZnO nanorod* synthesis. (A) A UV-Visible spectrum showing strong band edge absorption at 380 nm. (B) XRD pattern matching the standard pattern for wurtzite ZnO.

nanorods produced by this synthesis were wurtzite phase ZnO. This is consistent to what has been observed previously for ZnO nanorods prepared from $Zn(OAc)_2$ and an alkyl phosphonic acid in the same solvent.[12]

3.2.4 The role of TOPO. The triocylphosphine oxide (TOPO) co-solvent was included in this study in order to remain consistent with the synthesis previously reported in the literature.[12] Therefore, experiments were conducted to ascertain the role of TOPO and it was found to affect two aspects of the reaction. The first aspect was that TOPO affected the shape of the Zn-ODP intermediate isolated after the precursor formation step of the *ZnO nanorod* synthesis. Without TOPO, the phosphonate was in irregular shapes and very polydisperse in size (Figure 3.13A). Also, the layers in these structures were often seen running parallel to the axis of large Zn-ODP sheets. When TOPO was included in the solvent, the Zn-ODP formed into the long quasi-cylinders described above with the layers running perpendicular to the long axis of the cylinder (Figure 3.13B). As described earlier, it was determined by FTIR and NMR that TOPO was not incorporated into the layered intermediate, but based on this data, TOPO appears to help to shape the secondary structure of the Zn-ODP. Upon continuing the reaction after the precursor formation step both with and without TOPO present, the product ZnO nanorods were also analyzed. The nanorods are very similar in appearance (Figure 3.14), which suggests that TOPO does not play a significant role in the morphology of the product. However, an analysis of the amount of nanorods recovered using UV-Vis discovered

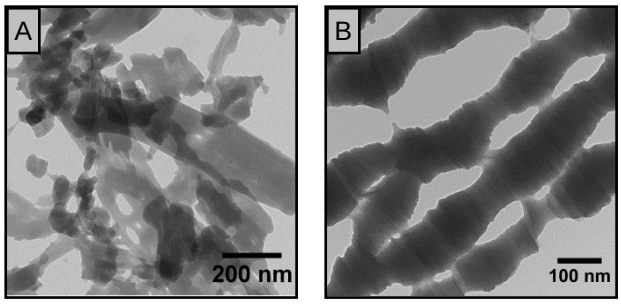

Figure 3.13. Zn-ODP prepared from $Zn(OAc)_2$ and ODPA without (A) and with (B) TOPO present as the co-solvent with octyl ether.

that TOPO may affect the recoverable yield. Upon using the same procedure to separate the nanorods from the residual Zn-ODP, it was found that the resulting solutions contained a higher concentration of ZnO when TOPO had been present in the synthesis (Figure 3.15). There are two possible explanations for these results. The first is that the shape of the Zn-ODP intermediate is important in improving the yield of nanorods produced by the synthesis. One explanation would be that this is due to more Zn-ODP layer edges being available to participate in the reaction due to the different orientations of the layers with the long axis of the structures. A second explanation would be that TOPO improves the ability of the separation procedure to isolate the nanorods from the residual Zn-ODP. This could be due to either a change in the properties of the solvent or by making the quasi-cylinders less "sticky." Based on these results TOPO was used as the co-solvent in all subsequent reactions forming ZnO nanoparticles.

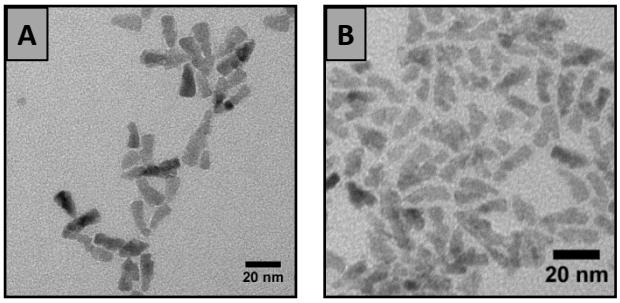

Figure 3.14. ZnO nanorods prepared in the *ZnO nanorod* synthesis without (A) and with (B) TOPO present as the co-solvent with octyl ether.

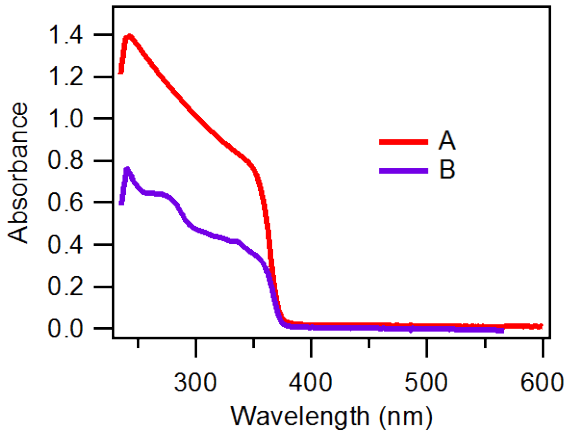

Figure 3.15. UV-Visible spectra of ZnO nanorod solutions recovered from the synthesis. (A) With TOPO, and (B) without TOPO present as the co-solvent during the reaction.

3.2.5 Impact of aliphatic chain length on ZnO nanocrystal shape. Formation of Zn phosphonates is a general phenomenon that occurs for a range of aliphatic chain lengths

(C3, C6, C10, C14), as well as for phenylphosphonic acid (Figure 3.3A-F). ZnO nanocrystals can also be obtained by replacing ODPA with any of these PAs in the complete *ZnO nanorod* synthesis. Figure 3.16 shows TEM of the resulting ZnO nanocrystals for a range of PAs. In the case of propyl (C3) PA, the resulting nanocrystals form aggregates. This suggests that this short PA on the nanocrystal surface does not enable sufficient solubility in organic solvents. When hexyl (C6) PA is used, the resulting nanocrystals are primarily triangular in shape, with bases of 11 ± 3 nm and heights of 15 ± 5 nm. With decyl (C10), tetradecyl (C14), and phenyl PAs, the nanocrystals have rod-like anisotropic shapes and are similar in size and aspect ratio, within one

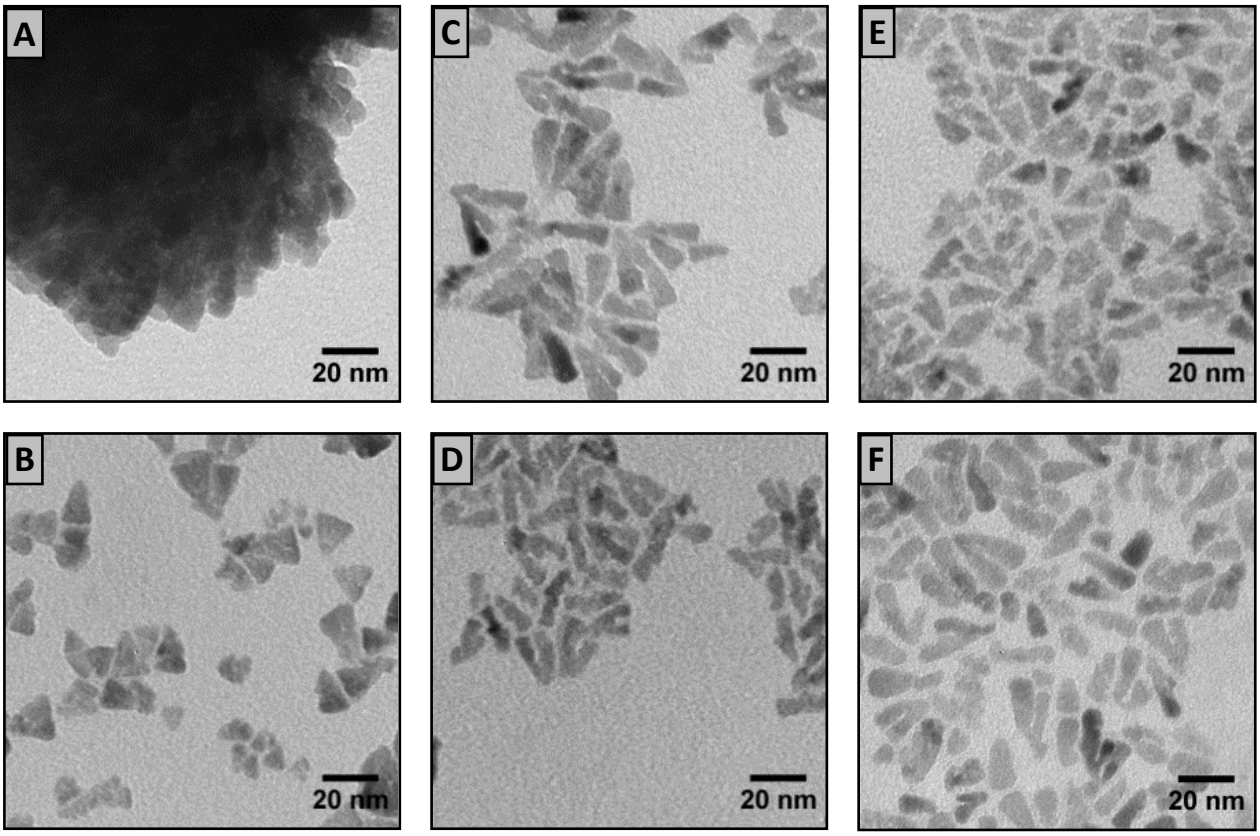

Figure 3.16. TEM images of the nanocrystals that were prepared in the continued reaction of the Zn-PA precursor and residual $Zn(OAc)_2$ with 1-undecanol. The PAs associated with each image: (A)Propyl (C3) phosphonic acid, (B) Hexyl (C6) phosphonic acid, (C) Decyl (C10) phosphonic acid, (D) Tetradecyl (C14) phosphonic acid, (E) Octadecyl (C18) phosphonic acid, and (F) Phenyl phosphonic acid

standard deviation, to those obtained with C18 PA (ODPA) (Table 3.2). This relatively weak dependence of the final particle dimensions on the aliphatic portion of the PA, provided that it is sufficiently long to enable solubilization, is in contrast to a much stronger impact in the case of CdSe nanorods. One report shows an increase in aspect ratio of CdSe nanorods from 2.5 to 18 when the PA aliphatic chain changes from C18 to C6.[43]

Table 3.2. Size measurements of the NCs formed as a result of the reaction of $Zn(OAc)_2$ with 1-undecanol in the presence of phosphonic acids with different R groups. The number of crystals measured for each PA, the length with one standard deviation, the width/base* with one standard deviation, and the aspect ratio from the average values are presented in the columns.

PA	# Measured	Length (nm)	Width (nm)*	Aspect ratio (l:w)
Hexyl (C6)	189	15 ± 5	11 ± 3	1.4 ± 0.6
Decyl (C10)	151	22 ± 5	7 ± 2	3.2 ± 1
Tetradecyl (C14)	155	18 ± 4	6 ± 1	3.0 ± 1
Octadecyl (C18)	338	18 ± 5	7 ± 2	2.5 ± 0.9
Phenyl	113	19 ± 5	7 ± 1	2.7 ± 0.9

*The base of the nanocone was measured for the C6PA and the width at 50% of the length is presented for the remaining PAs.

3.2.6 Stoichiometry of Zn precursors in ZnO nanorod synthesis. The molar ratio of $Zn(OAc)_2$ and ODPA in the starting material mixture for ZnO nanorod synthesis is 1:0.45. Eq. 1 suggests that, if the reaction proceeded to completion, 45% of the Zn precursor would be present in the form of Zn-ODP and the other 55% as $Zn(OAc)_2$ before the addition of 1-undecanol. The extent of $Zn(OAc)_2 \rightarrow$ Zn-ODP conversion was determined by quantitative FTIR. In this experiment, FTIR spectra of the neat reaction mixtures were acquired using a 0.10 mm path-length liquid IR cell. The absorption from solvents overwhelmed most parts of the spectrum (Figure 3.17) but left a window (2500 cm^{-1} to 1500 cm^{-1}) where a minimal solvent absorption could be subtracted. This window was particularly useful for quantification in the

carbonyl region. In Figure 3.18, the absorbance of the carbonyl peak generated by $Zn(OAc)_2$ at approximately 1600 cm^{-1} is shown for the *PA-free* reaction and the *ZnO nanorod* synthesis. These spectra were collected after the precursor formation step and before the 1-undecanol was added. Both reactions started with 1.0 mmol of $Zn(OAc)_2$ in the reaction mixture. However, Figure 3.18 shows that the acetate intensity decreased by 47% (based on the area under the peak) during the precursor formation step in the *ZnO nanorod* synthesis when ODPA was present. This indicates that that the reaction described by Eq. 1 proceeds to completion. Consequently, prior to the addition of 1-undecanol, the reaction mixture of the *ZnO nanorod* synthesis contains $Zn(OAc)_2$ and layered Zn-ODP in approximately equal amounts.

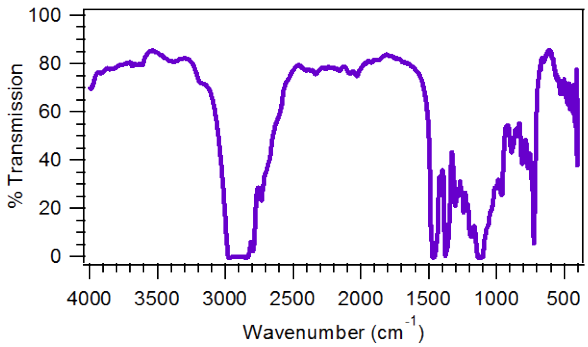

Figure 3.17. FTIR spectrum of octyl ether and TOPO using the 0.1 mm path length liquid FTIR cell. The solvents are in the same ratio as they are in the reaction. There is a window between 2500 cm^{-1} and 1500 cm^{-1} where the solvent absorption can be subtracted.

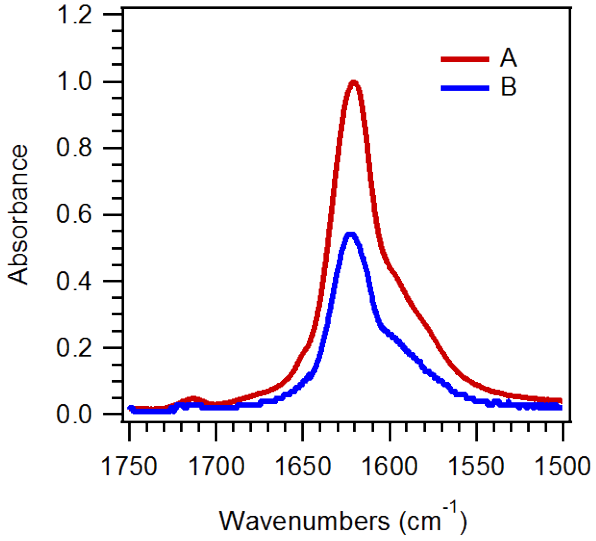

Figure 3.18. The acetate region in quantitative FTIR spectra of the crude reaction collected after the precursor formation step and before the addition 1-undecanol. (A) *PA-free* reaction. (B) *ZnO nanorod* synthesis. The area under the peak of B is 54 % that of the area under A

3.2.7 Relationship between Zn precursor and nanocrystal shape. Given the presence of two distinct Zn precursors in *ZnO nanorod* synthesis, the role of each precursor was

considered. Upon addition of 1-undecanol to the precursor mixture at room temperature, the reaction is heated to 250 °C and allowed to proceed for 120 minutes. Throughout the course of the reaction, the mixture remains cloudy, suggesting that the layered Zn-ODP does not dissolve into molecular components. This is in contrast to the case of CdSe synthesis via Cd-phosphonate, which is optically clear in solution at elevated temperatures, indicating that the complex is a molecular Cd-phosphonate species.[9] Additionally, Cd-phosphonate is the only Cd precursor in the CdSe synthesis indicating that the Zn-phosphonate route to ZnO is more complex. Therefore, three control reactions were performed with the aim to differentiate the effects of the two Zn precursors on the appearance of the final ZnO product (see Methods section). Figure 3.19A shows the product of a reaction similar to *ZnO nanorod* synthesis, with the exception that ODPA was removed and $Zn(OAc)_2$ was present in the amount of 0.55 mmol. This experiment removes the Zn-ODP precursor from the reaction mixture while the $Zn(OAc)_2$ concentration matches that of the *ZnO nanorod* synthesis. This reaction is referred to as *Control A*. The resulting nanocrystals are relatively large (10's of nm), highly polydisperse, isotropic in shape, and aggregated. This experiment demonstrates that Zn-ODP precursor is needed for the formation of smaller, anisotropic, relatively monodisperse, and soluble ZnO nanocrystals. The product of the *Control A* reaction is similar to the one obtained in the *PA-free* reaction described earlier in the text, where 1.0 mmol of $Zn(OAc)_2$

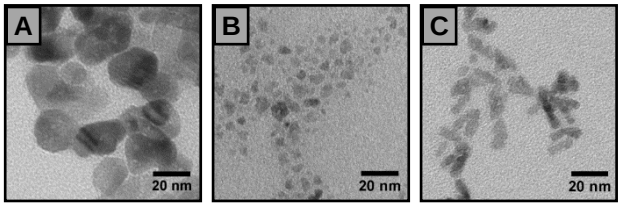

Figure 3.19. Results of ZnO synthesis with varying Zn precursors. (A) Aggregated polydisperse isotropic nanocrystals resulting from the $Zn(OAc)_2$-only reaction (*Control A)*. (B) The small soluble isotropic nanocrystals synthesized in the Zn-ODP-only reaction (*Control B*). (C) Anisotropic monodisperse nanocrystals resulting from the reaction that includes Zn-ODP and $Zn(OAc)_2$ (*Control C*)

was used (Figure 3.1A). This similarity indicates that $Zn(OAc)_2$ concentration is not the deciding factor in the particle shape.

In the experiment referred to as *Control B*, the isolated and purified Zn-ODP (approximately 0.45 mmol) was re-introduced into the octyl ether/TOPO solvent mixture and subjected to the reaction with 1-undecanol under conditions identical to those of the *ZnO nanorod* synthesis. The product consists of relatively small, polydisperse, soluble ZnO nanocrystals that are isotropic in shape (Figure 3.19B). Finally, when the isolated and purified Zn-ODP (0.45 mmol) was combined with 0.55 mmol of $Zn(OAc)_2$ in the solvent mixture (*Control C*), the resulting product was small, anisotropic, ZnO nanocrystals (Figure 3.19C) very similar in appearance to those shown in Figure 3.1B. This set of control experiments demonstrates that, while Zn-ODP alone can produce small ZnO nanocrystals, both $Zn(OAc)_2$ and Zn-ODP are required for the formation of ZnO nanorods. The relationship between Zn precursors and the appearance of the resulting ZnO nanocrystals is summarized in Figure 3.20.

3.2.8 Kinetics of $Zn(OAc)_2$ conversion. Quantitative FTIR measurements were utilized to understand how the presence of ODPA in the starting material mixture impacts the kinetics of the $Zn(OAc)_2$ reaction with 1-undecanol. This was achieved by collecting aliquots at various points during the reaction and acquiring FTIR spectra of the neat reaction mixture using a 0.10 mm path-length liquid IR cell. It has been shown that in the absence of

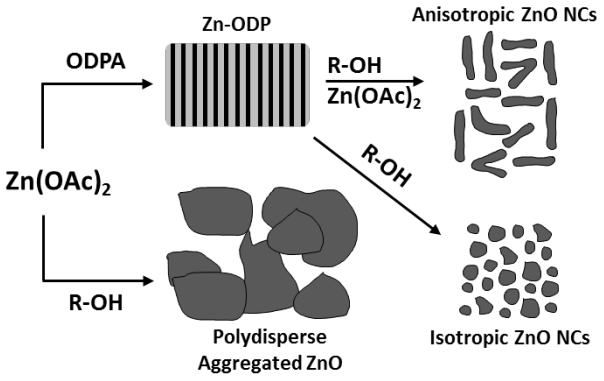

Figure 3.20. A summary of the reaction pathways for $Zn(OAc)_2$ to ZnO in the presence and absence of ODPA.

PAs, $Zn(OAc)_2$ reacts with alcohols via ester elimination to produce $Zn(OH)_2$ (Figure 3.21A), which in turn leads to ZnO nanocrystals via a condensation reaction that eliminates water.[12, 23] The $Zn(OAc)_2$ reactant and the ester product are readily identifiable by FTIR.[12] As with the previous quantitative FTIR experiment, the relatively low absorbance of the solvent in the window (Figure 3.17) required to quantitate the acetate and ester carbonyl peaks allowed the concentration of each to be followed throughout the reaction.

Figure 3.21 shows a comparison of the FTIR spectra (with solvent signal subtracted) during the *ZnO nanorod* synthesis and the reaction lacking Zn-ODP (*Control A*). The aliquots are taken during the nanocrystal formation (i.e., after addition of 1-undecanol) when the reaction reaches the following points: (i) room temperature, (ii) 150 °C, (iii) 175 °C, (iv) 200 °C, (v) 225 °C, (vi) 250 °C, (vii) the crude final reaction mixture after 120 minutes at 250 °C. The broader peak around 1600 cm^{-1} is assigned to $Zn(OAc)_2$, and the narrower peak near 1750 cm^{-1} corresponds to the carbonyl group of the ester formed when $Zn(OAc)_2$ reacts with alcohol to form $Zn(OH)_2$

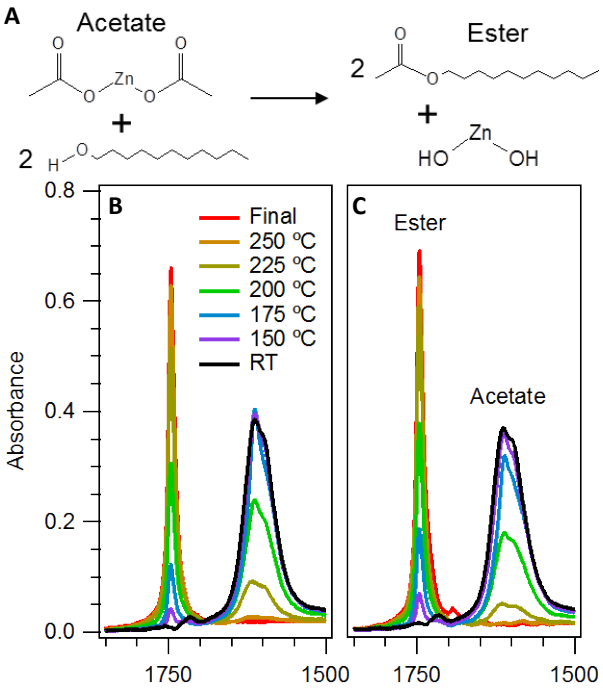

Figure 3.21. (A) Reaction scheme for the ester elimination that converts acetate into ester and $Zn(OH)_2$. A comparison of the FTIR spectra (with solvent signal subtracted) during (B) the reaction lacking Zn-ODP (*Control A*) and (C) the *ZnO nanorod* synthesis. The aliquots are taken during the nanocrystal formation (i.e., after addition of 1-undecanol) when the reaction reaches the following points: (i) room temperature, (ii) 150 °C, (iii) 175 °C, (iv) 200 °C, (v) 225 °C, (vi) 250 °C, (vii) the crude final reaction mixture after 120 minutes at 250 °C.

(Figure 3.21A).[12, 23] In the absence of Zn-ODP (Figure 3.21B), the first 18% of $Zn(OAc)_2$ has reacted by the time the reaction reaches 175 °C. The conversion proceeds to 46% by 200 °C, 78% by 225 °C, and 95% by the time it reaches 250 °C. Similar kinetics were observed previously with 1,12-dodecanediol.[12] The kinetics of $Zn(OAc)_2$ reaction with 1-undecanol are qualitatively similar in the presence of Zn-ODP (Figure 3.21C), with the conversion values of 27%, 55%, 85%, and 93% respectively at the corresponding temperatures. This similarity indicates that the production of $Zn(OH)_2$ from $Zn(OAc)_2$ proceeds at the same rates with and without Zn-ODP, and suggests that the impact of the ODPA addition occurs after $Zn(OH)_2$ is formed. Unfortunately, the solvent signal prevents an investigation of the O-H and P-O regions of the FTIR spectrum, precluding the investigation of a possible reaction between $Zn(OH)_2$ and Zn-ODP.

3.2.9 Impact of Zn-ODP on ZnO nanocrystal nucleation and growth. The aliquots removed from reaction mixtures for FTIR analysis described above were also analyzed by TEM without purification to characterize ZnO nanocrystal nucleation and growth. Figure 3.22 shows representative TEM images of the reaction mixtures at several stages for the following reactions: *Control A* (absence of ODPA), *Control B* (absence of $Zn(OAc)_2$), and the *ZnO nanorod* synthesis. In *Control A*, nanocrystals were present at temperatures as low as 150 °C. At 200 °C, aggregation of nanocrystals, similar to a previous report,[12] was observed. At higher temperatures, up to 250 °C, the nanocrystals are less aggregated, and are highly polydisperse in size and shape. In *Control B*, nucleation of considerably smaller nanocrystals (~5 nm in diameter) is observed also at 150 °C. With increasing temperature, some growth of nanocrystals is observed, along with the consistent presence of Zn-ODP. In contrast to these

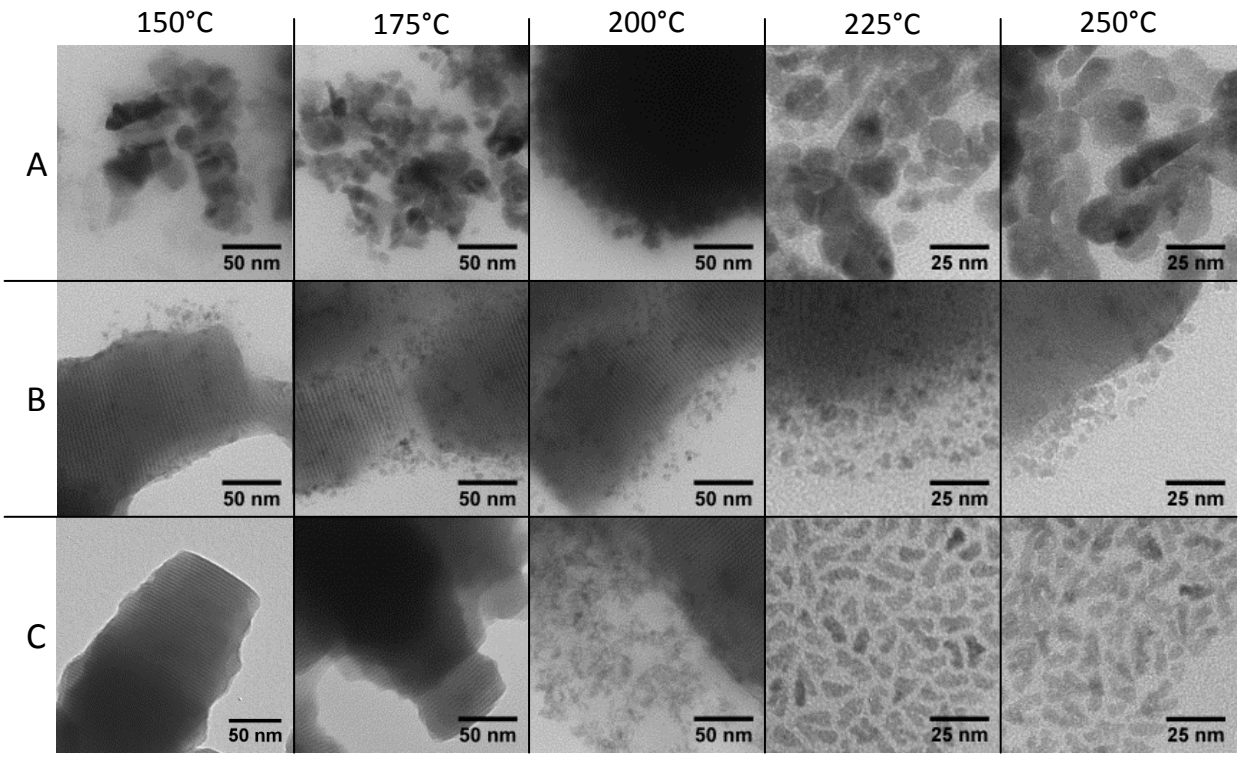

Figure 22. TEM images collected from experiments following the ZnO nanocrystal formation in three reactions testing the role of the Zn precursors. Aliquots were removed after the alcohol was added while heating to 250°C. The temperature points are divided into columns: 150 °C, 175 °C, 200 °C, 225 °C, and 250 °C. The rows represent different reactions: (A) Control A, the reaction with only 0.55 mmol of the $Zn(OAc)_2$ present. (B) Control B, a reaction with only the Zn-ODPA present after being formed under normal conditions, purified, and returned to a new flask with only the solvents present. (C) The full *ZnO nanorod* synthesis reaction with both Zn-ODPA and $Zn(OAc)_2$ present.

control experiments, the *ZnO nanorod* synthesis, which uses both $Zn(OAc)_2$ and Zn-ODP as precursors, exhibits delayed nucleation a higher temperature (200 °C) than nucleation in *Control A* or *Control B*. The small nuclei are formed into anisotropic nanocrystals by the time the reaction mixture reaches 225 °C and the product appears relatively unchanged between this point and 250 °C. The evidence in Figure 3.22 suggests that nanocrystal nucleation is delayed when both precursors are present when compared to the reactions of the individual precursors with 1-undecanol. This suggests that an alternative pathway to ZnO is created when both precursors are present.

3.2.10 Chemical reactions in ZnO nanorod synthesis. Based on the evidence in the previous sections several reaction pathways involving PAs for the formation of ZnO have been derived. As previously reported, in the *PA-free* ZnO synthesis, $Zn(OAc)_2$ reacts with alcohols via an ester elimination reaction to produce $Zn(OH)_2$ (Figure 3.21A). Then, $Zn(OH)_2$ reacts to form ZnO nanocrystals, such as the ones shown in Figure 3.1A, via a condensation reaction that eliminates H_2O.[12, 23] The $Zn(OAc)_2$ reactant and the ester product were readily identifiable by FTIR and the reaction was discussed in detail in the previous sections.[12] In the presence of PAs, the possibilities for chemical reactions become more numerous. Figure 3.21B shows the quantitative FTIR spectra in the carbonyl region (with solvent signal subtracted) for *ZnO nanorod* synthesis and for *Control A* reaction at room temperature (immediately after injection of 1-undecanol) and in the final product. In both cases, the acetate → ester conversion follows very similar kinetics in the presence and absence of ODPA (Figure 3.21), suggesting that the $Zn(OAc)_2$ → $Zn(OH)_2$ conversion is not strongly perturbed by the presence of Zn-ODP. However, a reaction of $Zn(OH)_2$ with Zn-ODP can be considered as an analogy to a reaction of ^-OH with a phosphoester, resulting in a condensation that liberates ODPA:

Equation 3

$$n\ Zn(OH)_2 + n\ Zn\text{-}ODP \rightarrow (Zn\text{-}O)_{2n} + n\ H_2ODP$$

where ODPA is written as H_2ODP to emphasize the two acidic protons. The ODPA released in this reaction can become the surface phosphonate ligand that imparts on the ZnO nanorods solubility in organic solvents. Another possible reaction of Zn-ODP involves 1-undecanol, in analogy to the $Zn(OAc)_2$ reaction with 1-undecanol:

Equation 4

$$Zn\text{-}ODP + 2\ C_{11}H_{23}\text{-}OH \rightarrow Zn(OH)_2 + (C_{11}H_{24})_2ODP$$

followed by the condensation of $Zn(OH)_2$. Unfortunately, $(C_{11}H_{23})_2ODP$ could also be the product of a reaction of ODPA (released in Eq. 3) with 2 equivalents $C_{11}H_{23}$-OH, so its detection would not provide unambiguous distinction between Eq. 3 and Eq. 4. Finally, the H_2O released in condensation of $Zn(OH)_2$ could react with Zn-ODP as follows:

Equation 5

$$\text{Zn-ODP} + 2\ H_2O \rightarrow Zn(OH)_2 + H_2ODP$$

This reaction could be followed by condensation of $Zn(OH)_2$. Because of the similarity of products with Eq. 3 and Eq. 4, this reaction cannot be definitively ruled out. Clearly, the presence of Zn-ODP in the reaction mixture that leads to ZnO nanorods introduces several possible chemical pathways and sets a challenge in understanding the chemistry that leads to anisotropic ZnO nanocrystals.

3.3 Conclusions and Future Directions

Alkylphosphonic acids play an important role in the synthesis of anisotropic ZnO nanocrystals. The $Zn(OAc)_2$ precursor reacts with the phosphonic acid in early stages of the reaction to form a layered Zn-phosphonate complex. However, all of the $Zn(OAc)_2$ is not converted to the phosphonate complex (Zn-ODP), which leaves two Zn precursors available to react with 1-undecanol and form ZnO. Evidence collected by studying the reaction of the two precursors individually led to some interesting discoveries. The rate of $Zn(OH)_2$ formation from $Zn(OAc)_2$ does not appear to change when Zn-ODP is present, even though the formation of nanocrystals is delayed during the nanocrystal formation step. This result leads to a conclusion that if Zn-ODP is present, the $Zn(OH)_2$ conversion to ZnO is delayed, resulting in a higher monomer concentration upon the eventual nucleation of nanocrystals. Comparably, in the synthesis of wurtzite CdSe nanocrystals, high monomer concentrations generate anisotropically

grown nanocrystals.[3, 4] That leads to the conclusion that the anisotropic nature of the ZnO nanocrystals that result from this synthesis also originates from increased monomer concentration after nucleation.

A more general implication of the research presented in this chapter is the notion of utilizing multiple precursors for the same element as an additional parameter in nanocrystal syntheses. Having more than one precursor for each element would lead to multiple chemical routes to monomer species in solution, with each route occurring at its own temperature dependent rate. This would allow for the monomer concentration to be fine-tuned at various points in the reaction. Since monomer concentration has been linked the directionality of nanocrystal growth,[3, 4] varying the temperature could allow for varying periods of isotropic and anisotropic growth based on the activation of multiple chemical routes from precursor to nanocrystal. This hypothesis, based on this study of the role of PAs in ZnO nanocrystal synthesis, is in contrast to the impact of PAs on CdSe nanocrystal syntheses.[7] In the CdSe synthesis, the presence of PAs allows the use of a multitude of Cd precursors because of their complete conversion to Cd-phosphonate in early stages of the reaction.[8] As a result, the impact of PAs on the CdSe synthesis was to provide a single Cd source used in many syntheses. The benefits of this discovery were the realization that the safer and more sTable 3.Cd precursors (e.g., CdO) could be used as a Cd source instead of the flammable and toxic $Cd(CH_3)_2$ (since both readily convert to Cd-phosphonate). In the ZnO nanocrystal synthesis presented here, the impact the PA was to provide a second Zn precursor (in addition to $Zn(OAc)_2$), which demonstrated the power utilizing different metal precursors in the same nanocrystal synthesis.

The benefit here was the ability to generate anisotropic ZnO nanocrystals, but future work could uncover additional benefits of multiple metal precursors in other syntheses.

3.4 Experimental

3.4.1 Chemicals: All chemicals were purchased from a commercial source and used without further purification: $Zn(OAc)_2$ (99.99%), $ZnCl_2$ (98+%), trioctylphosphine oxide (TOPO, 99%), dioctyl ether (99%), 1-undecanol (99%), propyl (C3) phosphonic acid (95%), and phenyl phosphonic acid (98%) were purchased from Sigma Aldrich. Octadecyl (C18) phosphonic acid (ODPA, 99+%), hexyl (C6) phosphonic acid (99+%), and tetradecyl (C14) phosphonic acid (99+%) were purchased from PCI Synthesis (9 Opportunity Way, Newburyport, MA01950, 978-463-4853). Decyl (C10) phosphonic acid (98%) was purchased from Alfa Aesar.

3.4.2 ZnO Nanorod Synthesis: This synthesis is a modified version of a previously reported procedure.[12] $Zn(OAc)_2$ (1 mmol), R-PA (0.45 mmol, R=C3, C6, C10, C14, C18, phenyl), TOPO (3 mmol), and octyl ether (7.5 mL) were combined in a 3-neck round bottom flask fitted with a condenser, septum, and glass thermocouple adaptor. In the drying step, the mixture was magnetically stirred under vacuum at 100 °C for 30 minutes. The flask was then placed under argon and heated to 200 °C for one hour (precursor formation step). To isolate the insoluble intermediate, the reaction was cooled to room temperature at this point, and the solid was precipitated using a 1:1 ethanol:methanol mixture. This solid was then washed three times by suspending in chloroform and precipitating with a 1:1 ethanol:methanol mixture. To synthesize anisotropic ZnO nanocrystals, the reaction mixture at 200 °C was cooled to 60 °C and argon-purged 1-undecanol (6 mmol) was added via syringe using air-free techniques. The flask was heated to 250 °C for 2 hours under argon. After cooling to room temperature, the

nanorods were isolated by precipitating with methanol. The resulting solid was then dissolved in hexanes and centrifuged, leaving a supernatant containing the nanorod product.

3.4.3 Control Reactions to Isolate the Zn Precursors. Control A: The ZnO nanorod synthesis starting with $Zn(OAc)_2$ (0.55 mmol), TOPO (3 mmol), and octyl ether (7.5 mL) without the presence of PA was carried out as described above, including the drying, precursor formation, and nanocrystal formation steps. **Control B:** Zn-ODP complex (~0.45 mmol) (isolated and purified as described above) was reintroduced into a solvent of octyl ether (7.5 mL) and TOPO (3 mmol) and dried under vacuum at 100 °C for 30 minutes. After cooling to 60 °C, argon-purged 1-undecanol (6 mmol) was added via syringe using air-free techniques. The flask was heated to 250 °C for 2 hours under argon. **Control C**: The procedure was identical to that for Control B except that $Zn(OAc)_2$ (0.55 mmol) was added to the octyl either and TOPO solvents along with the isolated Zn-ODP.

3.4.4 Monitoring the Reaction: The *ZnO nanorod* synthesis reaction and all three control reactions (A, B, and C) were monitored by FTIR and TEM. 0.5 mL aliquots were removed using a glass syringe and air-free techniques at desired time points during the course of the synthesis (see text). The aliquots were dropped into a vial containing liquid nitrogen to rapidly quench the reaction and the sample vials were stored at -20 °C until immediately prior to analysis. The neat reaction aliquots were analyzed by FTIR and dilute solutions were used to prepare TEM samples.

3.4.5 Aqueous Zinc Phosphonate Hydrate Synthesis: This procedure is a modified version of a previously reported synthesis.[26] For Zn-ODP, $ZnCl_2$ (1 mmol) was dissolved in 30 mL of 18.2 MΩ water and ODPA (1 mmol) was dissolved in 100 mL methanol. For Zn-

phenylphosphonate, 1 g of $ZnCl_2$ (7.3 mmol) and an equimolar amount of phenylphosphonic acid (7.3 mmol) were each dissolved in 20 mL of 18.2 MΩ water. In both cases, the PA solution was added to the $ZnCl_2$ solution. While stirring, NaOH was added until the pH was greater than 6. Upon NaOH addition, a white precipitate formed and was collected by centrifugation. The precipitate was then washed with methanol.

3.4.6 Electron Microsopy. All TEM samples were prepared by dropping dilute solutions on carbon coated copper 300 mesh grids (Electron Microscopy Sciences PN: CF300-Cu). Standard resolution transmission electron microscope (TEM) images were collected on a Phillips CM100 microscope operating at 80-100 kV. High resolution TEM images (HR-TEM) were collected on a JEOL JEM 2000-FX TEM operating at 200 kV. STEM-EELS imaging and elemental map ping were performed by FEI Company (Hillsboro, OR) on a FEI Tecnai Osiris™ TEM. SEM samples were prepared by dropping sample solutions on a piece of silicon wafer attached to an aluminum stub with conductive carbon tape and evaporating the solvent. SEM images were collected on a JEOL JSM-7401F scanning electron microscope at 1.0 kV acceleration voltage.

3.4.7 ZnO nanocrystal size measurements. Nanocrystal sizes were measured using the software package ImageJ available as freeware online. The nanorods prepared with C10, C14, C18, and phenyl PAs' longest axis was measured as the "length," and the "width" was measured at perpendicular to that axis at 50% of the length. Nano-cones prepared with C6 PA were measured from the tip of the cone to the base for the "length" and the base of the cone was measured as the "width." 189, 151, 155, 338, and 113 particles were measured for the nanocrystals made from the C6, C10, C14, C18, and phenyl PAs respectively.

3.4.8 Powder X-Ray diffraction (XRD). XRD data was collected on a Scintag Pad V diffractometer operating at 25 mA and -40 kV using the CuKα x-ray line (0.1540562 nm). XRD samples were prepared by depositing sample solutions on glass slides, and drying at 60 °C in air.

3.4.9 Spectroscopy. UV-visible absorption spectra were collected on an Agilent 8453 UV-visible spectrophotometer. Fourier transform infrared (FTIR) spectra were either collected by drying samples on International Crystal Labs KBr Real Crystal IR Cards or using an International Crystal Laboratories SL-3 Liquid cell with KBr windows and a 0.1 mm path length. Neat 0.5 ml reaction aliquots were injected directly into the liquid cell for the quantitative FTIR experiments. For the high-temperature data shown in Figure 3.21 and Figure 3.22, neat aliquots were first injected into liquid N_2 to quench the reaction. Spectra were collected on a Thermo Nicolet Avatar 360 FTIR using an average of 64 scans at a 1 cm^{-1} resolution.

3.4.10 ^{31}P solid state NMR. NMR spectra were acquired on a narrow-bore Varian INOVA 400 NMR spectrometer system, operating at 161.988 MHz for ^{31}P observation. MAS experiments were performed using a 5mm MAS spinning assembly and zirconia rotors manufactured by Revolution NMR, Inc. (Fort Collins, CO), which provides excellent spinning stability of ± 10 Hz for the spinning sideband analysis. Single-pulsed excitation MAS NMR experiments were performed using a 45^0 excitation pulse of 2.8 μs, with broadband ^{1}H TPPM decoupling, using 72 KHz cw decoupling field strength. Spectra shown are the result of 128-256 scans with a 10 sec. relaxation delay between scans. Chemical shifts were referenced indirectly to zero ppm ^{1}H NMR, using the absolute configuration frequency of the spectrometer. This referencing was checked against a sample of pure triphenylphosphine (TPP), yielding an observed absolute chemical shift of -8.4 PPM for TPP.[44] Spectral simulations were performed

to determine principal components of the chemical shift tensors via spinning sideband analysis under slow MAS using the STARS (Spectrum Analysis of Rotating Solids) simulation package developed by the Jakobsen group at the University of Aarhus, as implemented in the VNMRJ 3.2 software (Agilent Technologies).[45]

3.5 References

1. Manna, L.; Scher, E. C.; Alivisatos, A. P., Synthesis of soluble and processable rod-, arrow-, teardrop-, and tetrapod-shaped CdSe nanocrystals. *J. Am. Chem. Soc.* 2000, 122, 12700-12706.

2. Peng, X. G.; Manna, L.; Yang, W. D.; Wickham, J.; Scher, E.; Kadavanich, A.; Alivisatos, A. P., Shape control of CdSe nanocrystals. *Nature* 2000, 404, 59-61.

3. Peng, Z. A.; Peng, X. G., Mechanisms of the shape evolution of CdSe nanocrystals. *J. Am. Chem. Soc.* 2001, 123, 1389-1395.

4. Peng, Z. A.; Peng, X. G., Nearly monodisperse and shape-controlled CdSe nanocrystals via alternative routes: Nucleation and growth. *J. Am. Chem. Soc.* 2002, 124, 3343-3353.

5. Yin, Y.; Alivisatos, A. P., Colloidal nanocrystal synthesis and the organic-inorganic interface. *Nature* 2005, 437, 664-670.

6. Milliron, D. J.; Hughes, S. M.; Cui, Y.; Manna, L.; Li, J. B.; Wang, L. W.; Alivisatos, A. P., Colloidal nanocrystal heterostructures with linear and branched topology. *Nature* 2004, 430, 190-195.

7. Peng, Z. A.; Peng, X. G., Formation of high-quality CdTe, CdSe, and CdS nanocrystals using CdO as precursor. *J. Am. Chem. Soc.* 2001, 123, 183-184.

8. Liu, H. T.; Owen, J. S.; Alivisatos, A. P., Mechanistic study of precursor evolution in colloidal group II-VI semiconductor nanocrystal synthesis. *J. Am. Chem. Soc.* 2007, 129, 305-312.

9. Owen, J. S.; Chan, E. M.; Liu, H.; Alivisatos, A. P., Precursor Conversion Kinetics and the Nucleation of Cadmium Selenide Nanocrystals. *J. Am. Chem. Soc.* 2010, 132, 18206-18213.

10. Wang, F.; Tang, R.; Buhro, W. E., The Trouble with TOPO; Identification of Adventitious Impurities Beneficial to the Growth of Cadmium Selenide Quantum Dots, Rods, and Wires. *Nano Lett.* 2008, 8, 3521-3524.

11. Gomes, R.; Hassinen, A.; Szczygiel, A.; Zhao, Q.; Vantomme, A.; Martins, J. C.; Hens, Z., Binding of Phosphonic Acids to CdSe Quantum Dots: A Solution NMR Study. *J. Phys. Chem. Lett.* 2011, 2, 145-152.

12. Joo, J.; Kwon, S. G.; Yu, J. H.; Hyeon, T., Synthesis of ZnO nanocrystals with cone, hexagonal cone, and rod shapes via non-hydrolytic ester elimination sol-gel reactions. *Adv. Mater. (Weinheim, Ger.)* 2005, 17, 1873-+.

13. Ozgur, U.; Alivov, Y. I.; Liu, C.; Teke, A.; Reshchikov, M. A.; Dogan, S.; Avrutin, V.; Cho, S. J.; Morkoc, H., A comprehensive review of ZnO materials and devices. *J. Appl. Phys.* 2005, 98.

14. Niederberger, M., Nonaqueous sol-gel routes to metal oxide nanoparticles. *Acc. Chem. Res.* 2007, 40, 793-800.

15. Shim, M.; Guyot-Sionnest, P., Organic-Capped ZnO Nanocrystals: Synthesis and n-Type Character. *J. Am. Chem. Soc.* 2001, 123, 11651-11654.

16. Demir, M. M.; Munoz-Espi, R.; Lieberwirth, I.; Wegner, G., Precipitation of monodisperse ZnO nanocrystals via acid-catalyzed esterification of zinc acetate. *J. Mater. Chem.* 2006, 16, 2940-2947.

17. Choi, S. H.; Kim, E. G.; Park, J.; An, K.; Lee, N.; Kim, S. C.; Hyeon, T., Large-scale synthesis of hexagonal pyramid-shaped ZnO nanocrystals from thermolysis of Zn-oleate complex. *J. Phys. Chem. B* 2005, 109, 14792-14794.

18. Andelman, T.; Gong, Y.; Polking, M.; Yin, M.; Kuskovsky, I.; Neumark, G.; O'Brien, S., Morphological Control and Photoluminescence of Zinc Oxide Nanocrystals. *J. Phys. Chem. B* 2005, 109, 14314-14318.

19. Yin, M.; Gu, Y.; Kuskovsky, I. L.; Andelman, T.; Zhu, Y.; Neumark, G. F.; O'Brien, S., Zinc Oxide Quantum Rods. *J. Am. Chem. Soc.* 2004, 126, 6206-6207.

20. Zhang, Z.; Lu, M.; Xu, H.; Chin, W.-S., Shape-Controlled Synthesis of Zinc Oxide: A Simple Method for the Preparation of Metal Oxide Nanocrystals in Non-aqueous Medium. *Chem.--Eur. J.* 2007, 13, 632-638.

21. Cozzoli, P. D.; Curri, M. L.; Agostiano, A.; Leo, G.; Lomascolo, M., ZnO nanocrystals by a non-hydrolytic route: Synthesis and characterization. *J. Phys. Chem. B* 2003, 107, 4756-4762.

22. Chen, Y. F.; Kim, M.; Lian, G.; Johnson, M. B.; Peng, X. G., Side reactions in controlling the quality, yield, and stability of high quality colloidal nanocrystals. *J. Am. Chem. Soc.* 2005, 127, 13331-13337.

23. Kwon, S. G.; Hyeon, T., Colloidal Chemical Synthesis and Formation Kinetics of Uniformly Sized Nanocrystals of Metals, Oxides, and Chalcogenides. *Acc. Chem. Res.* 2008, 41, 1696-1709.

24. Seip, C. T.; Granroth, G. E.; Meisel, M. W.; Talham, D. R., Langmuir-Blodgett films of known layered solids: Preparation and structural properties of octadecylphosphonate bilayers with divalent metals and characterization of a magnetic Langmuir-Blodgett film. *J. Am. Chem. Soc.* 1997, 119, 7084-7094.

25. Cunningham, D.; Hennelly, P. J. D., Divalent Metal Phenylphosphonates and Phenylarsonates. *Inorg. Chim. Acta* 1979, 37, 95-102.

26. Cao, G.; Lee, H.; Lynch, V. M.; Mallouk, T. E., Synthesis And Structural Characterization of a Homologous Series of Divalent-Metal Phosphonates, MII(O3PR).H2O And MII(HO3PR)2. *Inorg. Chem.* 1988, 27, 2781-2785.

27. Cao, G.; Mallouk, T. E., Shape-Selective Intercalation Reactions of Layered Zinc And Cobalt Phosphonates. *Inorg. Chem.* 1991, 30, 1434-1438.

28. Guang, C.; Hong, H. G.; Mallouk, T. E., Layered Metal Phosphates And Phosphonates - From Crystals to Monolayers. *Acc. Chem. Res.* 1992, 25, 420-427.

29. Massiot, D.; Drumel, S.; Janvier, P.; BujoliDoeuff, M.; Bujoli, B., Relationship between solid-state P-31 NMR parameters and X-ray structural data in some zinc phosphonates. *Chem. Mater.* 1997, 9, 6-&.

30. Martin, K. J.; Squattrito, P. J.; Clearfield, A., The Crystal and Molecular-Strucuture of Zinc Phenylphosphonate. *Inorg. Chim. Acta* 1989, 155, 7-9.

31. Gao, W.; Dickinson, L.; Morin, F. G.; Reven, L., Phase transitions in lamellar alkylphosphonate salts. *Chem. Mater.* 1997, 9, 3113-3120.

32. Clearfield, A., Chapter 1 The Early History and Growth of Metal Phosphonate Chemistry. In *Metal Phosphonate Chemistry: From Synthesis to Applications*, The Royal Society of Chemistry: 2012; Vol. 0, pp 1-44.

33. Clearfield, A., Recent advances in metal phosphonate chemistry. *Curr. Opin. Solid State Mater. Sci.* 1996, 1, 268-278.

34. Fredoueil, F.; Penicaud, V.; BujoliDoeuff, M.; Bujoli, B., Syntheses and crystal structures of the new zinc phosphonates Zn(O3PCH2P)(O)(R)(C6H5))center dot xH(2)O, based on mixed phosphonic acid phosphine oxide building blocks. *Inorg. Chem.* 1997, 36, 4702-4706.

35. Frink, K. J.; Wang, R. C.; Colon, J. L.; Clearfield, A., Intercalation of Ammonia Into Zinc and Cobalt Phenylphosphonates. *Inorg. Chem.* 1991, 30, 1438-1441.

36. Poojary, D. M.; Zhang, B. L.; Bellinghausen, P.; Clearfield, A., Synthesis and X-ray powder structures of covalently pillared lamellar zinc bis(phosphonates). *Inorg. Chem.* 1996, 35, 5254-5263.

37. Deemie, R. W.; Knight, A.; Rao, M., An organometallic sol-gel route to layered zinc phenylphosphonate and encapsulation studies with eta(6)-(C6H6)Cr(CO)(3). *J. Organomet. Chem.* 1999, 585, 162-166.

38. Gerbier, P.; Guerin, C.; Henner, B.; Unal, J. R., An organometallic route to zinc phosphonates and their intercalates. *J. Mater. Chem.* 1999, 9, 2559-2565.

39. Luschtinetz, R.; Seifert, G.; Jaehne, E.; Adler, H.-J. P., Infrared Spectra of Alkylphosphonic Acid Bound to Aluminium Surfaces. *Macromol. Symp.* 2007, 254, 248-253.

40. Snyder, R. G.; Strauss, H. L.; Elliger, C. A., C-H Stretching Modes and the Structure of Normal-Alkyl Chains. 1. Long, Disordered Chains. *J. Phys. Chem.* 1982, 86, 5145-5150.

41. Thomas, L. C.; Chittend.Ra, Characteristic Infrared Absorption Frequencies of Organophosphorus Compounds-VII. Phosphorus Ions. *Spectrochim. Acta, Part A* 1970, A 26, 781-&.

42. Thomas, L. C.; Chittenden, R. A., Characteristic Infrared Absorption Frequencies of Organophosphorus Compounds. 1. The Phosphoryl (P=O) Group. *Spectrochim. Acta* 1964, 20, 467-487.

43. Wang, W.; Banerjee, S.; Jia, S.; Steigerwald, M. L.; Herman, I. P., Ligand Control of Growth, Morphology, and Capping Structure of Colloidal CdSe Nanorods. *Chem. Mater.* 2007, 19, 2573-2580.

44. Harris, R. K.; Becker, E. D.; De Menezes, S. M. C.; Granger, P.; Hoffman, R. E.; Zilm, K. W., Further conventions for NMR shielding and chemical shifts (IUPAC recommendations 2008). *Pure Appl. Chem.* 2008, 80, 59-84.

45. Skibsted, J.; Nielsen, N. C.; Bildsoe, H.; Jakobsen, H. J., Satellite Transitions In MAS NMR-Spectra of Quadrupolar Nuclei. *J. Magn. Reson.* 1991, 95, 88-117.

Chapter 4. Isolation of RNA Sequences with Facet Specific Platinum Surface Binding Through *in vitro* Selection

4.1 Introduction

There is a strong correlation between a nanoparticle catalyst's activity and its surface structure.[1] Unfortunately, there is currently no way of designing *a priori* a nanoparticle synthetic scheme that will yield a product with a desired morphology or surface structure. Advances in nano-structured catalysts are thus rare and rely almost exclusively on trial and error. The traditional method of nanoparticle catalyst discovery is one in which nanoparticles with novel morphologies and surface structures are discovered fortuitously after many iterations of adjusting synthesis conditions. Then, those new nanoparticle morphologies are studied for their potential applications. Conversely, development of a method by which nanoparticles with a desired surface structure are synthesized deterministically, would streamline the catalyst discovery process dramatically. In that case, one would be able to identify a specific surface structure best fit for a specific catalytic application via simulation or experiment, and then produce nanoparticles with that surface structure, without trial and error. The hypothesis for this work was that deterministic control over surface morphology could be achieved by designing a capping ligand that will bind specifically to a desired surface structure of a material. Subsequently, that ligand could be used to control the growth of nanoparticles of that material via the "selective adhesion" mechanism discussed in Chapter 1. Therefore, upon being presented with a desired metal composition and surface structure, this method could identify capping ligands capable of mediating the formation of nanoparticles of that metal with the desired surface structure. While hypothesized as being universal for all

metal compositions, platinum was chosen as the test case for the method's development because of its technological relevance and the surface structure dependent catalytic activity of platinum nanoparticles.

Platinum nanoparticles (Pt NPs) have been identified as active and efficient catalysts for several applications, including electrocatalysts in fuel cells.[2] The high catalytic activity of Pt NPs is in part a consequence of their high surface to volume ratio, providing an increased number of surface atoms available to participate in reactions.[3] Further improvements in catalytic activity have been found to correlate to the percentage of surface atoms present on edges and corners because those atoms have a lower coordination and are thus higher in energy.[4] Therefore, it was discovered that one way of tailoring the catalytic activity of Pt NPs has been to alter their surface structure so that more catalytically active low coordination surface atoms are available to participate in reactions.[4-8] Platinum has a face centered cubic (FCC) closest packed crystal structure.[2] Figure 4.1A shows the FCC unit cell containing atoms at all eight corners of a cube and one atom in each of the six faces. Directions through the crystal structure are defined by Miller indices of the format (*hkl*) with the (100) and (111) directions shown in Figure 4.1B&C. Pt NPs are usually polyhedra, with the three low energy facets [(111), (100), and (110)] covering each face of the polyhedron.[2] Since facets with different miller indices intersect each other at different angles,

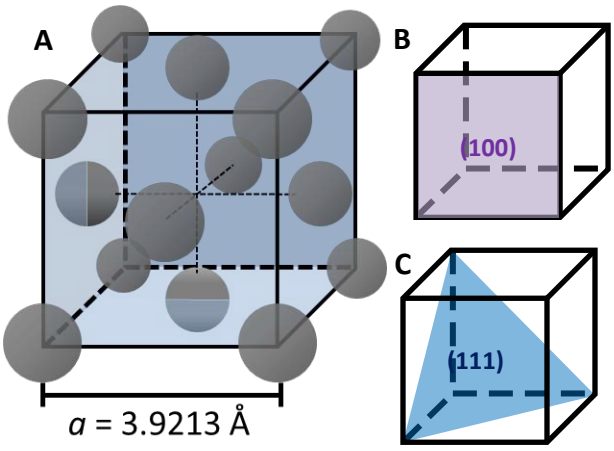

Figure 4.1. (A) Unit cell of a FCC crystal structure with atoms at the 8 corners of a cube and one atom in each of the six faces. Also pictured are the (100) plane (B) and the (111) plane (C) of a cubic crystal structure.

the shape of the product nanoparticles is directly correlated to the facet on their surface. For example, (100) facets intersect at 90° angles and consequently, nanoparticles with (100) facets on their surfaces typically have cubic shapes. The first reports of syntheses of Pt NPs with high shape monodispersity were generated using the polymer polyacrylate as the NP capping agent.[9] The synthesis produced (111) faced tetrahedral and (100) faced cubic Pt NPs simply by controlling the ratio of polyacrylate to platinum precursor.[9] Upon further study of those particles, the (111) faced tetrahedral NPs were found to be better catalysts than the (100) cubic or multi-faceted spherical particles.[6] Since that initial report, there has been extensive work developing syntheses for Pt NPs with a variety of surface structures.[2] Consequently, efficient catalysts have been discovered that contain even higher concentrations of edges and corners,[10] or have surfaces containing high Miller index facets, such as (731), which naturally contain a large concentration of high energy step edge atoms.[8]

Ribonucleic acid (RNA) was chosen as the potential surface structure controlling capping ligand for this study. RNA is an interesting biomolecule because of its ability to reproducibly fold into secondary structures, which have been used to recognize and bind with specificity to the surface structure of proteins.[11] Therefore, it has been hypothesized that the proven ability for RNA to recognize protein surfaces based on its secondary structure suggests that RNA also has the ability to recognize the surface of inorganic materials.[11-13] In fact, RNA has been used previously in several studies to mediate the synthesis of inorganic nanoparticles.[11-17] In some cases, RNA has been shown to mediate the formation of palladium nanoparticles with specific shapes encapsulated by a single facet, such as hexagons or cubes.[12, 13] An additional benefit of

utilizing RNA, as described in Chapter 1, is the ability to do an *in vitro* biomolecule selection to isolate functionally specific RNA sequences.

Presented in this chapter is the development of a method for identifying capping ligands capable of mediating the synthesis of Pt NPs with a desired facet on their surfaces. Since the surface facet helps to dictate the shape of the Pt NP, the capping ligands were thereby able to control the Pt NP shape. Surface structure controlling capping ligands were identified utilizing *in vitro* selection to isolate RNA sequences that preferentially bound to specific Pt facets. Pt single crystals cut and polished to expose a single Pt facet of the desired (*hkl*), were used to provide the selection pressure. The selected RNA was then used as the capping ligand in a NP synthesis, operating in the scheme presented in Figure 4.2. The mechanism is based on the "selective adhesion" concept. In that mechanism, the RNA preferentially binds the (*hkl*) of interest as the NPs grow, arresting further growth on those faces and promoting growth on the other, undesired faces (*h'k'l'*). Consequently, the product NPs of that process exhibit an enrichment in selected (*hkl*) facets. In the following sections, two separate RNA selections are described with the goal of identifying RNA sequences able to bind the low energy (111) and

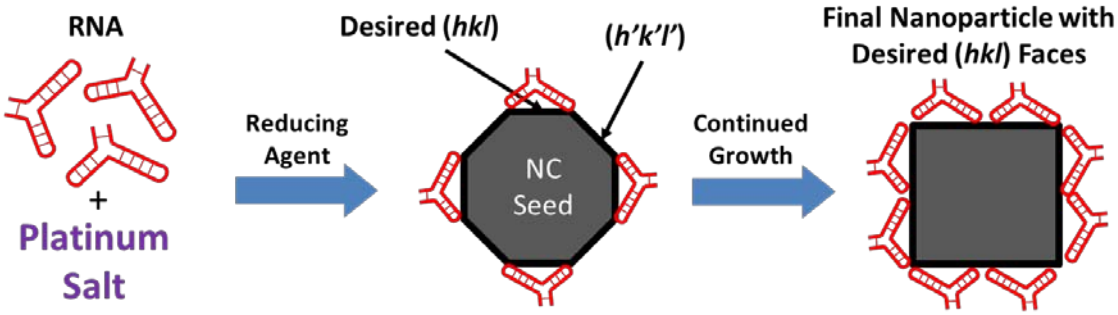

Figure 4.2. A reaction scheme demonstrating the use of RNA molecules to control the growth of nanoparticles. Upon the introduction of a reducing agent to a solution of RNA sequences selected to bind (*hkl*), those sequences bind (*hkl*) faces as they form leaving (*h'k'l'*) exposed. Additional monomers add to the exposed undesired facets resulting in a nanoparticle capped in the desired facet.

(100) facets of platinum. The results of the first selection indicated that it was not successful at isolating RNA capable of binding Pt surfaces in a facet specific manner. Therefore, a second selection was performed in which a counter selection step was added in an attempt to isolate RNA sequences that bound Pt in a more facet specific fashion. The isolated sequences were used successfully to mediate the synthesis of Pt NPs, showing statistically significant increases in the selected facet.

4.2 Selection #1.Results and Discussion

4.2.1 Selection of RNA to Bind Pt(111) and Pt(100). The *in vitro* selection of RNA sequences capable of binding specific facets of platinum was performed using two platinum single crystals. One was cut to expose the (100) facet of Pt and the other was cut to expose the (111) facet of Pt (Figure 4.3A&B). A reactor was designed and built in order to expose solutions of RNA to the surfaces of the crystal (Figure 4.3C). The reactor was comprised of two hard plastic plates used to clamp a Teflon spacer down on the surface of the crystal, creating a water tight seal. Holes of varying diamaters (2 mm, 1 mm, 0.5 mm) were cut in the bottom of the Teflon spacer, giving the capability to expose RNA solutions to different surface areas of the platinum crystals (Figure 4.3D). When attached to the Pt (111) crystal, those hole sizes are equivalent to 83, 21, and 5.2 pmoles of Pt

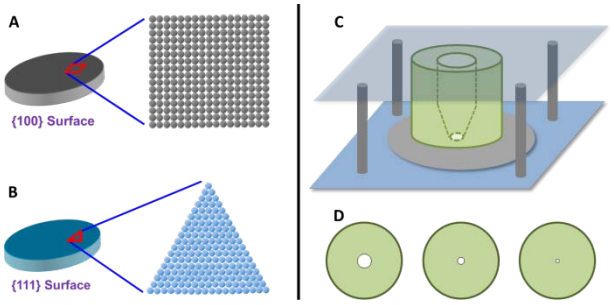

Figure 4.3. (A) Pt(100) crystal with one arrangement of surface atoms and (B) the Pt(111) crystal with a different arrangement of surface atoms. (C) A schematic of the reactor designed to clamp a Teflon spacer to the surface of the platinum single crystal. (D) The bottom of the Teflon spacers showing the holes drilled in the bottom allowing the RNA solution to contact the surface of the platinum crystal.

atoms for the 2 mm, 1 mm, 0.5 mm holes respectively. For the Pt (100) crystal, those sizes are equivalent to 69, 17, and 4.2 pmoles of Pt atoms for the 2 mm, 1 mm, 0.5 mm holes respectively. The reactor could easily accommodate 200 µL of RNA solution along with a small magnetic stir bar, allowing the solution to be stirred. A hole in the top plate was used to transfer solution into and out of the reactor using a pipette.

The selection procedure was developed and optimized by Dr. Alina Owczarek as part of the work presented in a chapter on RNA *in vitro* selection for materials in *NanoBiotechnology Protocols*.[18] The procedure (outlined in Figure 4.4) started with the production of an α-^{32}P labeled RNA random sequence library. The RNA sequences selected to bind the Pt(100) crystal were isolated as part of that previous study,[18] while the Pt(111) binding sequences were

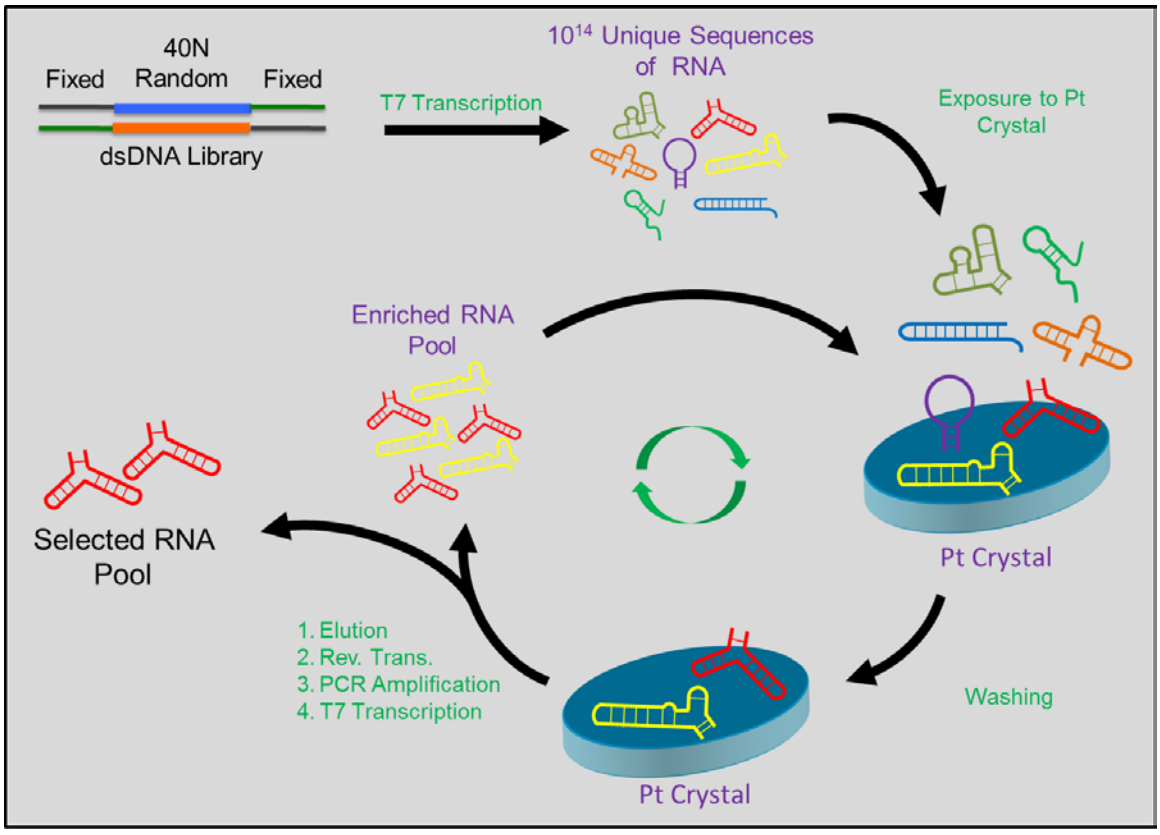

Figure 4.4. The procedure for the selection of RNA to bind the platinum crystal surface. (see text for a description of the procedure)

isolated as part of the work presented here. The selection began with an ssDNA library purchased from Integrated DNA Technologies (IDT) with sequences containing a 40 nucleotide random region capped by two fixed regions. The fixed regions act as primer regions for PCR using *Taq* DNA polymerase, allowing the conversion of the ssDNA library to a dsDNA library using PCR. The 5' primer used during this step was slightly longer than the library primer region and contained a T7 RNA polymerase promoter. Then, T7 RNA polymerase was used to transcribe the DNA into RNA, and the 40 nucleotide random region resulted in 10^{14} unique sequences being present in 1 nmol of the RNA product. The transcription reaction was spiked with α-^{32}P labeled adenosine triphosphate (ATP) so that the β-particle emissions could be detected and used to quantitate the RNA throughout the selection procedure.

Following the outline in Figure 4.4, the RNA pool was exposed to the Pt single crystal using the reactor shown in Figure 4.3. The RNA was dissolved in a 4-(2-hydroxyethyl)-1-piperazine-ethanesulfonic acid (HEPES) buffer at pH 7.2 (20 mM HEPES, 30 mM NaCl, 5 mM $MgCl_2$) and added to the reactor attached to the crystal. After stirring for 3 hours, the solution containing the unbound RNA was removed, leaving some RNA bound to the crystal surface. The reactor was washed three times with fresh buffer to remove all of the loosely bound RNA, and then the strongly bound RNA was eluted with formamide at elevated temperature (70 °C). The eluted RNA was reverse transcribed into cDNA using Super Script III reverse transcriptase, and then amplified as dsDNA by PCR. Since the Taq enzyme has an error rate of about 1 in 9000 bases, it introduces mutations during the amplification process, adding an evolutionary aspect to the *in vitro* selection.[19] The amplified DNA was then used in the next round of the selection using the same procedure. The selection procedure was repeated for 10 total rounds. Figure

4.5 shows the percent of the original RNA pool that was recovered during the elution step. After rounds 4 and 7 the Pt surface area was changed by swapping out the Teflon spacer from 2 mm to 1 mm and then from 1 mm to 0.5 mm, respectively. This was done to increase the selection pressure by reducing the surface area of platinum available for the RNA to bind.[18] A lower percentage of the starting RNA pool was passed to the next round thereby selecting the highest affinity binders. The benchmark used to decide when to change the size of the hole in the Teflon spacer was after three rounds of increasing RNA recovery. As shown in Figure 4.5, the percent recovery from round to round increased as expected (with the exception of round 3) and decreased when the amount of available platinum surface area was reduced.

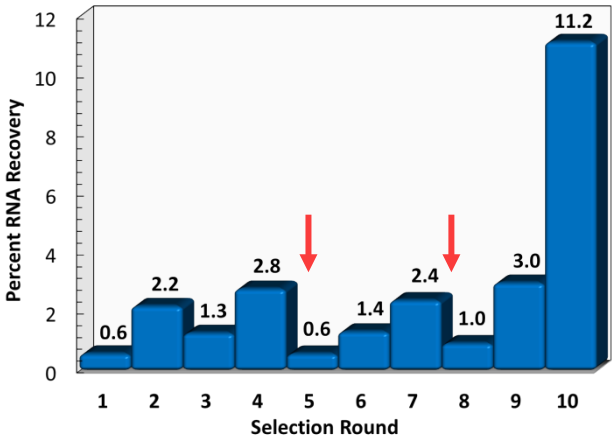

Figure 4.5. The percent of the starting RNA pool recovered at the end of each round of the selection. Red arrows indicate when the challenge was increased by reducing the size of the hole in the Teflon spacer thus reducing the concentration of platinum available.

4.2.2 Synthesis of Nanocrystals with Pt(100) Selected RNA Sequences. The RNA sequences selected for the Pt(100) facet by Dr. Owczarek were evaluated as capping ligands in a Pt NP synthesis. The synthesis of NPs was performed using hydrogen as the reducing agent and the procedure was similar to the one described previously in the literature.[9, 20] The platinum salt used in this reaction was K_2PtCl_4, which required that a 10 mM solution be made in water three days prior to the synthesis. This aging step allowed the K_2PtCl_4 to hydrolyze to the $PtCl_2(H_2O)_2$ complex, which is easier to reduce than $PtCl_4^{2-}$ and makes the reduction kinetics better for colloidal synthesis.[21] The

synthesis procedure combined the 3 day aged K_2PtCl_4 solution (final 0.5 mM) with the capping ligand, and then the solution was purged of oxygen by bubbling a stream of argon through it for 10 minutes. Hydrogen gas (the reducing agent) was bubbled through the reaction for 5 minutes, and then the vial was immediately sealed from the ambient atmosphere to trap the hydrogen gas. The reaction was agitated overnight (typically ~18 h) at 20 °C. This procedure was chosen because it kept the amount of added salts to a minimum, thus reducing the chance of interference with the folding of the RNA. Additionally, this method has been used in the past to produce (100) capped cubic and (111) capped tetrahedral Pt NPs, using the polymer sodium polyacrylate.[9]

It was quickly discovered that the presence of the buffer and salts used in the selection procedure (20 mM HEPES, 30 mM NaCl, 5 mM $MgCl_2$) interfered with the synthesis of NPs. The TEM image in Figure 4.6A shows that when the synthesis was run using the buffer along with a random pool of RNA and K_2PtCl_4, NP aggregates were formed. When the random pool RNA was used without the buffer, the NPs were comprised of more defined shapes, and were well dispersed (Figure 4.6B). The NP solutions were also visibly different. The reaction product with buffer was noticeably aggregated and dark grey in color. Without buffer, the reactions remained clear and turned a golden brown color as has been reported previously for Pt colloids.[9] Therefore, the Pt(100) selected RNA was tested in reactions that did not contain the HEPES buffer or the salts.

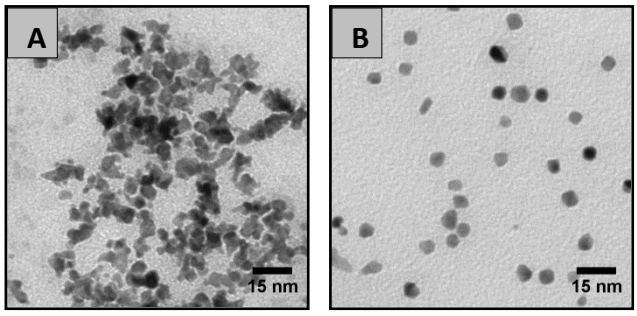

Figure 4.6. TEM images of the Pt NPs made by the reduction of K_2PtCl_4 with hydrogen gas in the presence of Random RNA (A) with the buffer and salts present and (B) with no buffer or salts.

The hypothesis was that the selected RNA sequences would produce more cubic shaped NPs, because that shape is predominantly capped by (100) facets.[2, 9] Consequently, the success of the selection could be determined by percentage of cubes found in the product. The percentage of cubes for the random pool of RNA sequences, the Pt(100) selected pool, and a single sequence designated #48 was determined. The single sequence had been found to bind with a statistically significant higher binding coefficient to the Pt single crystal's surface than the random pool.[18] It was found that both the NPs made with the selected pool and with sequence #48 contained more cubes than the NPs made with the random RNA (Figure 4.7). This result was intriguing, but there were concerns that the result could attributed to properties other than facet specific binding. The reasoning being that the RNA was not in the original buffer solution in the Pt NP synthesis. Since RNA secondary structure relies on the concentration of ionic species in the solution,[22, 23] the RNA was likely folded differently under Pt NP synthesis conditions. Therefore, this data does not support the hypothesis that RNA secondary structure is important for recognizing and binding to a material's specific surface structure.

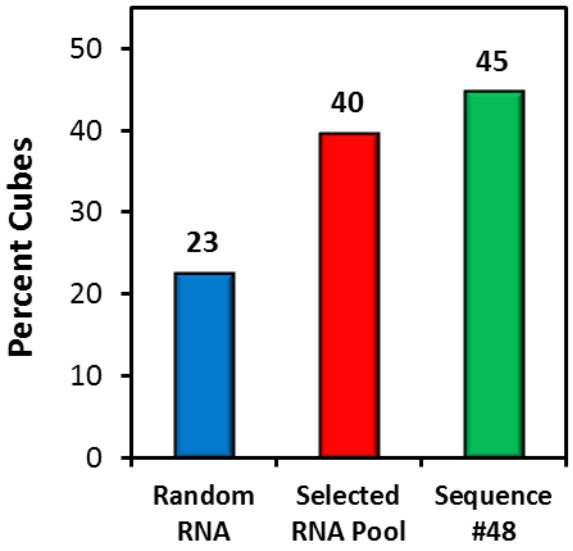

Figure 4.7. The percentage of cubes in the Pt NP product made with three different pools of RNA: the random pool, the Pt(100) selected pool, and Pt(100) selection single sequence #48.

4.2.3 Synthesis of Nanocrystals with Pt(111) Selected RNA. Subsequent Pt NP syntheses were then conducted with the RNA sequences selected to bind the Pt(111) facet.

For these experiments, it was found that addition of HEPES buffer without the salts could be used. The TEM image in Figure 4.8A shows that the NPs look similar to the NPs prepared without buffer. No shape enrichment was observed as part of the Pt NP syntheses using the Pt(111) selected RNA sequences, but there was an informative result demonstrating size control using three single sequences of RNA isolated from the selection. The HEPES only control Pt NPs were compared to Pt NPs made with three single sequences of selected RNA. Images of the Pt NPs with size histograms representing measurements of the NPs at their widest dimension through their center are presented in Figure 4.8. The selected RNA sequences produced Pt NPs of three different size distributions all of which have sizes that are smaller than the no RNA/HEPES only control. Interestingly, sequence B55 produced NPs with two distinct size distributions, based on the histograms. While these data do not confirm the ability for facet control, they do demonstrate that different sequences of RNA were capable of affecting this synthesis in different ways. It should also be noted that the HEPES only control sample contained well-

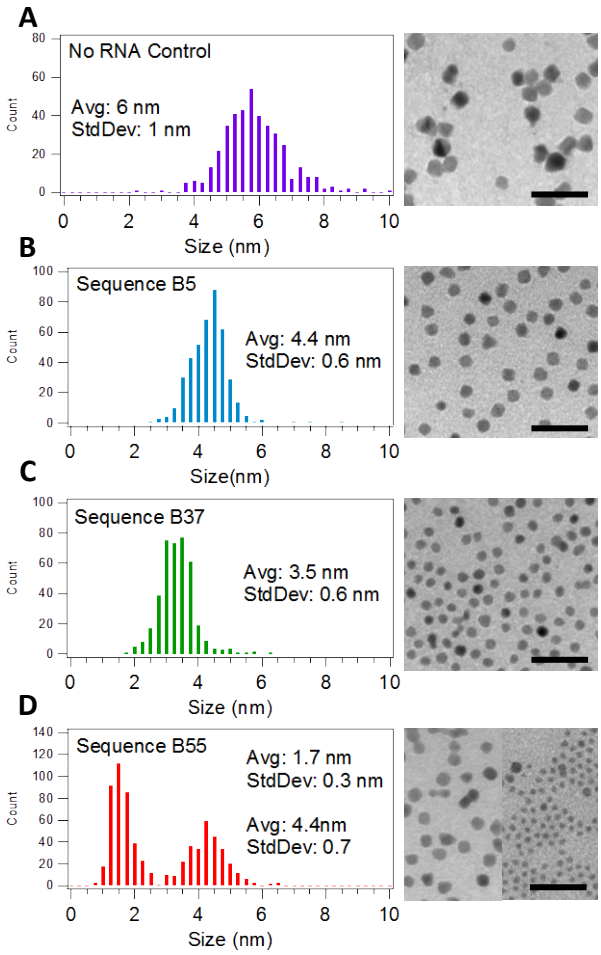

Figure 4.8. Size distribution histograms and TEM images of the Pt NPs made in HEPES only buffer without the presence of the salts. (A) HEPES only, (B) Pt(111) sequence #B5, (C) Pt(111) sequence #B37, and (D) Pt(111) sequence #B55. (Scale bars = 20 nm)

dispersed nanoparticles, suggesting that HEPES was able to function as a capping agent for the Pt NPs.

4.2.4 Binding of Selected RNA to Pt Crystals. The binding constants to the Pt(100) crystal for the RNA from the Pt(100) selection were determined previously.[18] A particular sequence from that selection, #26, had a statistically significant, higher binding affinity to the crystal than the random RNA pool. The K_{ads} was found to be approximately 10 times higher than the starting random sequence RNA pool.[18] A similar experiment was conducted as part of the work presented here in order to compare the binding affinities of the random and selected sequences of RNA to both the Pt(100) and Pt(111) crystals. This was done to determine if the selected RNA had a higher binding affinity towards platinum but to also determine if the

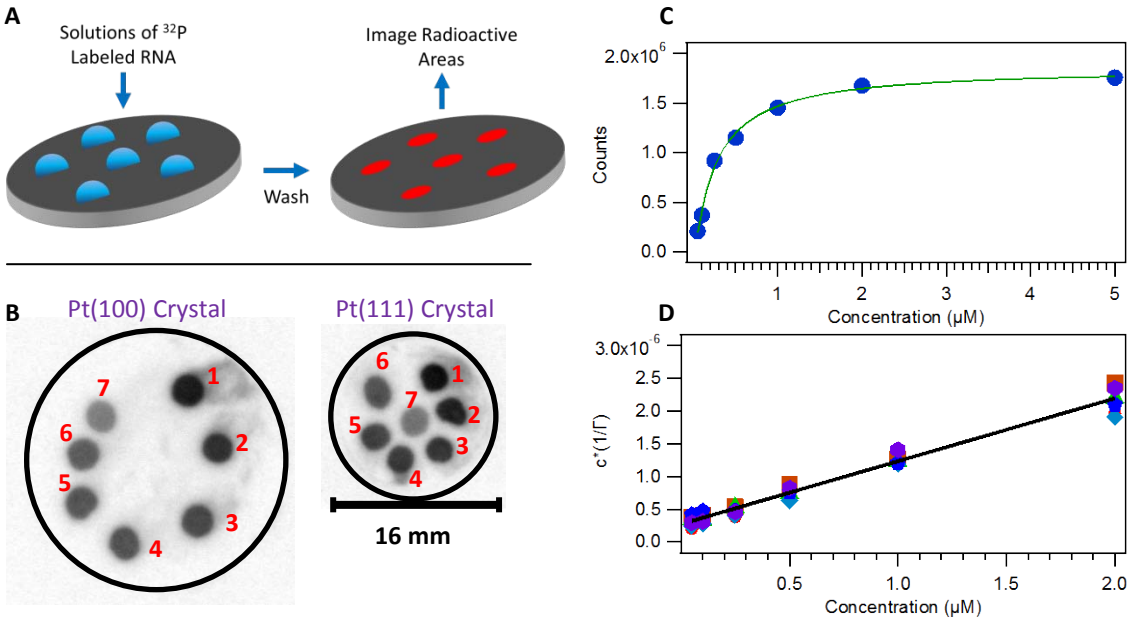

Figure 4.9. (A) A schematic for the binding study procedure where drops of ^{32}P labeled RNA solutions are exposed to the surface of the platinum crystal and then imaged with the phosphor imager. (B) Example data from the phosphor imager for spots with decreasing concentration of RNA from spot 1 (5 μM) to 7 (0.2 μM). (C) an example of the adsorption isotherm using the quantitative data. (D) A linear plot used to determine the K_{ads} (see text).

binding affinity was facet specific. The experiment involved placing 2 µL drops of a series of concentrations of ^{32}P labeled RNA on the surface of the Pt crystal, as shown Figure 4.9A. The crystal was then stored for 1 hour in a petri dish containing a wet filter paper to keep the humidity high and prevent evaporation of the droplets. After 1 hour, the surface of the crystal was rinsed with water, and the RNA bound to the surface was measured using a phosphor imager. The spots were quantified using the software associated with the imager, and example data are presented in Figure 4.9B. As the concentration of RNA was increased, the amount of RNA adsorbed to the surface increased, eventually reaching a saturation point. An example plot of the quantitative data is presented in Figure 4.9C. The data was measured relative to the "saturated" point by dividing the number of counts for each concentration point by the counts for the maximum concentration. The data was then fit to a linear plot using the equation for a Langmuir isotherm equation:

Equation 4.1[18]

$$\frac{c}{\Gamma} = \frac{c}{\Gamma_{max}} + \frac{1}{K_{ads} \cdot \Gamma_{max}} \quad where: \Gamma = \frac{[counts]_c}{[counts]_{csat}}$$

where, c = the RNA concentration in M, Γ = a ratio of the counts measured at each point to the saturated counts, K_{ads} = the equilibrium adsorptions constant, and Γ_{max} = the maximum adsorption, which in this case should be close to 1. Plotting 1/(c*1/Γ) versus c gave a linear plot with a slope of $1/\Gamma_{max}$ and an intercept of $1/(K_{ads}*\Gamma_{max})$ (Figure 4.9D is an example of such a plot).[24] The data obtained for these experiments are presented in Table 4.1 and are on the same order of magnitude as the data collected previously.[18] The experimentally derived K_{ads} for all three of the selected sequences tested had a statistically significant higher value when evaluated by the student's T-test at the 95% confidence level. However, none of the sequences

had a higher affinity for one crystal over the other when evaluated by the student's T-test at the 95% confidence level. Therefore, it was concluded that none of the sequences were specifically selected to bind one crystal over the other. It appears that the selections identified RNA sequences that were good Pt binders, indiscriminant of facet.

Table 4.1. Adsorption equilibrium constants for single sequences of RNA isolated from two selections on two different Pt crystal facets compared to a random pool of RNA. The constants were determined in the selection buffer. (K_{ads} in M^{-1})

RNA Seq.	K_{ads} Pt(111)	K_{ads} Pt(100)
Random RNA	**2.3** (± 0.9) x10^6	**2.1** (± 0.9) x10^6
Pt(100) #48	**5** (± 1) x10^6	**5** (± 2) x10^6
Pt(100) #26	**9** (± 2) x10^6	**11** (± 6) x10^6
Pt(111) #37	**3.8** (± 0.7) x10^6	**3.7** (± 0.9) x10^6

4.2.5 Conclusions of the First Selection. The results of the binding experiments led to the decision to stop work on the RNA sequences isolated as part of this selection and use the data collected to design a new selection that could isolate RNA with more facet specificity. Additionally, the selection was run in a buffer that was incompatible with the Pt NP synthesis, causing the Pt NP synthesis to be run in pure water or with HEPES only as the buffer. In these cases, it was unlikely that the RNA was in the same secondary structure, which was in conflict with the hypothesis that the secondary structure of the RNA was important.[25, 26] Also, when HEPES was added to the Pt NP reaction, it was capable of capping the NPs, which could have led to interference in the binding of the RNA during the synthesis. The sum of these observations led to the conduction of a second RNA *in vitro* selection for facet specific Pt binding sequences in a buffer that was compatible with the Pt NP synthesis.

4.3 Selection #2. Results and Discussion

Based on the results of the first selection, a new selection was conducted with the intention of matching the selection conditions with the Pt NP synthesis conditions and

improving the facet specificity of the selected RNA. First, a new buffer was identified that was compatible with the Pt NP synthesis and the RNA. The new buffer allowed for the same buffer conditions to be used in both the selection and the synthesis of Pt NPs, increasing the likelihood that the RNA would have the same secondary structure in both instances.[25, 26] In order to improve facet specificity of the selected RNA, a counter selection step was added to remove sequences that bound non-specifically to platinum or specifically to the wrong platinum facet. The hypothesis was that these changes to the selection procedure would improve the ability to select RNA sequences capable of binding a specific facet of Pt, and then those RNA sequences would mediate the synthesis of Pt NPs with an enriched abundance of the selected facet.

4.3.1 Identification of Improved Buffer. Two other RNA compatible buffers, potassium phosphate and tris(hydroxymethyl)aminomethane hydrochloride (Tris-Cl), were tested and compared to the original buffer HEPES. First, the buffers were tested for their ability to maintain the pH of the solution during the reduction of K_2PtCl_4 by hydrogen gas. The starting pH of the buffers was 7.2 and the final buffer concentration was 20 mM. Both Tris-Cl and potassium phosphate maintained the pH closer to the starting pH 7.2 than the original HEPES buffer and prevented the pH drop to ~3 observed in the absence of buffer (Table 4.2). The stability of the RNA was also tested in the phosphate and Tris-Cl buffers. A 1 μM solution of RNA in a 20 mM solution of the buffer was allowed to sit on the bench at room temperature for 24 hours. To check for degradation, the RNA was analyzed with polyacrylamide gel electrophoresis before and

Table 4.2. pH values for solutions of Pt after the reduction of K_2PtCl_4 with hydrogen gas. The starting pH was 7.2.

Buffer	pH after the reaction
Un-buffered	3.2
20 mM HEPES	6.0-6.5
20mM TRIS	6.5-7.0
20mM K Phosphate	6.5-7.0

after the stability test. No change was observed in the RNA molecular weight after sitting for 24 hours, showing that the RNA was stable in both of the buffers overnight.

The buffers were also tested for their compatibility with the synthesis of Pt NPs. The test was run with and without random RNA sequences present in the buffers Tris-Cl and potassium phosphate at pH 7.2. The results of the Pt NP synthesis are shown in Figure 4.10A-D. The Tris-Cl seemed to cap the particles in a similar fashion as HEPES, discussed in the previous section. The Pt NP product, when random RNA was present along with Tris-Cl, was irregularly shaped particles that appeared to be aggregated. The phosphate buffer (Figure 4.10C&D) appeared to be the superior buffer for NP synthesis, because in the absence of RNA, only large aggregates of Pt were observed. This implied that the phosphate ions were not good at capping the Pt and arresting their growth. However, when the random RNA sequences were present with the phosphate buffer in the synthesis, well dispersed more regularly shaped NPs formed. The NPs were distributed among the different shapes shown in Figure 4.10E. Most of the NPs were in the

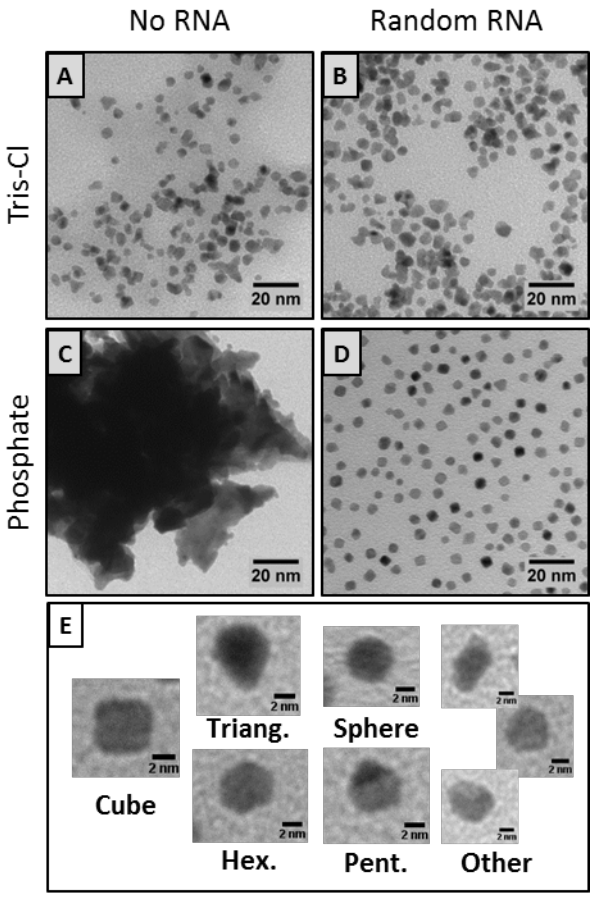

Figure 4.10. TEM images of the Pt NPs produced from the hydrogen reduction of K_2PtCl_4 using the Tris-Cl buffer (A, B) and the phosphate buffer (C, D) without RNA (A, C) and with random pool RNA (B, D). (E) Typical shapes seen in the synthesis using the phosphate buffer and random pool RNA.

category “other,” but appeared to contain well-defined facets, judging by the sharp angles around their edges. Based on the pH tests and the NP synthesis tests, the 20 mM phosphate buffer at pH 7.2 was chosen to as the buffer most compatible with the NP synthesis.

In order to get a baseline on the binding affinity of random RNA to the Pt(111) and Pt(100) Pt crystals, a binding experiment similar to the one described in Figure 4.9 was conducted. A qualitative experiment was done comparing the random pool of RNA in the HEPES/salts buffer from the previous selection and the new buffer, 20 mM potassium phosphate. The result was a striking difference in the binding affinity of the random pool of RNA in the two buffers. The RNA in the phosphate buffer bound with a much lower affinity than when the HEPES buffer was used. This is apparent in the data shown in Figure 4.11, where several spots of the same concentration of RNA were placed at various spots on the crystal, allowed to sit for one hour, and then washed away. A lower binding affinity of the random RNA was viewed as a positive result, because it would present the opportunity to isolate specific Pt binding RNA sequences that had a much higher affinity than the random pool. This is in contrast to the previous selection where the random pool of RNA sequences already had a high binding affinity.

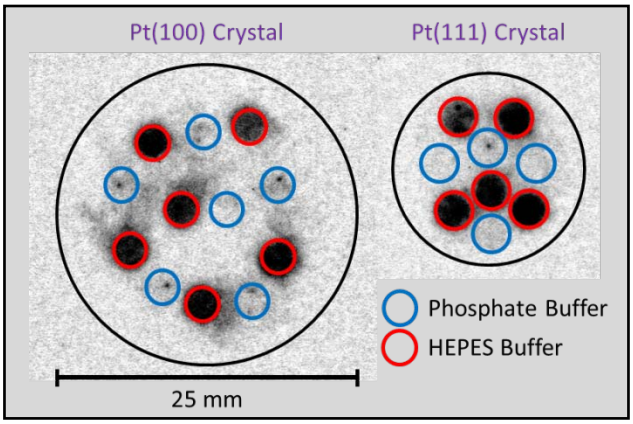

Figure 4.11. Phosphor images of the platinum crystals exposed to spots containing 1 µM random pool RNA in two different buffers, Phosphate and HEPES at 20 mM.

4.3.2 Selection of RNA to Bind Pt(111) and Pt(100) Facets. A second RNA *in vitro* selection was performed starting with a random pool of ~10^{14} different RNA sequences. Two selections were performed

side by side for each of the Pt crystal facets, (100) and (111). The procedure was similar to the one described in Figure 4.4 with a few modifications. First, the buffer was 20 mM potassium phosphate pH 7.2, with no other salts such as NaCl or $MgCl_2$, and was used throughout the selection. The second modification was added to improve the facet specificity of the selected RNA. During the selection step of each round, the RNA was exposed to both the Pt(111) and Pt(100) crystals in a procedure that included a counter selection step (as illustrated for the Pt(100) selection in Figure 4.12). The counter selection step involved first exposing the RNA pool to the crystal of the non-desired facet. For example, in the Pt(100) selection the RNA was exposed to the Pt(111) crystal. Then, the RNA still in solution was removed via pipette and transferred to the reactor containing the Pt crystal with the desired facet exposed. The

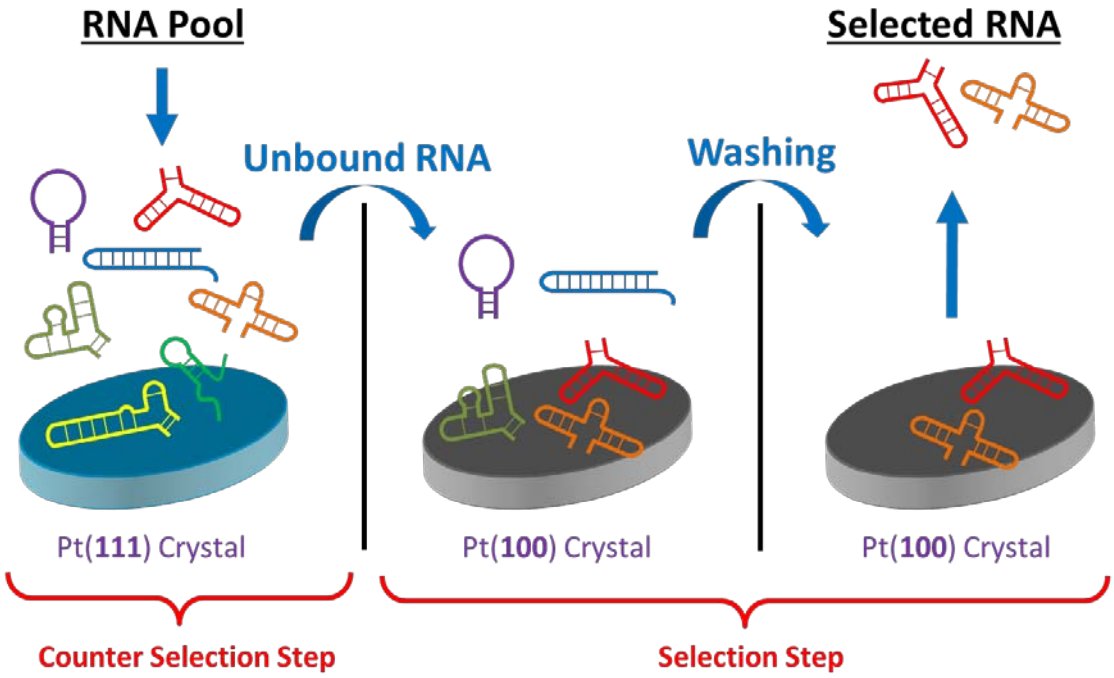

Figure 4.12. A schematic demonstrating the counter selection step added to the second selection where the RNA pool is first exposed to the platinum crystal of the non-desired desired facet to remove all non-specific binders. Then the selection is carried on as in Figure 4.

procedure was continued as was described for the first selection. The counter selection step was meant to remove all good Pt binders that were either non-facet specific or bound specifically to the non-desired facet. That step would also remove any RNA sequences that bound to the Teflon piece of the reactor. The range of sizes of the holes in the Teflon spacer was also changed for this selection. The 0.5 mm piece was replaced with a new 4 mm size piece that exposed the solution in the reaction to 330 pmol of Pt atoms on the Pt(111) crystal and 270 pmol on the Pt(100) crystal.

The selection was run for 12 rounds, and the percent of the starting pool of RNA recovered after each round is shown in Figure 4.13. During the counter selection step for both the Pt (111) and Pt(100) selections, the platinum area was kept as large as possible by using the Teflon spacer with the 4 mm hole throughout the 12 rounds. The platinum surface area exposed to the RNA solution was not increased beyond 4 mm due to the presumed ability of all RNA sequences to bind Pt with some affinity. Consequently, if the platinum area was increased, then there would be a continually higher chance that active sequences could start to be removed during the counter selection step. During the selection step for both the Pt(111) and

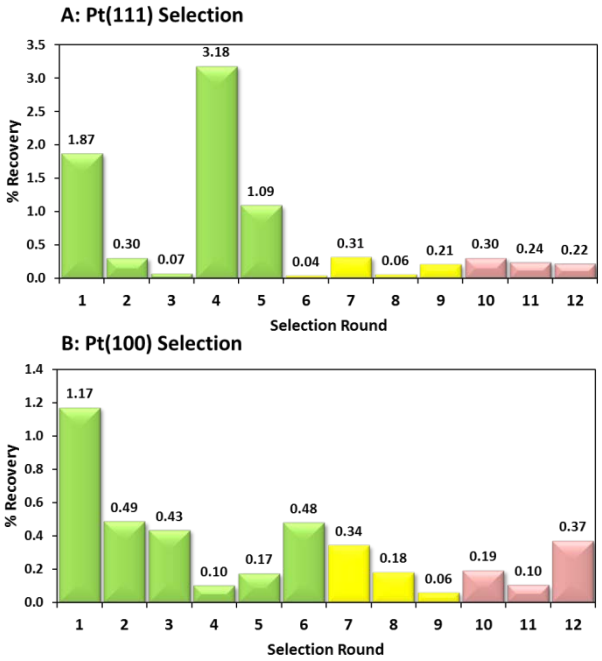

Figure 4.13. The percent of the starting pool recovered after each round for the Pt(111) (A) and the Pt(100) (B) selections. The size of the hole in the Teflon spacer during the selection step is indicated by the color of the bar: (green) 4 mm; (yellow) 2 mm; (red) 1 mm.

Pt(100) selections, the platinum area the RNA solution was exposed to was decreased, thus increasing the selection pressure as described in the previous section for Selection #1.[18] The same benchmark was used to decide when to decrease the size of the hole in the Teflon spacer as was used for Selection #1. That benchmark was to decrease the hole size after three rounds of increasing RNA recovery. For the Pt(111) selection, the Teflon piece was changed after round 5 from 4 mm to 2 mm and after round 9 from 2 mm to 1 mm. The percent RNA recovery for each round of the Pt(111) selection is presented in Figure 4.13A. For the Pt(100) selection the first reduction in hole size was made after round 6 and the second after round 9. The percent of RNA recovery is presented in Figure 4.13B. Unlike Selection #1, the percent recovery did not follow the pattern of continually increasing after each round until the hole size was reduced. That deviation from the expected percent RNA recovery pattern is likely due to one or both of the changes made to the Selection #2 procedure. Without further evidence, it would be difficult to ascertain what role the counter selection step or the new buffer may have played in causing the percent recovery variability.

A portion of the RNA pool isolated by the selection was cloned and sequenced to determine if the RNA sequences could be grouped into families containing conserved regions of nucleotide base order. The RNA sequences were entered into the software program, Daughter of Sequence Alignment (DOSA), from which several families of sequences were identified. Those families found in the pools isolated from both selections are shown in Figure 4.14. They were determined by searching for 8 nucleotide long conserved regions with an 85% match. The ability to identify families like the ones in Figure 4.14, is a strong indication that the selected RNA sequences were evolved to exhibit a specific function.[13] Further testing was required,

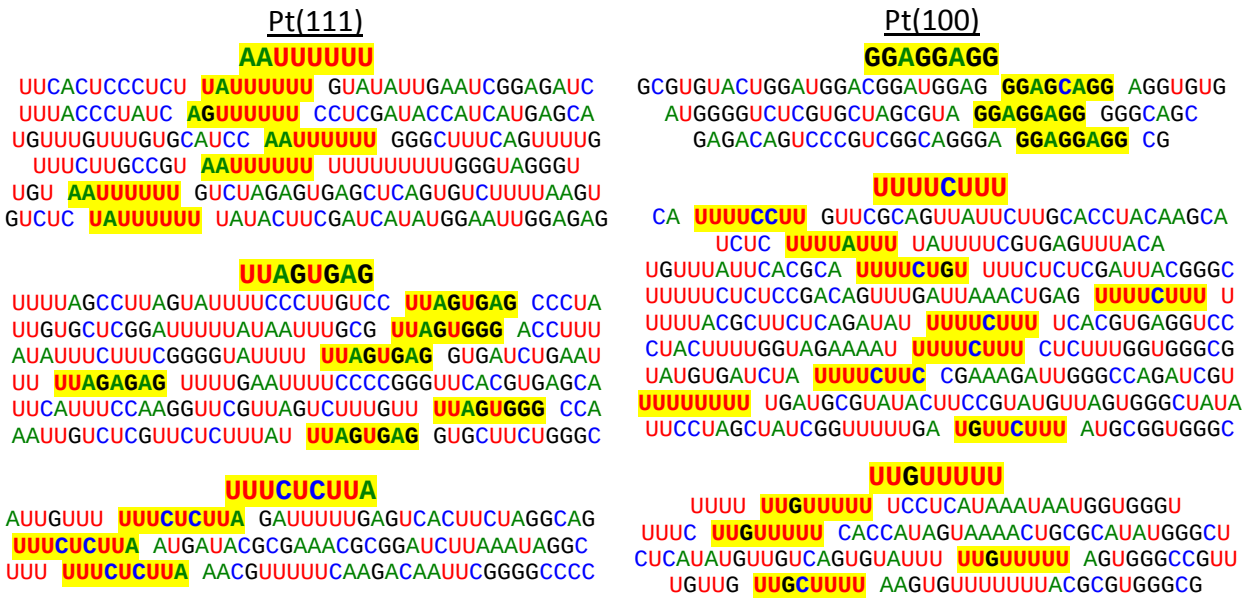

Figure 4.14. The families of RNA sequences found by the DOSA analysis for RNA isolated as part of the Pt(111) and Pt(100) selections.

however, to confirm that the selected RNA sequences had the ability to bind the Pt crystals in a facet specific fashion.

4.3.3 Binding of Selected RNA to Pt Crystals. Qualitative binding experiments like the one in Figure 4.11 were conducted on the selected pools of RNA sequences. The selected pools were compared relative to the original random pool and relative to each other. The studies were done on both crystals simultaneously, so that the relative binding affinities could be compared between the two crystals. The RNA isolated as part of both selections had a higher binding affinity towards the platinum crystals than the random pool. This was true for all of the RNA concentrations that were tested (0.25 µM, 0.5 µM, 1.0 µM, and 2.5 µM), and is evident in the data presented in Figure 4.15A&B for the experiments performed with 1.0 µM RNA. Quantitatively, the selected RNA from both selections was found to bind to both of the Pt crystals at all of the concentrations with a statistically significant, higher affinity using the

student's t-test at the 95% confidence level. However, when the spots were compared between the two crystals, a statistically significant difference was not observed, implying that the selected sequences did not specifically bind one crystal facet over the other. Additional evidence of the selected RNA pools not binding to the Pt(111) and Pt(100) facets in a specific manner came in the comparison of the two selected pools spotted in the pattern shown in Figure 4.15C. This experiment was done at 0.25 µM, 0.5 µM, and 1.0 µM RNA, and the quantitative data was compared using the student's t-test. At the 95% confidence level, neither of the selected pools were shown to bind either of the Pt cyrstals with a higher affinity. These results indicate that the selection did select RNA sequences that bind Pt with a higher affinity, but those selected sequences were not significantly facet specific.

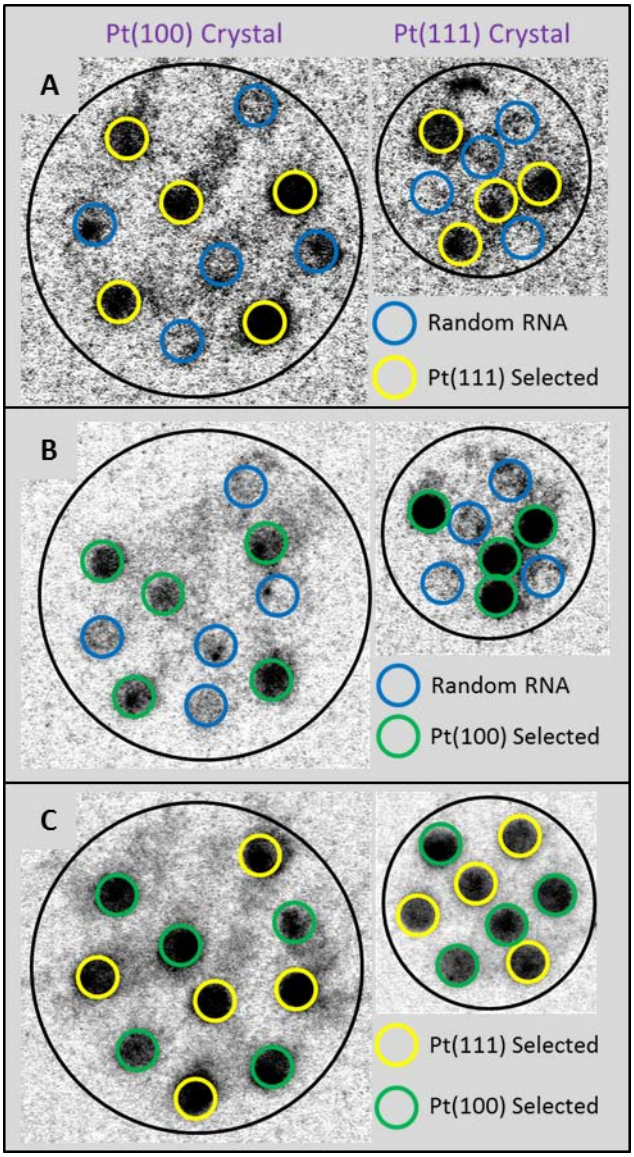

Figure 4.15. Phosphor imager data comparing the RNA pools at 1 µM on both the Pt(100) and Pt(111) crystals. (A) The random RNA compared to the Pt(111) selected RNA; (B) The random RNA compared to the Pt(100) selected RNA; (C) The Pt(111) selected RNA compared to the Pt(100) selected RNA.

4.3.4 Pt NPs Mediated by Selected RNA. Pt NPs were synthesized using RNA as the capping agent by reducing K_2PtCl_4 with hydrogen in the presence of 20 mM phosphate buffer at

pH 7.2. The shapes of the resulting NPs were counted and compared as a part of a screening of the selected sequences for activity. An evaluation of facet abundance in the product was done by comparing the shapes of the product Pt NPs. This can be done because the {100} planes of a FCC crystal intersect each other at 90° angles, and therefore, the expected shapes would be cubes. However, interpretation of the shapes resulting from intersecting {111} planes is more complicated because they intersect each other at ~70° angles. Shapes bound with (111) facets have typically been reported as tetrahedra or octahedra.[2] The selected pools and several of the selected single sequences were used to make Pt NP, and were then evaluated by counting the shapes present in the product.

The first shape enrichment comparison was conducted using the random pool, the Pt(111) selected pool, and the Pt(100) selected pool RNA sequences at 2.5 μM concentrations. The synthesis was repeated three times and shapes were counted for approximately 200 NPs from each synthesis. There was little difference in the shape distribution between the Pt NPs made with the random pool of RNA and the Pt(111) selected RNA. However, the Pt NPs made with the Pt(100) RNA did have a statistically significant higher number of cubes than the Pt NPs made with the random pool, when the two sets of data were tested with the student's t-test at the 95% confidence level. Images of the particles made in the each synthesis are in Figure 4.16A-C. A bar graph containing the shape distribution and one standard deviation error bars is presented in Figure 4.16D. The Pt(100) selection produced a positive result due to the increase in cubic Pt NPs likely bound with (100) facets, which indicated that the selected RNA was able to direct the surface structure of the nanoparticles during growth in the expected manner. The result of the Pt(111) selection was less conclusive because a shape distribution change was not

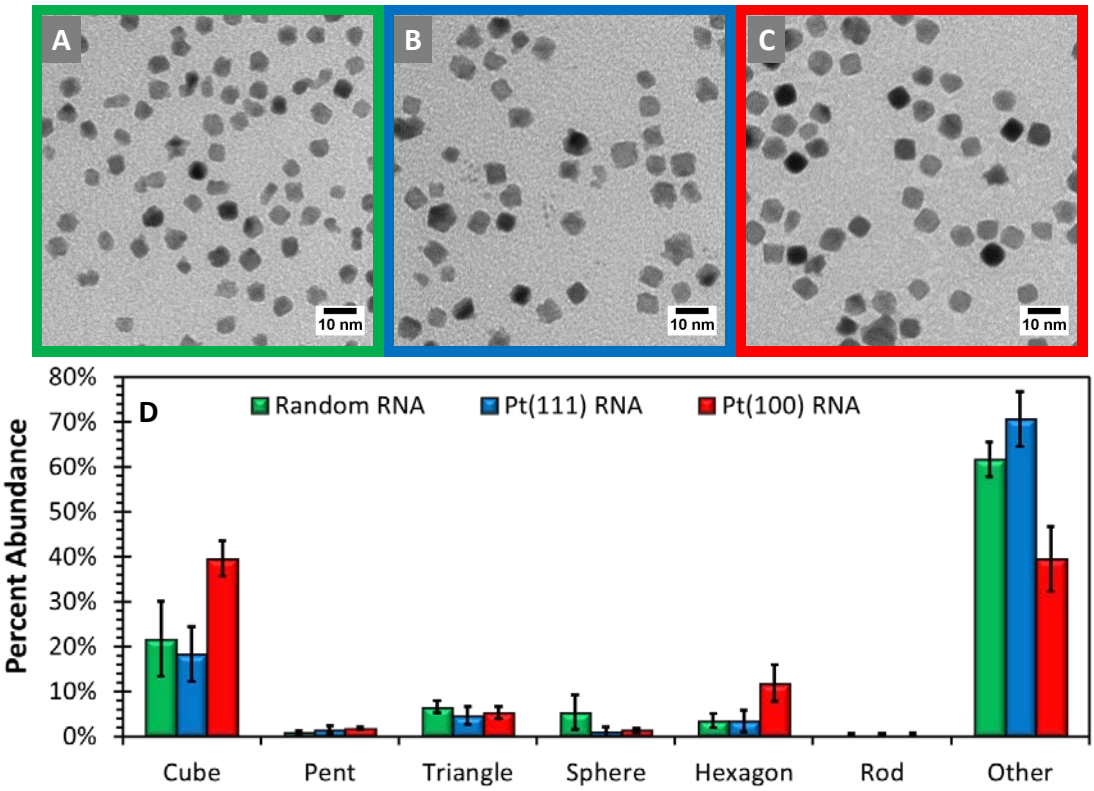

Figure 4.16. TEM images of Pt NPs made with three pools of RNA: (A) Random (B) Pt(111) selected RNA and (C) Pt (100) selected RNA. (D) The shape distribution for three separate syntheses was counted and the percent of each shape was averaged. The bars indicate the percent abundance and the error bars represent one standard deviation.

observed. However, a large portion of the NPs were in the "other" category in which the percentage of (111) facets could not be inferred.

Using the sequence families identified in Figure 4.14, 12 of the single RNA sequences from each selection were tested as Pt NP capping agents to determine if their ability to control shape was better than the selected pool of RNA. All of the sequences were tested individually in the Pt NP reaction using the same RNA concentration (2.5 µM) and reaction conditions. The RNA sequences isolated in the Pt(111) selection are identified as the 'A' group. NPs were made with two sequences from each family in Figure 4.14A and 6 orphan sequences. The sequences used are presented in Figure 4.17A and have the conserved regions from Figure 4.14

highlighted. None of the sequences showed an enrichment in any of the shapes that would be likely to be found with (111) capped particles, such as triangle, pentagon, or hexagon. Most nanoparticles were placed in the "other" category, and a couple of the sequences, A10 in particular, had an increase in the number of nanoparticles categorized as "cubes." These data are presented in Figure 4.18. The sequences isolated in the Pt(100) selection were identified as the 'B' group. Of the families in Figure 4.14B, two sequences were chosen from each of the larger families containing conserved regions with a large number of uracil bases, while one sequence chosen from the third smaller family. Seven additional orphan sequences were chosen, including one (B18) that was identical to sequence A22, except with a guanine substituted for a uracil in the 36th base. The data was evaluated by the percentage of cubes, because these sequences were selected to bind the (100) facet. None of the single sequences showed a marked increase in the number of cubes in the Pt NP product as compared to the selected pool. The percent cube abundance for each of those sequences is shown in Figure 4.19.

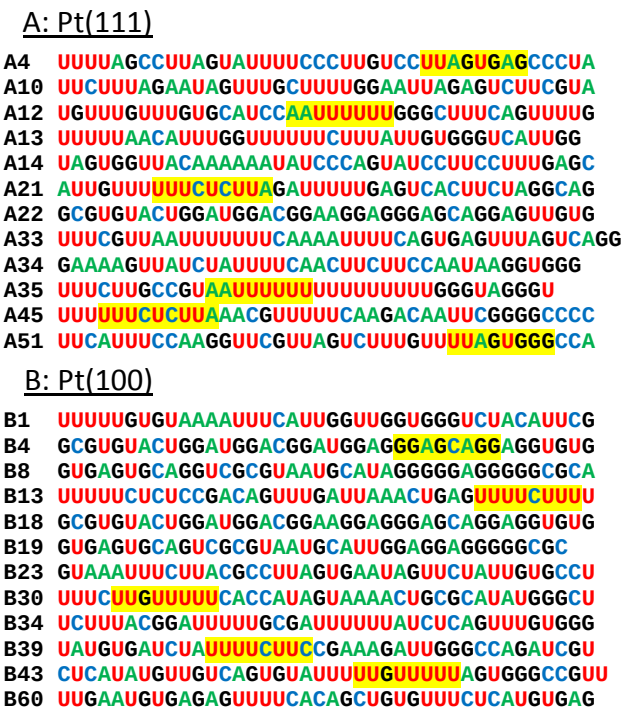

Figure 4.17. The single sequences chosen from (A) the Pt (111) selected pool and (B) the Pt(100) selected pool. Conserved regions from the sequence families in Figure 4.14 are highlighted in yellow.

4.3.5 HR-TEM Analysis. High resolution transmission electron microscopy (HR-TEM) images were used to better ascertain the abundance of the three low energy facets on the

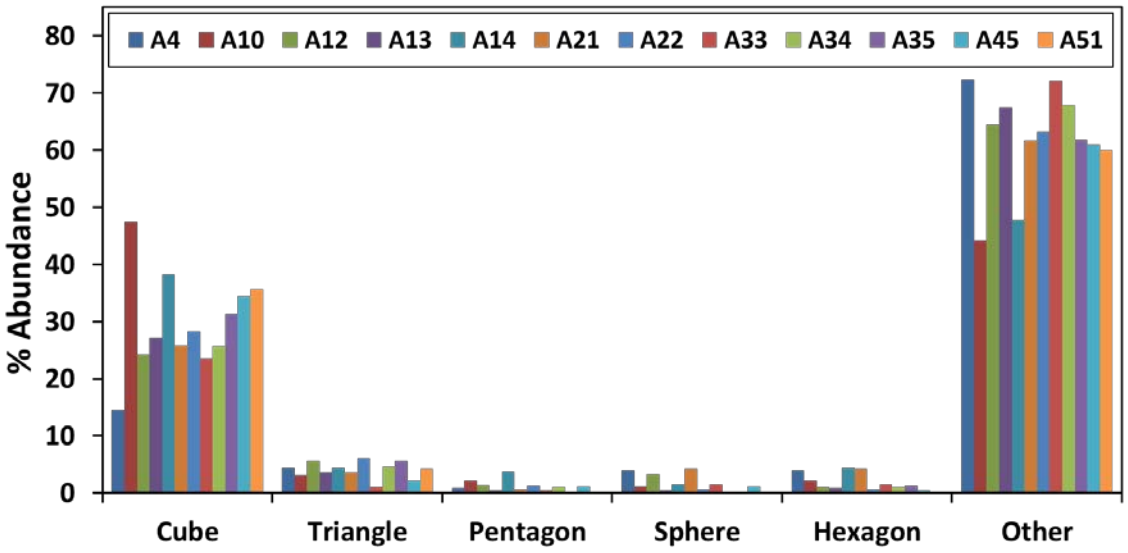

Figure 4.18. Shape distributions for Pt NPs made with the twelve single sequences from the Pt(111) selection listed in Figure 4.17A.

surfaces of the Pt NPs prepared with RNA. High resolution is defined here as images for which the lattice fringes of the Pt crystal structure are resolved. The spacing of the lattice fringes and the angles with which they intersect can be easily calculated using the equations for the FCC crystal structure and the lattice constant for Pt. Therefore, the spacing for $\{hkl\}$ can be calculated using Equation 4.2:[27]

Equation 4.2

$$d_{hkl}^2 = \frac{1}{(h^2 + k^2 + l^2) \cdot a'^2}; \; if \; a' = \frac{1}{a}$$

where h, k, and l are the three Miller indices of the set of lattice planes and a is the lattice constant. That gives the spacings for {111}, {200}, and {220} as 2.27 Å, 1.96 Å, and 1.39 Å respectively. In order to get a precise

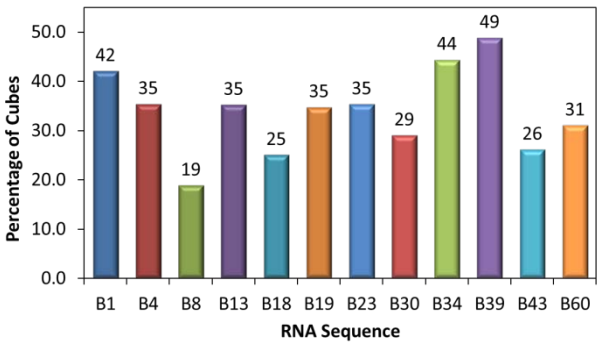

Figure 4.19. The percent abundance of cubes for the Pt NPs made with the twelve single sequences in Figure 4.17B.

measurement of the lattice spacing, a Fourier transform (FT) of the image was calculated, producing a spot pattern similar to an electron diffraction pattern. The angle and the distance of each spot from the center could then be used to determine the direction through the crystal and spacing of the lattice planes respectively. After the lattice spacings were indexed, those surface facets perpendicular to the TEM electron beam in the image were indexed based on their angle with the lattice planes. If the surface simply terminated a set of planes, the face was indexed as that facet. Alternatively, if that was not the case, the angle of the surface with respect to the set planes could be determined and compared to the angles between different lattice plane sets derived by Equation 4.3:

Equation 4.3

$$cos\phi = \frac{h \cdot h' + k \cdot k' + l \cdot l'}{\sqrt{h^2 + k^2 + l^2} \cdot \sqrt{h'^2 + k'^2 + l'^2}}$$

where $h\ k\ l$ and $h'\ k'\ l'$ are the Miller indices of two sets of lattice planes and Φ is the angle between the planes. In order to get a confident match, the angle of the surface with two separate lattice plane sets was measured. Three samples of Pt NPs made using three pools of RNA (random pool, Pt(111) selected pool, and Pt(100) selected pool) were submitted for HR-TEM imaging. Examples of particles from those three samples are presented in Figure 4.20A-C respectively. The faces of the particles have been indexed and are labeled in yellow. The FTs used to index those particles are presented below the images in Figure 4.20D-F. The faces of 10-12 particles for each sample were indexed and measured in order to gather statistics for facet abundance in the samples. More than 220 nm of edges were indexed for the particles from each sample, and the percent abundance of each low energy facet in each sample is presented in Table 4.3. Most notable in this data is the shift in the percent

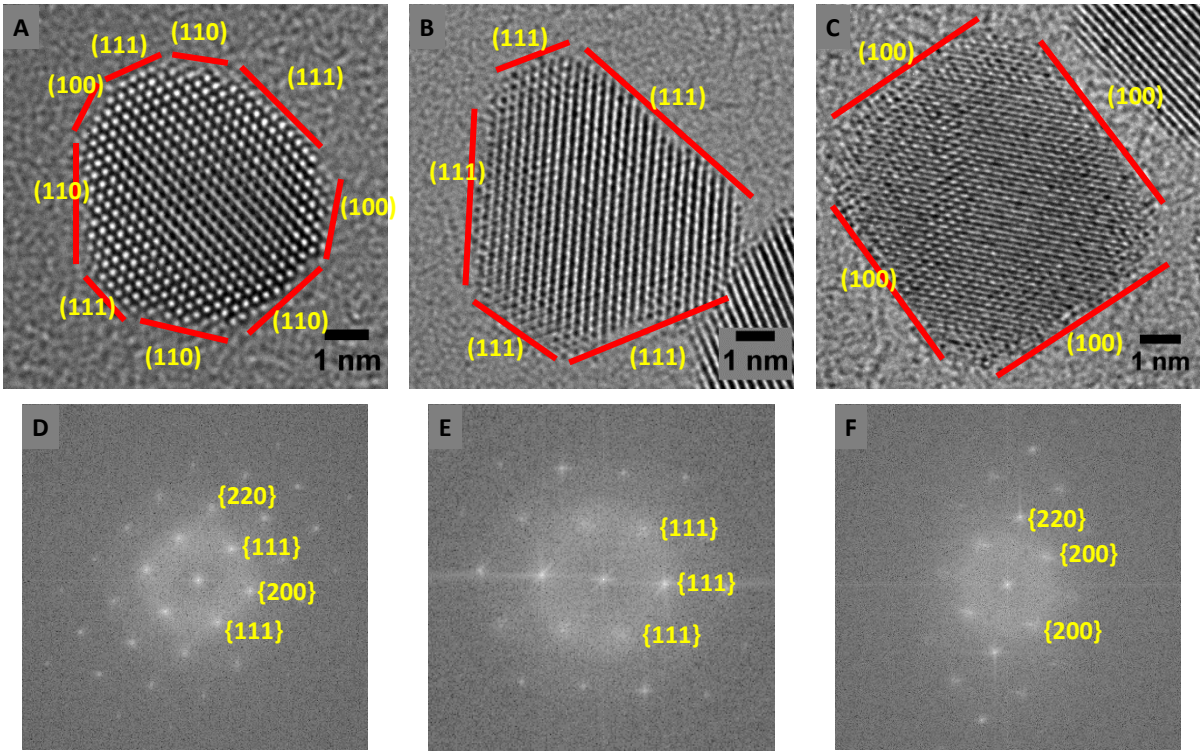

Figure 4.20. HR-TEM images for single Pt NPs from the three pools of RNA: (A) Random; (B) Pt(111) selection; (C) Pt(100) selection. The facets surrounding each particle are designated as red lines and the miller index for each facet is labeled in yellow. (D-F) Fourier transform spot patterns for the images above with the spots corresponding to sets of crystal planes labeled in yellow.

abundance of the (111) facet from 21% with the Pt NPs prepared with the random pool to 48% when the (111) selected pool was used. This result suggests that the (111) selected RNA was able to alter the facet abundance in the sample despite the lack of an obvious shift in the shape abundance.

4.3.6 Summary of Selection #2. The results presented above indicate that it is possible to isolate RNA sequences through *in vitro* selection that are able to control the surface structure of Pt NPs in a deterministic

Table 4.3. Percent abundance for each facet for the Pt NPs made with three different pools of RNA as determined by the HR-TEM data.

Sample	% (100)	% (111)	% (110)
Random RNA	63%	21%	16%
Pt(111) RNA	40%	48%	12%
Pt(100) RNA	57%	31%	12%

fashion. Pt NPs made with the Pt(111) selected pool of RNA showed an increase in the number of (111) facets despite there being no obvious difference in the resulting nanoparticle shapes. The Pt NPs made with the Pt(100) selected RNA showed a statistically significant increase in the number of cubes. Those cubes were likely to be mostly bound by (100) facets, as indicated by the HR-TEM image in Figure 4.20C and thus represent an increase in (100) faceted Pt NPs. Therefore, it can be concluded that RNA selected to bind specific facets of platinum can be used as shape controlling nanoparticle ligands. This conclusion is in spite of the evidence that there was not a statistically significant difference in the binding affinity of the RNA to the two platinum single crystal surfaces. This contradiction suggests that either the difference in binding affinity is below the resolution of the binding affinity assay or that the mechanism by which the ligands operate during the synthesis is different than the conditions under which the binding affinities were compared. In other words, the kinetics of RNA adhesion to the platinum surface may control Pt NP shape during growth. That is in contrast to the binding affinity test, which is done under thermodynamic conditions where the bound and unbound RNA in the experiment likely reaches equilibrium during the relatively long exposures of the platinum surfaces to the RNA solutions. Therefore, the experimental parameters used for the second selection may not have been optimized to select the best shape controlling sequences, which explains why 100% shape abundances were not observed.

4.4 Conclusion and Future Directions

The experiments presented in this chapter outline a method for selecting RNA sequences capable of binding specific facets of platinum. Those RNA sequences could then be used to mediate the formation of Pt NPs that had an enrichment of the selected facet on their

surfaces. Two separate selections using two sets of parameters were used in the process of selecting the RNA. The results of the first selection showed that it was possible to select RNA that could bind more tightly to a platinum surface, but the binding affinity was not specific to the facet on that surface. Furthermore, the buffer conditions used in the selection step were not compatible with the Pt NP synthesis and, consequently, altered buffer conditions were used in the synthesis. Therefore, a second selection was performed with the goal of improving on these results. A new, Pt NP synthesis compatible buffer was chosen, and a counter selection step was added during the selection process. The RNA selected to bind the Pt(111) facet increased the number of (111) facets in Pt NPs made using the RNA as determined by HR-TEM. The RNA selected to bind the (100) facet creatde a statistically significant increase in the number of (100) bound cubic Pt NPs when used as the capping ligand in their synthesis.

Despite the evidence that the RNA selection was successful at isolating RNA sequences able to control the surface structure of Pt NPs during their synthesis in deterministic fashion, there was still evidence that the RNA selection process was not completely optimized for this function. The contradictory evidence that the RNA was specific in controlling Pt NP facets while showing no resolvable specificity in the binding studies, leads to the conclusions that the two processes may be operating through different mechanisms. The hypothesis developed to explain the disparity is that the shape control in the Pt NP synthesis is a kinetic process, such that the rate of RNA binding to a facet is important. The binding study on the other hand is a thermodynamic process, where equilibrium is reached, and both the “on” and “off” rates are important. Therefore, future work in this area should be to determine if this hypothesis is correct. If it is correct, there are two possible routes for the work to take. In the first route, a

method for synthesizing Pt NPs where the shape control by the RNA ligands is under thermodynamic control should be developed. Alternatively, a new selection process should be developed that selects RNA under kinetic conditions, where the sequences that adsorb to the surfaces with the highest rate are isolated. Assuming those objectives can be accomplished, the ability to synthesize Pt NPs with an enrichment of a desired facet should be drastically improved.

If there is improvement in the effectiveness of selected RNA to control the shape during a nanoparticle synthesis, the basic research demonstrated here could be used to select RNA capable of mediating the formation of state of the art nanoparticle catalysts. When presented with a catalytically active composition and surface structure, the method would be able to isolate RNA capable of binding those catalytic surfaces. Then, the isolated RNA could be used to mediate the formation of nanoparticle catalysts with the selected active facets exposed on their surfaces. Additionally, study of the selected RNA's nucleotide base sequences and secondary structure could lead to the development of polymers capable of performing the same function. Ideally, those polymers would have similar chemical functionality as nanoparticle capping ligands but increased chemical stability, so that they could be used on an industrial scale. That achievement would complete the process of developing and producing industrially relevant nanoparticle catalysts.

4.5 Experimental

4.5.1 Reagents and materials. Two platinum single crystals were purchased from Princeton Scientific Corp, one 16 mm in diameter with the (111) surface exposed and the other 25 mm in diameter cut to expose the (100) facet. The crystals were polished to a mirror finish

with <2° accuracy and <30 nm roughness by Princeton Scientific Corp. The ssDNA random pool template (Template E) was purchased from IDT and had the sequence: 5'-G GGA GAA ATA CAA ATA GGC AGG A -(40n)-TTC GAC AGG AGG CTC ACA ACA GGC-3', where 40n is a 40 nucleotide long random region. It was diluted 10 µM. All PCR and transcription reactions, Pt NP reactions, and reagent dilutions were done with DPEC treated and certified nuclease free water. Potassium tetrachloroplatinate (K_2PtCl_4, 99.99%) and hydrogen gas (99.99+%) were purchased from sigma Aldrich. Potassium phosphate, Trizma base, and sulfuric acid were all certified ACS grade and used as received. Taq Polymerase, T7 RNA polymerase, RNAse OUT, and SuperScript III enzymes and solutions of the associated buffers, DTT, and salts were purchased from Invitrogen. dNTPs were purchased from Invitrogen and combined to make a solution with 10 mM of each base. NTPs (100 µM) were purchased from Fermentas. Radiolabeled α-^{32}P ATP (10 mCi/mL) was purchased from Perkin Elmer. Primers: All primers were ordered from IDT, dissolved to make 100 µM solutions and stored frozen. **5pE**: 5'-TAA TAC GAC TCA CTA TAG GGA GAA ATA CAA ATA GGC AGG A-3'; **3pPB2a**: 5' GCC TGT TGT GAG CCT CCT GTC GAA-3'; **5pPDASE 17#21**: 5'-TAA TAC GAC TCA CTA TAG GGA-3'

4.5.2 PCR. All PCR reactions were run in 100 µL aliquots. To start each selection the PCR reaction was run in a 96 well PCR plate in the BioRad iCycler and 1 nmol of Template E was used to start. All other PCR reactions were run in 200 µL thin wall PCR tubes in the Eppendorf Mastercycler Personal. The concentrations of each reagent are shown in Table 4.4. The PCR program was 5 min @ 95 °C; # cycles x (1 min @ 95 °C; 1 min @ 55 °C; 1 min @ 72 °C); 4 °C hold. The product was precipitated by: adding 10 µL of 3 M NaOAc and 250 µL ethanol per 100 µL of reaction; placing in the -80 °C freezer for 1.5+ hours; centrifuging 20 minutes at

16,100 rcf; supernatant decanted; washing with 70% ethanol; centrifuging 10 minutes at 16,100 rcf; supernatant decanted; allowed to dry in ambient air for 15+ minutes. The product was dissolved in DEPC water and the checked with a 6% native polyacrylamide gel. Pilot PCR was done by pulling aliquots from a 100 µL every 5 cycles and checking the reaction progress on a polyacrylamide gel.

Table 4.4. PCR conditions for the various PCR reactions run.

	Random pool	**Rev. Trans. Product**	**From Isolated plasmid**
Starting DNA	120 nM Template E	5 µL per 100 µL	6 µL per 100 µL
3'Primer	0.5 µM 3pPB2a	0.5 µM 3pPB2a	1 µM 3pPB2a
5'Primer	0.5 µM 5pE	0.5 µM 5pE	1 µM 5pPASE 17#21
dNTPs	250 µM each	250 µM each	250 µM each
Buffer	1x diluted from 10x	1x diluted from 10x	1x diluted from 10x
$MgCl_2$	3 mM	3 mM	3 mM
DMSO	10%	10%	10%
Taq Polymerase	2.5 units	2.5 units	2.5 units
# cycles	6	Based on pilot PCR	25 cycles

4.5.3 Transcription. Transcription reactions were run using 10 µL of PCR product per 100 µL of reaction containing the following reagents: 2 mM NTPs; 1x buffer diluted from 5x; 10 mM DTT; 1 unit/µL RNAse OUT; 2 unit/µL T7 RNA polymerase. For making ^{32}P labeled RNA, 1 µL of α-^{32}P ATP per 100 µL of reaction was added. The reaction was allowed to react overnight in the Eppendorf Mastercycler Personal using the program: 6 hours @ 37 °C; hold 4 °C. The product was purified on an 8% 8M urea denaturing gel and extracted from the gel using an gel elution buffer (50 mM Tris-Cl pH 8.0; 200 mM NaOAc; 0.2% SDS; 4 mM EDTA pH 8.0). The product was precipitated by: adding 10 µL of 3 M NaOAc and 250 µL ethanol per 100 µL of reaction; placing in the -80 °C freezer for 1.5+ hours; centrifuging 20 minutes at 16,100 rcf;

decanting supernatant; washing with 70% ethanol; centrifuging 10 minutes at 16,100 rcf; decanting supernatant; allowing to dry in ambient air for 15+ minutes.

4.5.4 Reverse Transcription. Reverse transcription was done by dissolving all of the isolated RNA in 27.5 µL of water and transferred to a 200 µL PCR tube. After the addition of 3 µL of 100 µM 3pPB2a primer the tube was heated for 5 min @ 85 °C in the Eppendorf Mastercycler Personal. After cooling to 42 °C the enzyme/buffer mixture (10 µL of 5x buffer; 2.5 µL of 100 mM DTT; 5 µL of 10 mM dNTPs; 2 µL of SuperScript III reverse transcriptase) was added. The following temperature program was run: 5 min @ 42 °C; 59 min @ 55 °C; 20 min @ 37 °C; 15 min @ 75 °C; hold 4 °C. The crude reaction mixture was then used in subsequent steps.

4.5.5 Selection #1 Procedure. The selection began by running PCR on 1 nmol of Template E and then transcribing the product DNA to ^{32}P labeled RNA. The selection buffer contained: 20 mM HEPES, pH 7.2; 5 mM $MgCl_2$; 30 mM NaCl. The Pt crystal of interest was assembled in the reactor in Figure 4.3. The reactor was washed by stirring water in it for 5 minutes followed by 3 washes using the selection buffer. For round 1, 5 nmol of RNA (25 µM) was dissolved 200 µL of selection buffer in a 200 µL PCR tube, the whole tube was placed in a scintillation vial, and the radioactive decay was counted using the Beckman LS-6500. The RNA solution was added to the reactor and magnetically stirred. The empty tube was counted using the LS. After stirring for 3 hours the RNA solution was removed and placed in a fresh PCR tube and counted. 3 washes were done with 200 µL of the selection buffer for 15 minutes each and the third wash was done at 65-70 °C. Each wash was saved and counted on the LS counter. Then the RNA was eluted using formamide that had been stored under an argon atmosphere.

Three 200 µL formamide washes at 65-70 °C for 1 hour were done and the recovered solution was counted. The RNA was precipitated using the same procedure as described in the "Transcription" section. The LS counts were used to calculate the percent recovery using the initial counts minus the counts for the empty tube as the 100% mark. The recovered RNA was then reverse transcribed, amplified by PCR, and used in the next round. Rounds 2-10 started with 0.5 nmol of RNA was used to give a 2.5 µM concentration. The size of the hole in the Teflon piece was changed from round to round as described in the text.

4.5.6 Selection #2 Procedure. The selection began by running PCR on 1 nmol of Template E and then transcribing the product DNA to ^{32}P labeled RNA. The selection buffer contained: 20 mM potassium phosphate at pH 7.2. The RNA was put through a refolding procedure which involved heating it to 95 °C for 5 minutes and then cooling on ice for 20+ minutes. **Counter selection**: The Pt crystal exposing the facet not of interest was assembled in the reactor in Figure 4.3. The reactor was washed 3 times by adding fresh selection buffer to the reactor and allowing it to stir inside for 5 minutes. For round 1, 1 nmol of RNA (5 µM) was dissolved 200 µL of selection buffer in a 200 µL PCR tube, the whole tube was placed in a scintillation vial, and the radioactive decay was counted using the Beckman LS-6500. The RNA solution was added to the reactor and magnetically stirred. The empty tube was counted using the LS. After stirring for 1 hour the RNA solution was removed and placed in a fresh PCR tube and counted. **Selection**: The Pt crystal exposing the crystal of interest was then assembled in the reactor. The reactor was washed 3 times by adding fresh selection buffer to the reactor and allowing it to stir inside for 5 minutes. The RNA solution was added to the reactor and magnetically stirred for 3 hours. After that, 3 washes were done with 200 µL of the selection

buffer for 15 minutes each. Each wash was saved and counted on the LS counter. Then the RNA was eluted using formamide that had been stored under an argon atmosphere. Three 200 µL formamide washes at 65-70 °C for 1 hour were done and the recovered solution was counted. The RNA was precipitated using the same procedure as described in the "Transcription" section. The LS counts were used to calculate the percent recovery using the total counts after the counter selection minus the counts for the empty tube as the 100% mark. The recovered RNA was then reverse transcribed, amplified by PCR, and used in the next round. Rounds 2-12 started with 0.5 nmol of RNA was used to give a 2.5 µM concentration. The size of the hole in the Teflon piece was changed from round to round as described in the text.

4.5.7 Sequencing. Sequencing was done with the pGEM-T Easy Vector Kit (cat. No. A1380) from Promega using the protocol supplied with the kit. 3 µL of PCR product from the final selection round was ligated into the pGEM-T Easy Vector plasmid according to the instructions. The ligated plasmids were then transformed into the JM109 High Efficiency Competent Cells supplied with the kit using the protocol provided. The transformation products were then plated on 6 LB agar plates containing ampicillin, IPTG, and X-Gal. The plates were incubated overnight and the following day 60 white colonies from each selection were picked and streaked on new LB agar ampicillin/IPTG/X-Gal plates in a grid fashion with 30 colonies on each. 12 colonies for each selection were cultured and their plasmids isolated using the Qiagen QIAprep® Spin Miniprep Kit. The plasmids were digested using EcoRI restriction enzyme and the product tested on a 6% native PAGE to confirm inserts of the proper size were inserted into the plasmids. After confirmation 60 colonies for each selection were sent to Bio Basic, Inc to be sequenced. Glycerol stocks were made for each colony by culturing each in LB

overnight, mixing with 15% glycerol and stored in 1.5 mL tubes in the -80 °C freezer. To make RNA of the single sequences, the glycerol stock was cultured in LB overnight. Then the plasmids were isolated from the bacteria. PCR was run on the resulting plasmid solution and the PCR product was transcribed into RNA.

4.5.8 RNA Mediated Pt NP synthesis. The synthesis began with aging a 10 mM K_2PtCl_4 solution in water for 3 days. On the day of the synthesis freshly prepared, gel purified RNA was diluted in the reaction buffer to a total volume of 380 µL. The RNA solution was put through a refolding procedure which involved heating it to 95 °C for 5 minutes and then cooling on ice for 20+ minutes. The RNA solutions were transferred to 1.5 mL tubes and places in a temperature controlled reaction block at 20 °C with orbital mixing. 20 µL of K_2PtCl_4 solution (0.5 mM final) was added immediately before two holes were punched in the top of the tub with 16G and 20G needles. Polyethylene tubing with a diameter equal to the 16G hole was inserted through the hole in the top of the tube and argon gas was bubbled through the solution for 10 minutes. The polyethylene tubing was cleaned with RNase Away to remove any nucleases. Fresh tubing was used for each reaction by trimming the end of the tube after it was used. After 10 minutes with argon a second tube was used to bubble hydrogen gas through the solution for 5 minutes. Immediately after the hydrogen tube was removed the tube was sealed tight with Parafilm and left in the reaction block overnight (~18h).

4.5.9 TEM. TEM samples were prepared on 300 mesh carbon coated copper grids (Electron Microscopy Sciences CF300-Cu). The grids were typically glow discharge cleaned with an ambient air plasma to create a negatively charged hydrophilic surface. 4 µL of sample was allowed to completely dry on the surface of the grid and then water (10 µL drops) was used to

wash the surface 3 times. The washing procedure involved dropping the water on the surface of the grid and then wicking it away after 1 minute with filter paper. Standard brightfield TEM images were collected on a Phillips CM 100 TEM operating at 100 kV.

4.5.10 HR-TEM. HR-TEM samples were prepared using the same procedure as the normal resolution sample only the grids were holy carbon coated 400 mesh copper grids from Ted Pella. HR images were collected by the CAMCOR facility at the University of Oregon on a FEI Titan 80-300kV FEG-TEM operated at an acceleration voltage of 300 kV. Fast Fourier transforms (FFT) of the images were calculated using the ImageJ software package available as a public domain program in the internet. A selected area FFT was calculated by drawing a box around the particle in a calibrated image. The spots were then measured as a distance r from the center of the FFT using the spot measure function in ImageJ. Pairs of spots 180° apart from each other represented the same lattice spacing for a given set of planes. The distance for each spot of the 180° pair was averaged to determine the measurement used to index the set of planes based on the lattice spacings calculated by Equation 2. The faces of the particle perpendicular to the electron beam were then indexed by determining their angle with the observed lattice planes. If there was a 0° angle with the lattice plane, the face was said to be equal to that plane and measured. If no set of planes terminated in that surface, the angle of the surface with two separate sets of planes was determined. Based on this information in comparison to the angles calculated by Equation 3 and shown in the surface was indexed and measured. Pt NPs made with 3 pools of RNA were analyzed: Random pool (10 particles, 251.2 nm surface area); {111} selected pool (10 particles 222.8 nm surface area); and {100} selected

pool (13 particles, 245.7 nm surface area). The surface area indexed as (111), (110), and (100) was totaled and a percentage of the total surface area measured was determined.

Table 4.5. Angles between planes (hkl) and ($h'k'l'$) in FCC metals.

h	*k*	*l*	*h'*	*k'*	*l'*	Angle°	*h*	*k*	*l*	*h'*	*k'*	*l'*	Angle°
1	0	0	1	1	1	**54.74**	1	1	1	1	0	0	**54.74**
1	0	0	1	1	0	**45.00**	1	1	1	1	1	0	**35.26**
1	0	0	2	1	0	**26.57**	1	1	1	2	1	0	**39.23**
1	0	0	-1	1	1	**125.26**	1	1	1	-1	1	1	**70.53**
1	0	0	0	1	0	**90.00**	1	1	1	-1	0	0	**125.26**
1	0	0	-1	1	0	**135.00**	1	1	1	-1	1	0	**90.00**

4.5.11 Binding Experiments. Binding experiments were conducted using the methods described in detail in the text. ^{32}P labeled RNA was used in the experiments and a phosphor screen in conjunction with a Perkin Elmer Cyclone Plus imager were used for imaging the surface of the crystal. The screen was imaged at the highest resolution the instrument was capable of (600 dpi), and the associated software was used to quantitate the spots. The crystals were marked with a sharpie to maintain orientation when imaged. The Pt crystals were cleaned by soaking in formamide at ~70 °C overnight in between experiments.

4.6 References

1. Feldheim, D. L., The new face of catalysis. *Science* 2007, 316, 699-700.

2. Peng, Z. M.; Yang, H., Designer platinum nanoparticles: Control of shape, composition in alloy, nanostructure and electrocatalytic property. *Nano Today* 2009, 4, 143-164.

3. Mahmoud, M. A.; Narayanan, R.; El-Sayed, M. A., Enhancing Colloidal Metallic Nanocatalysis: Sharp Edges and Corners for Solid Nanoparticles and Cage Effect for Hollow Ones. *Acc. Chem. Res.* 2013.

4. Narayanan, R.; El-Sayed, M. A., Shape-dependent catalytic activity of platinum nanoparticles in colloidal solution. *Nano Lett.* 2004, 4, 1343-1348.

5. Burda, C.; Chen, X. B.; Narayanan, R.; El-Sayed, M. A., Chemistry and properties of nanocrystals of different shapes. *Chem. Rev. (Washington, DC, U. S.)* 2005, 105, 1025-1102.

6. Narayanan, R.; El-Sayed, M. A., Changing catalytic activity during colloidal platinum nanocatalysis due to shape changes: Electron-transfer reaction. *J. Am. Chem. Soc.* 2004, 126, 7194-7195.

7. Narayanan, R.; El-Sayed, M. A., Effect of nanocatalysis in colloidal solution on the tetrahedral and cubic nanoparticle SHAPE: Electron-transfer reaction catalyzed by platinum nanoparticles. *J. Phys. Chem. B* 2004, 108, 5726-5733.

8. Tian, N.; Zhou, Z. Y.; Sun, S. G.; Ding, Y.; Wang, Z. L., Synthesis of tetrahexahedral platinum nanocrystals with high-index facets and high electro-oxidation activity. *Science* 2007, 316, 732-735.

9. Ahmadi, T. S.; Wang, Z. L.; Green, T. C.; Henglein, A.; ElSayed, M. A., Shape-controlled synthesis of colloidal platinum nanoparticles. *Science* 1996, 272, 1924-1926.

10. Mahmoud, M. A.; Tabor, C. E.; El-Sayed, M. A.; Ding, Y.; Wang, Z. L., A new catalytically active colloidal platinum nanocatalyst: The multiarmed nanostar single crystal. *J. Am. Chem. Soc.* 2008, 130, 4590.

11. Feldheim, D. L.; Eaton, B. E., Selection of biomolecules capable of mediating the formation of nanocrystals. *ACS Nano* 2007, 1, 154-159.

12. Gugliotti, L. A.; Feldheim, D. L.; Eaton, B. E., RNA-mediated control of metal nanoparticle shape. *J. Am. Chem. Soc.* 2005, 127, 17814-17818.

13. Gugliotti, L. A.; Feldheim, D. L.; Eaton, B. E., RNA-mediated metal-metal bond formation in the synthesis of hexagonal palladium nanoparticles. *Science* 2004, 304, 850-852.

14. Ma, N.; Dooley, C. J.; Kelley, S. O., RNA-Templated Semiconductor Nanocrystals. *J. Am. Chem. Soc.* 2006, 128, 12598-12599.

15. Kumar, A.; Jakhmola, A., RNA-Templated Fluorescent Zn/PbS (PbS + Zn2+) Supernanostructures. *The Journal of Physical Chemistry C* 2009, 113, 9553-9559.

16. Kumar, A.; Jakhmola, A., RNA-Mediated Fluorescent Q-PbS Nanoparticles. *Langmuir* 2007, 23, 2915-2918.

17. Carter, C. J.; Dolska, M.; Owczarek, A.; Ackerson, C. J.; Eaton, B. E.; Feldheim, D. L., In vitro selection of RNA sequences capable of mediating the formation of iron oxide nanoparticles. *J. Mater. Chem.* 2009, 19, 8320-8326.

18. Carter, C. J.; Owczarek, A.; Feldheim, D. L., Methods for Isolating RNA Sequences Capable of Binding to or Mediating the Formation of Inorganic Materials. In *NanoBiotechnology Protocols*, Rosenthal, S. J.; Wright, D. W., Eds. Humana Press: 2013; Vol. 1026.

19. Tindall, K. R.; Kunkel, T. A., Fidelity of DNA synthesis by the Thermus aquaticus DNA polymerase. *Biochemistry* 1988, 27, 6008-6013.

20. Henglein, A.; Ershov, B. G.; Malow, M., Absorption-Spectrum And Some Chemical-Reactions Of Colloidal Platinum In Aqueous-Solution. *J. Phys. Chem.* 1995, 99, 14129-14136.

21. Henglein, A.; Giersig, M., Reduction of Pt(II) by H-2: Effects of citrate and NaOH and reaction mechanism. *J. Phys. Chem. B* 2000, 104, 6767-6772.

22. Laing, C.; Schlick, T., Computational approaches to RNA structure prediction, analysis, and design. *Curr. Opin. Struct. Biol.* 2011, 21, 306-318.

23. Zuker, M., Mfold web server for nucleic acid folding and hybridization prediction. *Nucleic Acids Res.* 2003, 31, 3406-3415.

24. Potgieter, J. H., Adsorption of methylene blue on activated carbon: An experiment illustrating both the Langmuir and Freundlich isotherms. *J. Chem. Educ.* 1991, 68, 349.

25. Shiman, R.; Draper, D. E., Stabilization of RNA tertiary structure by monovalent cations. *J. Mol. Biol.* 2000, 302, 79-91.

26. Delisi, C.; Crothers, D. M., Prediction Of RNA Secondary Structure. *Proc. Natl. Acad. Sci. U. S. A.* 1971, 68, 2682-&.

27. Kelly, A.; Knowles, K. M., Appendix 3: Interplanar Spacings and Interplanar Angles. In *Crystallography and Crystal Defects*, John Wiley & Sons, Ltd: 2012; pp 469-472.

5. Bibliography

1. Ahmadi, T. S.; Wang, Z. L.; Green, T. C.; Henglein, A.; ElSayed, M. A., Shape-controlled synthesis of colloidal platinum nanoparticles. *Science* 1996, 272, 1924-1926.

2. Akhtar, M. S.; Panwar, J.; Yun, Y.-S., Biogenic Synthesis of Metallic Nanoparticles by Plant Extracts. *ACS Sustainable Chemistry & Engineering* 2013.

3. Alivisatos, A. P., Perspectives on the physical chemistry of semiconductor nanocrystals. *J. Phys. Chem.* 1996, 100, 13226-13239.

4. Alivisatos, P.; Cummings, P.; De Yoreo, J.; Fichthorn, K.; Gates, B.; Hwang, R.; Lowndes, D.; Majumdar, A.; Makowski, L.; Michalske, T.; Misewich, J.; Murray, C.; Sibener, S.; Teague, C.; Williams, E. *Nanoscience Research for Energy Needs. Report of the National Nanotechnology Initiative Grand Challenge Workshop, March 16-18, 2004*; 2004; p Medium: ED.

5. Andelman, T.; Gong, Y.; Polking, M.; Yin, M.; Kuskovsky, I.; Neumark, G.; O'Brien, S., Morphological Control and Photoluminescence of Zinc Oxide Nanocrystals. *J. Phys. Chem. B* 2005, 109, 14314-14318.

6. Antolini, E.; Lopes, T.; Gonzalez, E. R., An overview of platinum-based catalysts as methanol-resistant oxygen reduction materials for direct methanol fuel cells. *J. Alloys Compd.* 2008, 461, 253-262.

7. Arai, T.; Konishi, Y.; Iwasaki, Y.; Sugihara, H.; Sayama, K., High-throughput screening using porous photoelectrode for the development of visible-light-responsive semiconductors. *J. Comb. Chem.* 2007, 9, 574-581.

8. Arakaki, A.; Webb, J.; Matsunaga, T., A Novel Protein Tightly Bound to Bacterial Magnetic Particles in Magnetospirillum magneticum Strain AMB-1. *J. Biol. Chem.* 2003, 278, 8745-8750.

9. Bauer, J. C.; Chen, X.; Liu, Q. S.; Phan, T. H.; Schaak, R. E., Converting nanocrystalline metals into alloys and intermetallic compounds for applications in catalysis. *J. Mater. Chem.* 2008, 18, 275-282.

10. Bell, A. T.; Gates, B. C.; Ray, D.; Thompson, M. R. *Basic Research Needs: Catalysis for Energy*; PNNL-17214; Other: KC0302010; TRN: US200816%%673; 2008; p Medium: ED; Size: PDFN.

11. Bonnemann, H.; Richards, R. M., Nanoscopic metal particles - Synthetic methods and potential applications. *Eur. J. Inorg. Chem.* 2001, 2455-2480.

12. Burda, C.; Chen, X. B.; Narayanan, R.; El-Sayed, M. A., Chemistry and properties of nanocrystals of different shapes. *Chem. Rev. (Washington, DC, U. S.)* 2005, 105, 1025-1102.

13. Cable, R. E.; Schaak, R. E., Low-temperature solution synthesis of nanocrystalline binary intermetallic compounds using the polyol process. *Chem. Mater.* 2005, 17, 6835-6841.

14. Cai, W. P.; Zhong, H. C.; Zhang, L. D., Optical measurements of oxidation behavior of silver nanometer particle within pores of silica host. *J. Appl. Phys.* 1998, 83, 1705-1710.

15. Cao, G.; Lee, H.; Lynch, V. M.; Mallouk, T. E., Synthesis And Structural Characterization of a Homologous Series of Divalent-Metal Phosphonates, MII(O3PR).H2O And MII(HO3PR)2. *Inorg. Chem.* 1988, 27, 2781-2785.

16. Cao, G.; Mallouk, T. E., Shape-Selective Intercalation Reactions of Layered Zinc And Cobalt Phosphonates. *Inorg. Chem.* 1991, 30, 1434-1438.

17. Carter, C. J.; Ackerson, C. J.; Feldheim, D. L., Unusual Reactivity of a Silver Mineralizing Peptide. *ACS Nano* 2010, 4, 3883-3888.

18. Carter, C. J.; Dolska, M.; Owczarek, A.; Ackerson, C. J.; Eaton, B. E.; Feldheim, D. L., In vitro selection of RNA sequences capable of mediating the formation of iron oxide nanoparticles. *J. Mater. Chem.* 2009, 19, 8320-8326.

19. Carter, C. J.; Owczarek, A.; Feldheim, D. L., Methods for Isolating RNA Sequences Capable of Binding to or Mediating the Formation of Inorganic Materials. In *NanoBiotechnology Protocols*, Rosenthal, S. J.; Wright, D. W., Eds. Humana Press: 2013; Vol. 1026.

20. Chen, Y. F.; Kim, M.; Lian, G.; Johnson, M. B.; Peng, X. G., Side reactions in controlling the quality, yield, and stability of high quality colloidal nanocrystals. *J. Am. Chem. Soc.* 2005, 127, 13331-13337.

21. Choi, S. H.; Kim, E. G.; Park, J.; An, K.; Lee, N.; Kim, S. C.; Hyeon, T., Large-scale synthesis of hexagonal pyramid-shaped ZnO nanocrystals from thermolysis of Zn-oleate complex. *J. Phys. Chem. B* 2005, 109, 14792-14794.

22. Clearfield, A., Recent advances in metal phosphonate chemistry. *Curr. Opin. Solid State Mater. Sci.* 1996, 1, 268-278.

23. Clearfield, A., Chapter 1 The Early History and Growth of Metal Phosphonate Chemistry. In *Metal Phosphonate Chemistry: From Synthesis to Applications*, The Royal Society of Chemistry: 2012; Vol. 0, pp 1-44.

24. Cozzoli, P. D.; Curri, M. L.; Agostiano, A.; Leo, G.; Lomascolo, M., ZnO nanocrystals by a non-hydrolytic route: Synthesis and characterization. *J. Phys. Chem. B* 2003, 107, 4756-4762.

25. Cunningham, D.; Hennelly, P. J. D., Divalent Metal Phenylphosphonates and Phenylarsonates. *Inorg. Chim. Acta* 1979, 37, 95-102.

26. Deemie, R. W.; Knight, A.; Rao, M., An organometallic sol-gel route to layered zinc phenylphosphonate and encapsulation studies with eta(6)-(C6H6)Cr(CO)(3). *J. Organomet. Chem.* 1999, 585, 162-166.

27. Delisi, C.; Crothers, D. M., PREDICTION OF RNA SECONDARY STRUCTURE. *Proc. Natl. Acad. Sci. U. S. A.* 1971, 68, 2682-&.

28. Demir, M. M.; Munoz-Espi, R.; Lieberwirth, I.; Wegner, G., Precipitation of monodisperse ZnO nanocrystals via acid-catalyzed esterification of zinc acetate. *J. Mater. Chem.* 2006, 16, 2940-2947.

29. Dewey, T. M.; Mundt, A. A.; Crouch, G. J.; Zyzniewski, M. C.; Eaton, B. E., NEW URIDINE DERIVATIVES FOR SYSTEMATIC EVOLUTION OF RNA LIGANDS BY EXPONENTIAL ENRICHMENT. *J. Am. Chem. Soc.* 1995, 117, 8474-8475.

30. Faraday, M., The Bakerian Lecture: Experimental Relations of Gold (and Other Metals) to Light. *Philosophical Transactions of the Royal Society of London* 1857, 147, 145-181.

31. Feldheim, D. L., The new face of catalysis. *Science* 2007, 316, 699-700.

32. Feldheim, D. L.; Eaton, B. E., Selection of biomolecules capable of mediating the formation of nanocrystals. *ACS Nano* 2007, 1, 154-159.

33. Ferrando, R.; Jellinek, J.; Johnston, R. L., Nanoalloys: From theory to applications of alloy clusters and nanoparticles. *Chem. Rev. (Washington, DC, U. S.)* 2008, 108, 845-910.

34. Fredoueil, F.; Penicaud, V.; BujoliDoeuff, M.; Bujoli, B., Syntheses and crystal structures of the new zinc phosphonates Zn(O3PCH2P)(O)(R)(C6H5))center dot xH(2)O, based on mixed phosphonic acid phosphine oxide building blocks. *Inorg. Chem.* 1997, 36, 4702-4706.

35. Frink, K. J.; Wang, R. C.; Colon, J. L.; Clearfield, A., Intercalation of Ammonia Into Zinc and Cobalt Phenylphosphonates. *Inorg. Chem.* 1991, 30, 1438-1441.

36. Gao, W.; Dickinson, L.; Morin, F. G.; Reven, L., Phase transitions in lamellar alkylphosphonate salts. *Chem. Mater.* 1997, 9, 3113-3120.

37. Gerbier, P.; Guerin, C.; Henner, B.; Unal, J. R., An organometallic route to zinc phosphonates and their intercalates. *J. Mater. Chem.* 1999, 9, 2559-2565.

38. Gomes, R.; Hassinen, A.; Szczygiel, A.; Zhao, Q.; Vantomme, A.; Martins, J. C.; Hens, Z., Binding of Phosphonic Acids to CdSe Quantum Dots: A Solution NMR Study. *J. Phys. Chem. Lett.* 2011, 2, 145-152.

39. Guang, C.; Hong, H. G.; Mallouk, T. E., Layered Metal Phosphates And Phosphonates - From Crystals to Monolayers. *Acc. Chem. Res.* 1992, 25, 420-427.

40. Gugliotti, L. A.; Feldheim, D. L.; Eaton, B. E., RNA-mediated metal-metal bond formation in the synthesis of hexagonal palladium nanoparticles. *Science* 2004, 304, 850-852.

41. Gugliotti, L. A.; Feldheim, D. L.; Eaton, B. E., RNA-mediated control of metal nanoparticle shape. *J. Am. Chem. Soc.* 2005, 127, 17814-17818.

42. Gurau, B.; Viswanathan, R.; Liu, R. X.; Lafrenz, T. J.; Ley, K. L.; Smotkin, E. S.; Reddington, E.; Sapienza, A.; Chan, B. C.; Mallouk, T. E.; Sarangapani, S., Structural and electrochemical characterization of binary, ternary, and quaternary platinum alloy catalysts for methanol electro-oxidation. *J. Phys. Chem. B* 1998, 102, 9997-10003.

43. Hanak, J. J., The "multiple-sample concept" in materials research: Synthesis, compositional analysis and testing of entire multicomponent systems. *J. Mater. Sci.* 1970, 5, 964-971.

44. Hemminger, J. *New Science for a Secure and Sustainable Energy Future*; U.S. Department of Energy: 2008; p Medium: ED.

45. Henglein, A.; Ershov, B. G.; Malow, M., ABSORPTION-SPECTRUM AND SOME CHEMICAL-REACTIONS OF COLLOIDAL PLATINUM IN AQUEOUS-SOLUTION. *J. Phys. Chem.* 1995, 99, 14129-14136.

46. Henglein, A.; Giersig, M., Reduction of Pt(II) by H-2: Effects of citrate and NaOH and reaction mechanism. *J. Phys. Chem. B* 2000, 104, 6767-6772.

47. Jandeleit, B.; Schaefer, D. J.; Powers, T. S.; Turner, H. W.; Weinberg, W. H., Combinatorial materials science and catalysis. *Angewandte Chemie-International Edition* 1999, 38, 2495-2532.

48. Jang, J. S.; Lee, J.; Ye, H.; Fan, F. R. F.; Bard, A. J., Rapid Screening of Effective Dopants for Fe2O3 Photocatalysts with Scanning Electrochemical Microscopy and Investigation of Their Photoelectrochemical Properties. *J. Phys. Chem. C* 2009, 113, 6719-6724.

49. Jayaraman, S.; Hillier, A. C., Electrochemical synthesis and reactivity screening of a ternary composition gradient for combinatorial discovery of fuel cell catalysts. *Meas. Sci. Technol.* 2005, 16, 5-13.

50. Joo, J.; Kwon, S. G.; Yu, J. H.; Hyeon, T., Synthesis of ZnO nanocrystals with cone, hexagonal cone, and rod shapes via non-hydrolytic ester elimination sol-gel reactions. *Adv. Mater. (Weinheim, Ger.)* 2005, 17, 1873-+.

51. Joyce, G. F., Forty Years of In Vitro Evolution. *Angewandte Chemie International Edition* 2007, 46, 6420-6436.

52. Jun, Y.-w.; Choi, J.-s.; Cheon, J., Shape Control of Semiconductor and Metal Oxide Nanocrystals through Nonhydrolytic Colloidal Routes. *Angewandte Chemie International Edition* 2006, 45, 3414-3439.

53. Kang, Y. J.; Murray, C. B., Synthesis and Electrocatalytic Properties of Cubic Mn-Pt Nanocrystals (Nanocubes). *J. Am. Chem. Soc.* 2010, 132, 7568-+.

54. Katz, J. E.; Gingrich, T. R.; Santori, E. A.; Lewis, N. S., Combinatorial synthesis and high-throughput photopotential and photocurrent screening of mixed-metal oxides for photoelectrochemical water splitting. *Energy & Environmental Science* 2009, 2, 103-112.

55. Kelly, A.; Knowles, K. M., Appendix 3: Interplanar Spacings and Interplanar Angles. In *Crystallography and Crystal Defects*, John Wiley & Sons, Ltd: 2012; pp 469-472.

56. Khlebtsov, B. N.; Khanadeyev, V. A.; Ye, J.; Mackowski, D. W.; Borghs, G.; Khlebtsov, N. G., Coupled plasmon resonances in monolayers of metal nanoparticles and nanoshells. *Physical Review B* 2008, 77.

57. Kramer, S.; Xie, H.; Gaff, J.; Williamson, J. R.; Tkachenko, A. G.; Nouri, N.; Feldheim, D. A.; Feldheim, D. L., Preparation of protein gradients through the controlled deposition of protein-nanoparticle conjugates onto functionalized surfaces. *J. Am. Chem. Soc.* 2004, 126, 5388-5395.

58. Kumar, A.; Jakhmola, A., RNA-Mediated Fluorescent Q-PbS Nanoparticles. *Langmuir* 2007, 23, 2915-2918.

59. Kumar, A.; Jakhmola, A., RNA-Templated Fluorescent Zn/PbS (PbS + Zn2+) Supernanostructures. *The Journal of Physical Chemistry C* 2009, 113, 9553-9559.

60. Kwon, S. G.; Hyeon, T., Colloidal Chemical Synthesis and Formation Kinetics of Uniformly Sized Nanocrystals of Metals, Oxides, and Chalcogenides. *Acc. Chem. Res.* 2008, 41, 1696-1709.

61. Laing, C.; Schlick, T., Computational approaches to RNA structure prediction, analysis, and design. *Curr. Opin. Struct. Biol.* 2011, 21, 306-318.

62. Lee, J. W.; Ye, H. C.; Pan, S. L.; Bard, A. J., Screening of photocatalysts by scanning electrochemical microscopy. *Anal. Chem.* 2008, 80, 7445-7450.

63. Lee, K.; Tienes, B. M.; Wilker, M. B.; Schnitzenbaumer, K. J.; Dukovic, G., (Ga1–xZnx)(N1–xOx) Nanocrystals: Visible Absorbers with Tunable Composition and Absorption Spectra. *Nano Lett.* 2012, 12, 3268-3272.

64. Lee, S.-M.; Jun, Y.-w.; Cho, S.-N.; Cheon, J., Single-Crystalline Star-Shaped Nanocrystals and Their Evolution: Programming the Geometry of Nano-Building Blocks. *J. Am. Chem. Soc.* 2002, 124, 11244-11245.

65. Leger, J. M., Mechanistic aspects of methanol oxidation on platinum-based electrocatalysts. *J. Appl. Electrochem.* 2001, 31, 767-771.

66. Lewis, N. S.; Nocera, D. G., Powering the planet: Chemical challenges in solar energy utilization. *Proc. Natl. Acad. Sci. U. S. A.* 2006, 103, 15729-15735.

67. Li, Y.; Shen, W., Morphology-dependent nanocatalysis on metal oxides. *Science China Chemistry* 2012, 55, 2485-2496.

68. Link, S.; El-Sayed, M. A., Spectral properties and relaxation dynamics of surface plasmon electronic oscillations in gold and silver nanodots and nanorods. *J. Phys. Chem. B* 1999, 103, 8410-8426.

69. Link, S.; Wang, Z. L.; El-Sayed, M. A., Alloy formation of gold-silver nanoparticles and the dependence of the plasmon absorption on their composition. *J. Phys. Chem. B* 1999, 103, 3529-3533.

70. Liu, G. J.; Bard, A. J., Rapid Preparation and Photoelectrochemical Screening of CuInSe2 and CuInMSe2 Arrays by Scanning Electrochemical Microscopy. *J. Phys. Chem. C* 2010, 114, 17509-17513.

71. Liu, G. J.; Liu, C. Y.; Bard, A. J., Rapid Synthesis and Screening of Zn(x)zCd(1-x)S(y)Se(1-y) Photocatalysts by Scanning Electrochemical Microscopy. *J. Phys. Chem. C* 2010, 114, 20997-21002.

72. Liu, H. S.; Song, C. J.; Zhang, L.; Zhang, J. J.; Wang, H. J.; Wilkinson, D. P., A review of anode catalysis in the direct methanol fuel cell. *J. Power Sources* 2006, 155, 95-110.

73. Liu, H. T.; Owen, J. S.; Alivisatos, A. P., Mechanistic study of precursor evolution in colloidal group II-VI semiconductor nanocrystal synthesis. *J. Am. Chem. Soc.* 2007, 129, 305-312.

74. Liu, W.; Ye, H. C.; Bard, A. J., Screening of Novel Metal Oxide Photocatalysts by Scanning Electrochemical Microscopy and Research of Their Photoelectrochemical Properties. *J. Phys. Chem. C* 2010, 114, 1201-1207.

75. Luschtinetz, R.; Seifert, G.; Jaehne, E.; Adler, H.-J. P., Infrared Spectra of Alkylphosphonic Acid Bound to Aluminium Surfaces. *Macromol. Symp.* 2007, 254, 248-253.

76. Ma, N.; Dooley, C. J.; Kelley, S. O., RNA-Templated Semiconductor Nanocrystals. *J. Am. Chem. Soc.* 2006, 128, 12598-12599.

77. Mahmoud, M. A.; Narayanan, R.; El-Sayed, M. A., Enhancing Colloidal Metallic Nanocatalysis: Sharp Edges and Corners for Solid Nanoparticles and Cage Effect for Hollow Ones. *Acc. Chem. Res.* 2013.

78. Mahmoud, M. A.; Tabor, C. E.; El-Sayed, M. A.; Ding, Y.; Wang, Z. L., A new catalytically active colloidal platinum nanocatalyst: The multiarmed nanostar single crystal. *J. Am. Chem. Soc.* 2008, 130, 4590-+.

79. Manna, L.; Scher, E. C.; Alivisatos, A. P., Synthesis of soluble and processable rod-, arrow-, teardrop-, and tetrapod-shaped CdSe nanocrystals. *J. Am. Chem. Soc.* 2000, 122, 12700-12706.

80. Manna, L.; Scher, E. C.; Alivisatos, A. P., Shape control of colloidal semiconductor nanocrystals. *J. Cluster Sci.* 2002, 13, 521-532.

81. Martin, K. J.; Squattrito, P. J.; Clearfield, A., The Crystal and Molecular-Strucuture of Zinc Phenylphosphonate. *Inorg. Chim. Acta* 1989, 155, 7-9.

82. Massiot, D.; Drumel, S.; Janvier, P.; BujoliDoeuff, M.; Bujoli, B., Relationship between solid-state P-31 NMR parameters and X-ray structural data in some zinc phosphonates. *Chem. Mater.* 1997, 9, 6-&.

83. May, E. L.; Hillier, A. C., Rapid and reversible generation of a microscale pH gradient using surface electric fields. *Anal. Chem.* 2005, 77, 6487-6493.

84. Maye, M. M.; Han, L.; Kariuki, N. N.; Ly, N. K.; Chan, W. B.; Luo, J.; Zhong, C. J., Gold and alloy nanoparticles in solution and thin film assembly: spectrophotometric determination of molar absorptivity. *Anal. Chim. Acta* 2003, 496, 17-27.

85. Milliron, D. J.; Hughes, S. M.; Cui, Y.; Manna, L.; Li, J. B.; Wang, L. W.; Alivisatos, A. P., Colloidal nanocrystal heterostructures with linear and branched topology. *Nature* 2004, 430, 190-195.

86. Mulvaney, P., Surface plasmon spectroscopy of nanosized metal particles. *Langmuir* 1996, 12, 788-800.

87. Narayanan, R.; El-Sayed, M. A., Shape-dependent catalytic activity of platinum nanoparticles in colloidal solution. *Nano Lett.* 2004, 4, 1343-1348.

88. Narayanan, R.; El-Sayed, M. A., Changing catalytic activity during colloidal platinum nanocatalysis due to shape changes: Electron-transfer reaction. *J. Am. Chem. Soc.* 2004, 126, 7194-7195.

89. Narayanan, R.; El-Sayed, M. A., Effect of nanocatalysis in colloidal solution on the tetrahedral and cubic nanoparticle SHAPE: Electron-transfer reaction catalyzed by platinum nanoparticles. *J. Phys. Chem. B* 2004, 108, 5726-5733.

90. Niederberger, M., Nonaqueous sol-gel routes to metal oxide nanoparticles. *Acc. Chem. Res.* 2007, 40, 793-800.

91. Okkerse, B., SELF-DIFFUSION OF GOLD. *Physical Review* 1956, 103, 1246-1249.

92. Osterloh, F. E.; Parkinson, B. A., Recent developments in solar water-splitting photocatalysis. *MRS Bulletin* 2011, 36, 17-22.

93. Owen, J. S.; Chan, E. M.; Liu, H.; Alivisatos, A. P., Precursor Conversion Kinetics and the Nucleation of Cadmium Selenide Nanocrystals. *J. Am. Chem. Soc.* 2010, 132, 18206-18213.

94. Ozgur, U.; Alivov, Y. I.; Liu, C.; Teke, A.; Reshchikov, M. A.; Dogan, S.; Avrutin, V.; Cho, S. J.; Morkoc, H., A comprehensive review of ZnO materials and devices. *J. Appl. Phys.* 2005, 98.

95. Pang, H. L.; Zhang, X. H.; Zhong, X. X.; Liu, B.; Wei, X. G.; Kuang, Y. F.; Chen, J. H., Preparation of Ru-doped SnO2-supported Pt catalysts and their electrocatalytic properties for methanol oxidation. *J. Colloid Interface Sci.* 2008, 319, 193-198.

96. Peng, X. G.; Manna, L.; Yang, W. D.; Wickham, J.; Scher, E.; Kadavanich, A.; Alivisatos, A. P., Shape control of CdSe nanocrystals. *Nature* 2000, 404, 59-61.

97. Peng, Z. A.; Peng, X. G., Mechanisms of the shape evolution of CdSe nanocrystals. *J. Am. Chem. Soc.* 2001, 123, 1389-1395.

98. Peng, Z. A.; Peng, X. G., Formation of high-quality CdTe, CdSe, and CdS nanocrystals using CdO as precursor. *J. Am. Chem. Soc.* 2001, 123, 183-184.

99. Peng, Z. A.; Peng, X. G., Nearly monodisperse and shape-controlled CdSe nanocrystals via alternative routes: Nucleation and growth. *J. Am. Chem. Soc.* 2002, 124, 3343-3353.

100. Peng, Z. M.; Yang, H., Designer platinum nanoparticles: Control of shape, composition in alloy, nanostructure and electrocatalytic property. *Nano Today* 2009, 4, 143-164.

101. Polarz, S., Shape Matters: Anisotropy of the Morphology of Inorganic Colloidal Particles - Synthesis and Function. *Adv. Funct. Mater.* 2011, 21, 3214-3230.

102. Poojary, D. M.; Zhang, B. L.; Bellinghausen, P.; Clearfield, A., Synthesis and X-ray powder structures of covalently pillared lamellar zinc bis(phosphonates). *Inorg. Chem.* 1996, 35, 5254-5263.

103. Potgieter, J. H., Adsorption of methylene blue on activated carbon: An experiment illustrating both the Langmuir and Freundlich isotherms. *J. Chem. Educ.* 1991, 68, 349.

104. Reddington, E.; Sapienza, A.; Gurau, B.; Viswanathan, R.; Sarangapani, S.; Smotkin, E. S.; Mallouk, T. E., Combinatorial electrochemistry: A highly parallel, optical screening method for discovery of better electrocatalysts. *Science* 1998, 280, 1735-1737.

105. Richards, C. I.; Choi, S.; Hsiang, J. C.; Antoku, Y.; Vosch, T.; Bongiorno, A.; Tzeng, Y. L.; Dickson, R. M., Oligonucleotide-stabilized Ag nanocluster fluorophores. *J. Am. Chem. Soc.* 2008, 130, 5038-+.

106. Rouge, J. L.; Eaton, B. E.; Feldheim, D. L., Biomolecules in the synthesis and assembly of materials for energy applications. *Energy & Environmental Science* 2011, 4, 398-402.

107. Sandrock, M. L.; Foss, C. A., Synthesis and linear optical properties of nanoscopic gold particle pair structures. *J. Phys. Chem. B* 1999, 103, 11398-11406.

108. Sau, T. K.; Rogach, A. L., Nonspherical Noble Metal Nanoparticles: Colloid-Chemical Synthesis and Morphology Control. *Adv. Mater. (Weinheim, Ger.)* 2010, 22, 1781-1804.

109. Schaak, R. E.; Cable, R. E.; Leonard, B. M.; Norris, B. C., Colloidal crystal microarrays and two-dimensional superstructures: A versatile approach for patterned surface assembly. *Langmuir* 2004, 20, 7293-7297.

110. Schaak, R. E.; Sra, A. K., Rapid low-temperature solution route to multimetallic solid state materials using nanoparticle precursors. *Abstr. Pap. Am. Chem. Soc.* 2004, 228, 563-INOR.

111. Schaak, R. E.; Sra, A. K., Controlling atomic order in intermetallic nanocrystals. *Abstr. Pap. Am. Chem. Soc.* 2004, 228, 763-INOR.

112. Schaak, R. E.; Sra, A. K., Synthesis of atomically ordered nanocrystals from bimetallic nanoparticle precursors. *Abstr. Pap. Am. Chem. Soc.* 2004, 227, 847-INOR.

113. Schaak, R. E.; Sra, A. K.; Leonard, B. M.; Cable, R. E.; Bauer, J. C.; Han, Y. F.; Means, J.; Teizer, W.; Vasquez, Y.; Funck, E. S., Metallurgy in a beaker: Nanoparticle toolkit for the rapid low-temperature solution synthesis of functional multimetallic solid-state materials. *J. Am. Chem. Soc.* 2005, 127, 3506-3515.

114. Seip, C. T.; Granroth, G. E.; Meisel, M. W.; Talham, D. R., Langmuir-Blodgett films of known layered solids: Preparation and structural properties of octadecylphosphonate bilayers with divalent metals and characterization of a magnetic Langmuir-Blodgett film. *J. Am. Chem. Soc.* 1997, 119, 7084-7094.

115. Shim, M.; Guyot-Sionnest, P., Organic-Capped ZnO Nanocrystals: Synthesis and n-Type Character. *J. Am. Chem. Soc.* 2001, 123, 11651-11654.

116. Shiman, R.; Draper, D. E., Stabilization of RNA tertiary structure by monovalent cations. *J. Mol. Biol.* 2000, 302, 79-91.

117. Shimazaki, Y.; Kobayashi, Y.; Yamada, S.; Miwa, T.; Konno, M., Preparation and characterization of aqueous colloids of Pt-Ru nanoparticles. *J. Colloid Interface Sci.* 2005, 292, 122-126.

118. Snyder, R. G.; Strauss, H. L.; Elliger, C. A., C-H Stretching Modes and the Structure of Normal-Alkyl Chains. 1. Long, Disordered Chains. *J. Phys. Chem.* 1982, 86, 5145-5150.

119. Storhoff, J. J.; Elghanian, R.; Mucic, R. C.; Mirkin, C. A.; Letsinger, R. L., One-Pot Colorimetric Differentiation of Polynucleotides with Single Base Imperfections Using Gold Nanoparticle Probes. *J. Am. Chem. Soc.* 1998, 120, 1959-1964.

120. Sun, Y. G.; Xia, Y. N., Gold and silver nanoparticles: A class of chromophores with colors tunable in the range from 400 to 750 nm. *Analyst* 2003, 128, 686-691.

121. Tang, Y.; Cheng, W. L., Metallic Nanoparticles as Advanced Electrocatalysts. *Science of Advanced Materials* 2012, 4, 784-797.

122. Thomas, L. C.; Chittend.Ra, Characteristic Infrared Absorption Frequencies of Organophosphorus Compounds-VII. Phosphorus Ions. *Spectrochim. Acta, Part A* 1970, A 26, 781-&.

123. Thomas, L. C.; Chittenden, R. A., Characteristic Infrared Absorption Frequencies of Organophosphorus Compounds. 1. The Phosphoryl (P=O) Group. *Spectrochim. Acta* 1964, 20, 467-487.

124. Tian, N.; Zhou, Z. Y.; Sun, S. G.; Ding, Y.; Wang, Z. L., Synthesis of tetrahexahedral platinum nanocrystals with high-index facets and high electro-oxidation activity. *Science* 2007, 316, 732-735.

125. Tindall, K. R.; Kunkel, T. A., Fidelity of DNA synthesis by the Thermus aquaticus DNA polymerase. *Biochemistry* 1988, 27, 6008-6013.

126. Tuerk, C.; Gold, L., SYSTEMATIC EVOLUTION OF LIGANDS BY EXPONENTIAL ENRICHMENT - RNA LIGANDS TO BACTERIOPHAGE-T4 DNA-POLYMERASE. *Science* 1990, 249, 505-510.

127. Uchida, M.; Flenniken, M. L.; Allen, M.; Willits, D. A.; Crowley, B. E.; Brumfield, S.; Willis, A. F.; Jackiw, L.; Jutila, M.; Young, M. J.; Douglas, T., Targeting of Cancer Cells with Ferrimagnetic Ferritin Cage Nanoparticles. *J. Am. Chem. Soc.* 2006, 128, 16626-16633.

128. Valden, M.; Lai, X.; Goodman, D. W., Onset of catalytic activity of gold clusters on titania with the appearance of nonmetallic properties. *Science* 1998, 281, 1647-1650.

129. Vasquez, Y.; Henkes, A. E.; Bauer, J. C.; Schaak, R. E., Nanocrystal conversion chemistry: A unified and materials-general strategy for the template-based synthesis of nanocrystalline solids. *J. Solid State Chem.* 2008, 181, 1509-1523.

130. Wadia, C.; Alivisatos, A. P.; Kammen, D. M., Materials Availability Expands the Opportunity for Large-Scale Photovoltaics Deployment. *Environ. Sci. Technol.* 2009, 43, 2072-2077.

131. Wang, F.; Tang, R.; Buhro, W. E., The Trouble with TOPO; Identification of Adventitious Impurities Beneficial to the Growth of Cadmium Selenide Quantum Dots, Rods, and Wires. *Nano Lett.* 2008, 8, 3521-3524.

132. Wang, H. S.; Abruna, H. D., Electrocatalysis of Direct Alcohol Fuel Cells: Quantitative DEMS Studies. In *Fuel Cells and Hydrogen Storage*, Bocarsly, A.; Mingos, D. M. P., Eds. 2011; Vol. 141, pp 33-83.

133. Wang, W.; Banerjee, S.; Jia, S.; Steigerwald, M. L.; Herman, I. P., Ligand Control of Growth, Morphology, and Capping Structure of Colloidal CdSe Nanorods. *Chem. Mater.* 2007, 19, 2573-2580.

134. Wiley, B.; Sun, Y. G.; Xia, Y. N., Synthesis of silver wanostructures with controlled shapes and properties. *Acc. Chem. Res.* 2007, 40, 1067-1076.

135. Wilson, O. M.; Hu, X. Y.; Cahill, D. G.; Braun, P. V., Colloidal metal particles as probes of nanoscale thermal transport in fluids. *Physical Review B* 2002, 66.

136. Woodhouse, M.; Herman, G. S.; Parkinson, B. A., Combinatorial approach to identification of catalysts for the photoelectrolysis of water. *Chem. Mater.* 2005, 17, 4318-4324.

137. Woodhouse, M.; Parkinson, B. A., Combinatorial discovery and optimization of a complex oxide with water photoelectrolysis activity. *Chem. Mater.* 2008, 20, 2495-2502.

138. Woodhouse, M.; Parkinson, B. A., Combinatorial approaches for the identification and optimization of oxide semiconductors for efficient solar photoelectrolysis. *Chem. Soc. Rev.* 2009, 38, 197-210.

139. Wu, J. B.; Zhang, J. L.; Peng, Z. M.; Yang, S. C.; Wagner, F. T.; Yang, H., Truncated Octahedral Pt3Ni Oxygen Reduction Reaction Electrocatalysts. *J. Am. Chem. Soc.* 2010, 132, 4984-+.

140. Xu, D.; Bliznakov, S.; Liu, Z. P.; Fang, J. Y.; Dimitrov, N., Composition-Dependent Electrocatalytic Activity of Pt-Cu Nanocube Catalysts for Formic Acid Oxidation. *Angewandte Chemie-International Edition* 2010, 49, 1282-1285.

141. Xu, D.; Liu, Z. P.; Yang, H. Z.; Liu, Q. S.; Zhang, J.; Fang, J. Y.; Zou, S. Z.; Sun, K., Solution-Based Evolution and Enhanced Methanol Oxidation Activity of Monodisperse Platinum-Copper Nanocubes. *Angewandte Chemie-International Edition* 2009, 48, 4217-4221.

142. Yang, J.; Deivaraj, T. C.; Too, H. P.; Lee, J. Y., Acetate stabilization of metal nanoparticles and its role in the preparation of metal nanoparticles in ethylene glycol. *Langmuir* 2004, 20, 4241-4245.

143. Yasuda, H.; Mori, H., SPONTANEOUS ALLOYING OF ZINC ATOMS INTO GOLD CLUSTERS AND FORMATION OF COMPOUND CLUSTERS. *Phys. Rev. Lett.* 1992, 69, 3747-3750.

144. Yin, A. X.; Min, X. Q.; Zhang, Y. W.; Yan, C. H., Shape-Selective Synthesis and Facet-Dependent Enhanced Electrocatalytic Activity and Durability of Monodisperse Sub-10 nm Pt-Pd Tetrahedrons and Cubes. *J. Am. Chem. Soc.* 2011, 133, 3816-3819.

145. Yin, M.; Gu, Y.; Kuskovsky, I. L.; Andelman, T.; Zhu, Y.; Neumark, G. F.; O'Brien, S., Zinc Oxide Quantum Rods. *J. Am. Chem. Soc.* 2004, 126, 6206-6207.

146. Yin, Y.; Alivisatos, A. P., Colloidal nanocrystal synthesis and the organic-inorganic interface. *Nature* 2005, 437, 664-670.

147. Zhang, H.; Huang, F.; Gilbert, B.; Banfield, J. F., Molecular Dynamics Simulations, Thermodynamic Analysis, and Experimental Study of Phase Stability of Zinc Sulfide Nanoparticles. *The Journal of Physical Chemistry B* 2003, 107, 13051-13060.

148. Zhang, J.; Yang, H. Z.; Fang, J. Y.; Zou, S. Z., Synthesis and Oxygen Reduction Activity of Shape-Controlled Pt3Ni Nanopolyhedra. *Nano Lett.* 2010, 10, 638-644.

149. Zhang, Z.; Lu, M.; Xu, H.; Chin, W.-S., Shape-Controlled Synthesis of Zinc Oxide: A Simple Method for the Preparation of Metal Oxide Nanocrystals in Non-aqueous Medium. *Chem.--Eur. J.* 2007, 13, 632-638.

150. Zhong, C. J.; Luo, J.; Fang, B.; Wanjala, B. N.; Njoki, P. N.; Loukrakpam, R.; Yin, J., Nanostructured catalysts in fuel cells. *Nanotechnology* 2010, 21.

151. Zhou, K. B.; Li, Y. D., Catalysis Based on Nanocrystals with Well-Defined Facets. *Angewandte Chemie-International Edition* 2012, 51, 602-613.

152. Zhou, Y. K.; Neyerlin, K.; Olson, T. S.; Pylypenko, S.; Bult, J.; Dinh, H. N.; Gennett, T.; Shao, Z. P.; O'Hayre, R., Enhancement of Pt and Pt-alloy fuel cell catalyst activity and durability via nitrogen-modified carbon supports. *Energy & Environmental Science* 2010, 3, 1437-1446.

153. Zuker, M., Mfold web server for nucleic acid folding and hybridization prediction. *Nucleic Acids Res.* 2003, 31, 3406-3415.